Self-organized Tethered Structures in Polymers under Confinement

by

Xi Chen

A dissertation submitted in partial fulfillment
of the requirements for the degree of
Doctor of Philosophy
(Macromolecular Science and Engineering)
in The University of Michigan
2011

Doctoral Committee:

Professor Peter F. Green, Chair
Professor Theodore G. Goodson III
Associate Professor Jinsang Kim
Associate Professor Max Shtein

To my parents,

Guangzhi Gao and Fuli Chen

Acknowledgement

It's three thirty in the morning, and I'm looking at my fruitful six years of work. I can't help but feel lucky, that I am surrounded by such great mentors, colleagues and friends. No words can possibly express my gratitude to all of you.

First and foremost, I'd like to acknowledge my advisor, Prof. Peter F. Green. I tell everyone that he is the best advisor a graduate student can hope for, and that is true. His dedication to research deeply influenced me. I am in love with research just as much as he does now. I gained a great deal of confidence over the years because of his encouragement and support. Now I'm looking at my publications and thinking about the great many things I learned from him, I just want to say, thank you, Peter, for being my advisor.

Next I would like to thank my dissertation committee, Prof. Theodore Goodson III, Prof. Jinsang Kim, Prof. Max Shtein, and former committee member Prof. David Martin. They gave me a lot of advice and helped me to complete my thesis. Their help and support are sincerely appreciated. Before my data meeting, Prof. Goodson took me to a coffee shop to go over my slides with me. Prof. Kim never hesitated to give me materials when I needed them. He even recommended me to a renounced company for a research position. Prof. Shtein's challenging questions taught me how to be assertive.

I would also like to thank EMAL staff, Dr. Kai Sun, for his help to me on the TEM. I learned a great deal about TEM's operations and sample preparations from him.

I must thank my program, Macromolecular Science and Engineering, and the persons who make this program so spectacular, Nonna Hamilton, and Prof. Richard Laine. I feel at home here.

I would like to thank all my colleagues from Green Group, especially Dr. Luciana Meli who trained me to use the TEM. She never hesitated to help me with my difficulties. I'd like to thank Hengxi Yang. It's been a great pleasure working on the micelle projects with him. I also want to thank other group members, all of whom are my great collaborators, Dr. Emmanouil Glynos, Dr. Ernest McIntyre, Dr. Hyunjoon Oh, Jenny Kim, Jojo Amonoo, Bingyuan Huang, Bradley Frieberg, Peter Chung and Junnan Zhao. We are such an awesome group.

Many thanks to my collaborators, Jonas Locke, Prof. Anne McNeil, Kui Zhang and Jake Jokisaari for their support in the organic solar cell related projects.

I'd like to express my gratitude to my parents. This dissertation is dedicated to them. Although we are far away from each other, I know that they always have my back.

I also made friends with some great people in Ann Arbor. Thank you to all of them. They made my life in Ann Arbor much more colorful.

In the end, I'd like to acknowledge the funding sources that have supported me through my PhD work. I'd like to acknowledge the National Science Foundation, Division of Materials Research, Polymers Program for micelle formation projects, the Department of Energy, Office of Basic Energy Science, for nanoparticle-polymer-composite related projects, and the Center for Solar and Thermal Energy Conversion, an

Energy Frontier Research Center funded by the Department of Energy Office of Basic Energy Sciences for studies related to organic solar cells.

Table of Contents

List of Figures

List of Tables

Abstract

Polymer nanocomposites (PNCs), polymer hosts into which nano-scale fillers are incorporated, are a technologically important class of materials, with diverse applications: optoelectronic devices, coatings, lithographic tools, membranes and stimulus-responsive systems. Understanding, controlling and optimizing the properties of these materials continue to pose significant technical challenges. Control of the spatial distribution of the nanofillers within the polymer hosts remains one of the challenges due to complex entropic and enthalpic interactions.

Many of the applications of PNCs require them to perform in geometrically confined environments, such as thin films, where interactions between the constituents of the PNC and interfaces are important. The role of the interfaces is sometimes unclear; in some cases the presence of the interfaces can change the morphology and hence the properties/performance of the PNC.

Our research is aimed at gaining control of the structure and nano-scale morphology of thin film PNCs and understanding the structure-property relationships. Our goal is to design PNCs with tailored morphologies and desired properties for specific applications. A series of topics are examined.

First we introduce the design rules of thin film PNCs by investigating the equilibrium structure of polymer-tethered metal nanoparticles/polymer composites. Specifically, the morphologies of thin film blends of polystyrene (PS)-brush coated Au nanoparticles with tetramethyl bisphenol-A polycarbonate (TMPC) were investigated. The role of entropic and enthalpic interactions towards determining the structure of thin film polymer/polymer-tethered nanoparticle systems is examined.

Following that we apply the rules to the design of a series of PNCs with tailored fluorescence properties using chain-grafted Au nanoparticle/poly[2-methoxy-5-(2-ethylhexyloxy)-1,4-phenylenevinylene] (MEH-PPV) mixtures. We achieved control of the Au nanoparticle distribution within MEH-PPV by manipulating the enthalpic and entropic interactions between the grafted brush layers and the host chains. Further, the fluorescence of these Au/MEH-PPV nanocomposite thin films may be "tailored" by as much as an order of magnitude, through changes in the nanoparticle distribution, brush length and nanoparticle size.

Lastly, we compare different tethered structures (nanoparticles vs diblock copolymer) in thin film PNCs. The roles of entropy and enthalpy in the micelle formation and surface adsorption of diblock copolymers in thin film homopolymer melts are examined.

Chapter 1

Introduction

1.1 Objectives

We are interested in the structure and properties of a class of the technologically important **polymer nanocomposites (PNCs)**. In PNCs the polymer serves as a host for fillers of nanoscale dimensions. The nanofillers are typically nanoparticles of various shapes, nanofibers and sheets, carbon nanotubes and buckyballs, as well as copolymers. Polymer nanocomposites are used for diverse applications[1-6] in optoelectronic devices, coatings, lithographic tools, membranes and stimulus-responsive systems. One of the most significant challenges in this field is controlling the dispersion of the nanoparticles within the polymer host. One promising strategy is to tether polymer chains to the surfaces of the nanoparticles in order to render them miscible with the polymer host. The research described in this thesis is focused entirely on "tethered" polymer nanoparticle systems.

While the research into polymer nanocomposites has been ongoing for three decades, with important challenges remain. Filler aggregation is a primary practical problem because it adversely affects the efficiency and functionality of the nanofillers. To prevent the nanofillers from aggregating, and furthermore, to achieve precise control

of the nano-scale morphology of the PNCs is the key to obtain maximum property enhancement of the composites.

Many of the applications of PNCs require them to perform in geometrically confined environments, such as thin films, where interactions between the constituents of the PNC and interfaces are important. The role of the interfaces is sometimes unclear; in some cases the presence of the interfaces can change the morphology and, hence, the properties/performance of the PNCs. Therefore, understanding the effects of the interfaces on the structure and properties geometrically confined PNCs is another important issue I will focus on in this work.

Through the studies done in this work, we intend to gain understanding of the interactions between the components in the PNCs as well as with the interfaces, and explore ways to control the nanostructure of the PNCs. Finally, we want to apply the design rules to solve practical problems.

To this end, **my research is aimed at gaining control of the structure and nano-scale morphology of thin film PNCs and understanding the structure-property relationships. My goal is to design PNCs with tailored morphologies and desired properties for their specific applications**. The topics covered in this work is laid out in the following order: first we introduce the design rules of thin film PNCs by investigating the structure of polymer-tethered metal nanoparticles/polymer composites; then we apply this rule to the design of a series of PNCs with tailored fluorescence properties using fluorescent polymers. Following that we compare different tethered structures (nanoparticles vs diblock copolymer) in thin film PNCs. The roles of entropy and enthalpy in the micelle formation and surface adsorption of diblock copolymers in thin

film homopolymer melts are examined. Below is a summary of the topics we examined in this work:

1. role of entropic and enthalpic interactions towards determining the structure of thin film polymer/polymer-tethered nanoparticle systems (chapter 2);
2. control of morphology and the optical properties of polymer nanocomposites (chapter 3);
3. micelle formation and surface adsorption of diblock copolymer in thin film homopolymer melts: role of entropic interactions (chapter 4);
4. micelle formation of diblock copolymer in thin film homopolymer melts: role of enthalpic interactions (chapter 5);

For the remainder of this chapter, we will provide a brief background that the aforementioned topics are based on.

1.2 Distribution of polymer chain-tethered nanoparticles in thin film homopolymer melts

We are interested in exploring factors that determine the equilibrium distribution of nanoparticles within a specific, geometrically confined matrix, and how to precisely control the distribution of the nanoparticles. The equilibrium morphology of a PNC is the outcome of a complicated picture with various enthalpic and entropic interactions involved, for example, particle/polymer, particle/particle, particle/interface and polymer/interface interactions, at the nano-scale. In this subsection we lay out some

theoretical background of how these interactions determine the equilibrium structure of a PNC.

1.2.1 Hard spherical nanoparticles/bulk homopolymer mixtures

We begin by discussing the interactions in a PNC, in the bulk form, where the nanofillers are hard spherical nanoparticles. This part of the background is important because in some cases the tethered structures can be viewed as hard spheres, which we will see in chapter 2 and 4. We begin with the simplest case, where there are no enthalpic interactions between the hard spherical nanoparticles and the host polymer chains, i.e. the athermal case. In this case the structure of the PNC is dominated by the entropic interactions between the nanoparticles and the host.

In the athermal case, host chains in contact with a nanoparticle surface suffer conformational entropy loss, which scales as $\sim R_{NP}^2/Pa^2$,[7] where R_{NP} is the radius of the nanoparticle, P is the degree of polymerization of the host chains and a is the monomer size of the host. This results in a depletion zone within close proximity of the nanoparticle surface, which promotes particle aggregation.

In order to accommodate the imbedded nanoparticles, host chains have to stretch, and the stretching energy $F_{stretching} \sim [R_{NP}/R_g(P)]^2$, where $R_g(P)$ is the radius gyration of the host chains. This means it costs less elastic energy for longer host chains to accommodate smaller particles.

Finally, the entropy of mixing favors dispersion of the nanoparticles, and this contribution is $F_{mix} \sim (\varphi/R_{NP}^3)\ln\varphi$, where φ is the volume fraction of the nanoparticles. The distribution of the nanoparticles is determined by the relative contributions of these

energies. The foregoing discussion suggests that it is energetically easier to disperse smaller hard spherical nanoparticles, within longer polymer hosts.

In reality, bare inorganic nanoparticles often exhibit intense van der Waals force, an enthalpic interaction, which makes them attract to each other strongly. The van der Waals potential can be expressed as $V(x_d) = -A_H R_{NP}/6x_d$, where A_H is the Hamaker constant and x_d is the distance of separation between the center of the nanoparticles. An effective way to shield the unfavorable van der Waals force, and to promote particle dispersion, is to chemically or physically graft a layer of polymer chains, refered to as the brush layer, onto the nanoparticle surface. The distribution of these "tethered" nanoparticles in a polymer host is largely determined by the interactions between the brush layer and the host chains.

1.2.2 polymer chain-tethered nanoparticles/bulk homopolymer mixtures

If the grafted chains are chemically identical to the host chains, i.e., the Flory-Huggins interaction parameter $\chi = 0$, the athermal case, the nanomorphology of the PNC, in its bulk form, is determined by the following factors: the degrees of polymerization of the grafted chains and the host chains, N and P, the grafting density, σ, and the radius of the nanoparticle cores, R_{core}[8-11]. In circumstances where the grafting density is high, grafted chains are relatively short, the host chains are excluded from the vicinity of the surface of the nanoparticle cores and reside only in the outer region of the brush layer, resulting in a "dry-brush" condition. In this case there is only finite penetration of the host chains into the brush layer, $\lambda = Na/\sigma P$, where λ is the penetration depth[10]. The depleting of host chains near the particle surface leads to particle aggregation and phase separation between the particles and host chains. Contrary to that, in circumstances where

the grafting densities are lower, the gain of translational entropy of the host chains by penetrating into the brush dominates, grafted chains would stretch to accommodate host chains, leading to complete interpenetration between the brush layer and the host, particles are sterically stabilized, hence dispersion is achieved. Given moderate grafting densities, for planer brush or surfaces of low curvature, the dry-brush to wet-brush transition is $N = P^{11}$.

It is important to note that the size of the nanoparticle cores plays a significant role in the interactions between the brush layer and the host chains. The effects of the particle size may be understood as the effective grafting density, σ_{eff}, is lower on a curved surfaces than on a flat surface, $\sigma_{\text{eff}} = \sigma R_{\text{core}}^2/(R_{\text{core}}+l)^2$, where l is the brush thickness. Note that σ_{eff} decreases with R_{core}, leading to enhanced miscibility between the nanoparticles and the host. This implies that the smaller cores promote particle dispersion. On a curved surface, the effective penetration depth $\lambda_{\text{eff}} = (1+l/R_{\text{core}})^2\lambda$, provided that P is not too large. If P is very large, $\lambda_{\text{eff}} = (1+l/R_{\text{core}})^{2/3}\lambda$. We can see that penetration of the host chains is enhanced with decreasing particle size and increasing brush thickness.

To this end, we discussed the factors that determine the distribution of polymer chain-tethered nanoparticles in a bulk polymer host, where the grafted chains and the host chains are chemically identical. In practical situations, the grafted chains and the host chains are often different, and there are enthalpic interactions involved, i.e., the χ parameter is nonzero. In this case we need to consider both entropic and enthalpic contributions to the free energy of the system. In general, entropic contributions to the total energy of the system scale as $1/P$, and the enthalpic interactions scale as χP. If the grafted chains and the host are immiscible, and this unfavorable enthalpic interaction

dominates the other contributions to the free energy of the system, the nanoparticles will phase separate from the host. See chapter 3 for a specific example. For the case where the grafted chains and the host are compatible, $\chi < 0$, the enthalpic contributions can be summarized into a "diagram of states", as described by Borukhov and Leibler[9]. Briefly, if $|\chi| < N^{-1}$, the system is solely entropy-driven, the enthalpic contributions are negligible. The phase diagram consists of entropic dry-brush regimes and entropic wet-brush regimes. When $|\chi| > N^{-1}$, the enthalpic dry-brush and the enthalpic wet-brush regimes appear on the phase diagram. As $|\chi|$ increases, the enthalpy-driven regimes enlarge and the entropy-driven regimes shrink; a new enthalpic regime, the enthalpic mushroom regime appears when $|\chi| > N^{-/2}$. As $|\chi|$ further increases to $|\chi| > 1$, the entropic regimes completely disappear and the free energy of the system is solely enthalpy-driven. The transition from entropy dominated regimes to enthalpy dominated regimes occurs at $|\chi|P \approx 1$ in each of the above conditions.

1.2.3 polymer chain-tethered nanoparticle/homopolymer in a thin film confined geometry

The foregoing discussions summarized the interactions between the nanoparticles and the host chains in bulk PNCs. In general, the existence of an interacting interface, e.g., a thin film situation, decreases the miscibility between the nanoparticles and the host chains for a number a reasons. In an athermal thin film PNC system, particles tend to segregate to the interfaces, including the free surface and the substrate, because linear host chains gain conformational entropy by migrating away from the interfaces and replaced by nanoparticles. The surface free energy/area gain can be expressed as $F_{ch} =$

$\alpha k_B T(V_{NP}/V_s D_{NP}^2)$, where α is the number of degrees of freedom a polymer segment gains due to migrating away from the interface, V_{NP} is the volume of a nanoparticle, V_s is the volume of a statistical segment, and D_{NP} is the diamteter of the nanoparticle. When the nanoparticle surface is chain grafted, additional entropy gain occurs when they segregate to the interfaces as the tethered chains suffer less entropy loss than linear host chains.

Enthalpic interactions are also involved when there is an interface. Inorganic nanoparticle cores are strongly attracted to silicon or glass substrates. The interaction potential scales as $R_{core}/(d+l)$, where R_{core} is the radius of the nanoparticle core and d is the distance of outer surface of the brush layer to the substrate. The strength of the interaction increases with increasing particle core size. On the other hand, if the grafted chains possess a lower surface energy than the host chains, the nanoparticles will segregate to the free surface.

In this subsection we introduced the theories that describe the parameters that determine the equilibrium structure of thin film PNCs. In chapter 2, we will further explore the design rules by investigating the effects of N, P, nanoparticle curvature as well as enthalpic contributions and monomer asymmetries in the structure of polystyrene grafted nanoparticles in thin film PS and tetramethyl bisphenol-A polycarbonate (TMPC).

1.3 Surface plasmon resonance of metal nanoparticles and its effects on the fluorescence properties of nearby molecules

In this subsection we introduce a phenomenon unique to the nano-sized noble metal particles, namely surface plasmon resonance, and discuss its applications in altering the optical properties of functional polymers.

1.3.1 Surface plasmon resonance of noble metal nanoparticles

Surface plasmon resonance is not a new phenomenon to man. Ruby glass containing colloidal gold as a color pigment was produced in Ancient Roman times. As the size of noble metals decreases to below 100 nm range, the free electrons are confined to the nanoparticle surface, hence the nanoparticles possess very different properties from the bulk due to the quantum confinement effect. They can interact with electromagnetic field, such as light, through collective charge density oscillations confined to nanoparticles, referred to as surface plasmon resonance[12, 13], and drastically change the local optical field. Therefore noble metal nanoparticles can strongly absorb and scatter light, their colloidal suspensions exhibiting vivid colors. Surface plasmon resonance is highly sensitive to the size and shape of the nanoparticles. These unique size-dependent electronic properties render them excellent candidates for a large number of applications[14-17], from biosensing, cancer detection to optoelectronic devices. The research into surface plasmon resonance of noble metal nanoparticles has recently become intense, in the past decade, as mature synthetic methods to prepare nanoparticles were developed.

The size dependence of surface plasmon resonance has two origins. For small particles (< 25 nm for gold), as the size of the particles decreases, the atomic structure of the nanoparticles may change, and the effect of the particle surface, such as increased localization of the electrons and change of coordination numbers, becomes more significant, resulting a size-dependent dielectric function. This is referred to as the intrinsic size effect[18], because the intrinsic properties of the materials change with size. The total extinction coefficient of metal nanoparticles is given as the summation over all electric and magnetic multipole oscillations contributing to the absorption and scattering of the interacting electromagnetic field, first calculated by Mie in 1908. In the intrinsic regime, the dipole approximation, an approximation taking only the dipole term into account while ignoring the higher order terms, applies, and the extinction coefficient is expressed by

$$\kappa = \frac{18\pi NV\varepsilon_m^{3/2}}{\lambda} \frac{\varepsilon_2}{(\varepsilon_1 + 2\varepsilon_m)^2 + \varepsilon_2^2} \qquad (1)$$

where κ is the extinction coefficient, N and V are the number and volume of the nanoparticles, respectively, λ is the wavelength of the incident light, ε_m is the dielectric constant of the surrounding medium, assumed to be independent of λ, and ε_1, ε_2 represent the real and imaginary parts of the metal's dielectric function, which in this regime are size dependent. The resonance occurs roughly at $\varepsilon_1(\omega) = 2\varepsilon_m$ if ε_2 is weakly dependent on ω, ω being the angular frequency of the incident light.

For larger nanoparticle (> 25 nm for gold), their dielectric functions ε(ω) is the same as that of the bulk material and hence size independent. The size dependence of the optical spectra of large particles is an extrinsic size effect dominated only by the

dimension of the particle with respect to the wavelength of the light. This is referred to as the extrinsic size effect.

Surface plasmon resonance is also particle shape dependent. For gold and silver nanorods, the optical extinction peak splits into a longitudinal peak and a transverse peak, corresponding to plasmon resonance along and perpendicular to the long axis of the nanorods, and the resonance gets stronger as the aspect ratio increases. For example, Wiley et al. reported a two-fold increase in scattering intensity of silver nanobars as the aspect ratio increased from 2 to 4[19].

1.3.2 Effect of metal nanoparticles on the fluorescence properties of nearby molecules

Light absorption occurs when electrons of molecules are excited to an elevated energy state by incident photons. The excited electrons may relax to the ground state through radiative decay, i.e., through emitting a photon, referred to as fluorescence. The excited electrons may also relax through nonradiative decay pathways, in which case no photons are emitted. The quantum yield, η, of the molecules, defined as the total number of photons emitted/total number of photons absorbed, can also be expressed by the radiative and nonradiative decay rate: $\eta = R_{rad}/(R_{rad}+R_{nonrad})$, where R_{rad} and R_{nonrad} are radiative and nonradiative decay rates of the fluorescent molecules, respectively.

When the fluorescent molecules are placed in the vicinity of a metal nanoparticle, their fluorescence properties may be significantly altered, as nanoparticles can change the radiative and nonradiative decay rates of the molecules, as well as affecting nearby optical field due to the surface plasmon resonance[20-22]. For example, by adjusting the plasmon resonance frequency to matching the emission peak of the dye molecules and by

increasing the scattering ability of the silver nanoparticles by making them into the form of nanoshells, the fluorescence of the dye molecules nearby can be enhanced by a factor of 50[21]. On the other hand, hyper-quenching can be achieved through mixing cationic conjugated polymer with negatively charged gold nanoparticles in an aqueous environment[22]. By adjusting the ionic strength, conjugation length and particle dimensions, the quantum yield of the polymer with the presence of the nanoparticles is only 10^{-11} of that in the absence of the nanoparticles. The hyper efficient quenching occurs through rapid internal energy or electron transfer between the polymer and the nanoparticles.

The effects of metal nanoparticles on the fluorescent properties, i.e., quenching or enhancement, are size dependent. The extinction of light, caused by metal nanoparticles, is the sum of absorption and scattering: $C_{ext} = C_{sca} + C_{abs}$, where C_{ext} is the extinction cross section of the nanoparticles, the hypothetical cross-sectional area which every incident photon enters is extinct (scattered or absorbed), and C_{sca} and C_{abs} are the scattering and absorption cross section, respectively. The scattering and absorption of light by small metal nanoparticles, less than 1/20 of the wavelength of the incident light, follow Rayleigh theory, which assumes that electrons oscillate at the same frequency and phase as the incident light. In this situation, C_{sca} scales as $\sim r^6$, where r is the radius of the nanoparticle, while C_{abs} scales as $\sim r^3$. Therefore as the size of a nanoparticle decreases, C_{abs}/C_{sca} increases rapidly. When the particle absorbs more light than it scatters, $C_{abs}/C_{sca} > 1$, it behaves as a quencher. When the nanoparticles are larger than about 1/20 of wavelength of the indent light, the scattering and absorption follow Mie theory, where the dipole and higher terms of the oscillations are all taken into account. In this regime the

size dependence of scattering and absorption has the same trend as in the Rayleigh region: C_{abs}/C_{sca} increases with decreasing particle size. Jain et al.[23] calculated the total extinction spectra of gold nanoparticles of different sizes, and they found that for 20 nm diameter gold nanoparticle, the extinction is almost exclusively contributed by absorption. In general, small, gold nanoparticles are good quenchers; big, silver nanoparticles are good enhancers.

In this subsection we introduced the optical properties of noble metal nanoparticles, and covered the size dependence of surface plasmon resonance and its effects on nearby fluorescent molecules. In chapter 3 we will discuss the design a series of PNCs with gold nanoparticles and fluorescent polymers, with tailored structure and optical properties.

1.4 Micelle formation of diblock copolymers in thin film homopolymer or homopolymer blends

A-*b*-B diblock copolymers, consist of two contiguous blocks of monomers with distinct properties, exhibit rich interfacial behavior. When dissolved into a selective solvent, say, a homopolymer consist of H monomers, at a low concentration, they can self-assemble into micelles, with a core of B monomers and a corona with A monomers, which can be viewed as a special type of fillers. Micelles have important applications in sequestration of nanoparticles[24] and drug delivery systems[25, 26]. On the other hand, micelle formation may be detrimental to the functionality of the diblock copolymers in modifying interfaces. Therefore the study of micelle formation in a diblock

copolymer/homopolymer A-*b*-B/H system has significant scientific and technological values.

1.4.1 Micelle formation in an A-*b*-B/A system

We begin with a relatively simple case, where the matrix homopolymer is chemically identical to one of the blocks, and is incompatible with the other: i.e. H = A, $\chi_{H\text{-}A} = 0$, $\chi_{A\text{-}B} = \chi_{H\text{-}B} > 0$, where $\chi_{A\text{-}B}$ is the Flory-Huggins interaction parameter between A and B blocks, and $\chi_{H\text{-}A}$ and and $\chi_{H\text{-}B}$ are those between the homopolymer H and block A, and homopolymer H and block B, respectively. The system contains only two types of monomers, A species and B species. To minimize unfavorable interactions between A and B species, the diblock copolymer tend self-assemble into micelles, of various shapes, depending on the disparities of between the degrees of polymerization of the A and B blocks, N_A and N_B, respectively, the degree of polymerization of the host homopolymer, P, $\chi_{A\text{-}B}$, and concentration. For example, symmetric polystyrene-*b*-poly(2-vinylpyridine) (PS-*b*-P2VP) form spherical micelles in PS homopolymers of a large range of molecular weights at low concentration. In poly(styrene-butadiene) diblock copolymer (SB)/PS blends, all of the spherical, cylindrical, lamellar and vesicular micelles can form, through changing N_A, N_B, P, and the concentration of SB[27].

In an A-*b*-B/A system, not all of the copolymer chains will self-assemble into micelles. In fact, the system needs some amount of free copolymer chains to keep its translational entropy, and no micelles will form if the concentration of the diblock copolymer is below that threshold value, which is referred to as the critical micelle concentration (cmc). Critical micelle concentration in the blend of a symmetric diblock

copolymer and a short homopolymer readily intermixed with the micelle corona is proportional to $\exp(-\chi_{A\text{-}B}N_B)$[28, 29]. The structure of micelles formed in an A-*b*-B/A system is determined by a balance of the following factors: the interfacial tension between A and B species, which favors large micelles, to minimize contact total area between A and B species; note that by large we mean the total number of copolymer chains in a micelle is large; the translational entropy of the homopolymer chains and the corona when homopolymer chains penetrate into the corona, which favors small micelles; and the conformational entropy of the homopolymer and the copolymer.

Similar to the concept of the dry-brush and wet-brush in the chain-tethered nanoparticles/homopolymer system, when the host homopolymer chains are sufficiently short, $P < N_A$, they readily intermix with the corona, it is a wet-brush case, and small micelles are favored, to maximize the translational entropy of the intermixing host chains and the corona. If the homopolymer chains are long, $P >> N_A$, they are largely excluded from the corona, and large micelles will form to minimize the contact area between the micelles and the host chains; this is the dry-brush case. Micelles exhibit long-range attraction in the dry-brush regime; the energy of attraction is proportional to the diameter of the entire micelle[30]. Recall that there is depletion attraction between nanoparticles in the chain-tethered nanoparticles/homopolymer system in the dry-brush regime. The comparison between these two systems is further explained in chapter 4.

1.4.2 Micelle formation in an A-*b*-B/H system

In an A-*b*-B/H system where A and B species are incompatible, H and B are also incompatible, while H and A have favorable specific interactions, i.e., $\chi_{A\text{-}B} > 0$, $\chi_{H\text{-}B} > 0$

and $\chi_{H\text{-}A} < 0$, the phase behavior of the system is determined by $\chi_{A\text{-}B}$, $\chi_{H\text{-}B}$ and $\chi_{H\text{-}A}$, as well as N_A, N_B, P, and the copolymer concentration. In systems where both macrophase separation and microphase separation can occur, the relative strength of $\chi_{A\text{-}B}$, $\chi_{H\text{-}B}$ and $\chi_{H\text{-}A}$ has significant impact on the phase boundaries. The more negative $\chi_{H\text{-}A}$ is, the less macrophase separation is expected. In the microphase separation regime, enthalpic interactions may affect the domain spacings of the ordered microphases, as well as shifting the location of the order-disorder transition.

The A-*b*-B/H systems have been investigated by a number of groups in the past two decades. Tucker and Paul[31] studied the mixing between poly(2,6-dimethyl-1,4-phenylene oxide) (PPO) and styrene based copolymers. They constructed a simple scaling model to show the effects of favorable enthalpy of mixing between PS block and PPO homopolymer on the maximum solubility of the homopolymer in the microphase separated copolymer. The same system was re-examined two decades later by Brinke and coworkers[32] where they calculated the concentration profile of the homopolymer in the lamella-structured diblock copolymer. Akiyama and Jamieson[33] showed the effects of specific interactions between homopolymer poly(styrene-co-acrylonitrile) (SAN) and poly(methyl methacrylate) (PMMA), on the structure of micelles formed in blends of SAN and poly(styrene-*b*-methyl methacrylate) (PS-*b*-PMMA) by systematically changing the acrylonitrile content in SAN. SAN/PS-b-PMMA system was also studied by Lowenhaupt et al. where the phase behavior showed both micro and macrophase separation[34]. They used random phase approximation calculations (RPA) to predict phase boundaries and compared that to the experimental results. Hashimoto and coworkers[35] investigated the blends of poly(vinyl methyl ether) (PVME) and poly(styrene-*b*-isoprene)

(SI) by small angle X-ray scattering. PVME and PS are known to show LCST behavior; they are miscible at low temperatures and become incompatible at high temperatures. Similar systems were studied by Balsara and coworkers[36] using poly(ethylene-*b*-propylene) (PE-*b*-PP)/polyisobutylene (PIB) blends. Self-consistent theoretical simulations were used to calculate the cylindrical-to-lamellar transitions of several systems including poly(oxyethylene-oxypropylene-oxyethylene) copolymers/poly(acrylic acid) (PAA) and polystyrene-*b*-poly(ethylene oxide) (PS-*b*-PEO)/PAA blends[37, 38].

In chapter 5 we discuss the addition of a small amount of TMPC into the blend of PS-*b*-P2VP/PS to show how enthalpic interactions can effectively tune the micelle formation of the system.

1.4.3 An A-*b*-B/H system under confinement

In the case of a thin film A-*b*-B/H system supported by a substrate, in addition to self-assembling into micelles, the copolymer chains may segregate to one, or both interfaces, forming brush layers, in order to minimize the free energy of the entire system. Brush layers would be absent if the homopolymer H were preferentially attracted to the free surface and the substrate. In a thin film PS-*b*-PMMA/PS system supported by silicon substrates, the critical micelle concentration is found to be orders of magnitude larger than that of the bulk, owing to surface adsorption of PMMA block to the substrate. On the other hand, the already formed micelles may exhibit long-range attractions to the interfaces as well. Micelle-interface attractions are mainly entropy-driven.

In chapter 4 and 5, we systematically examine how the homopolymer molecular weight and composition can affect surface adsorption of the diblock copolymer to the substrate, as well as the micelle-interface interactions.

1.5 References

1. van Bavel, S. S.; Barenklau, M.; de With, G.; Hoppe, H.; Loos, J. *Advanced Functional Materials* **2010,** 20, (9), 1458-1463.
2. Halls, J. J. M.; Walsh, C. A.; Greenham, N. C.; Marseglia, E. A.; Friend, R. H.; Moratti, S. C.; Holmes, A. B. *Nature* **1995,** 376, (6540), 498-500.
3. Vaia, R. A.; Maguire, J. F. *Chemistry of Materials* **2007,** 19, (11), 2736-2751.
4. Schadler, L. S.; Kumar, S. K.; Benicewicz, B. C.; Lewis, S. L.; Harton, S. E. *Mrs Bulletin* **2007,** 32, (4), 335-340.
5. Zorn, M.; Bae, W. K.; Kwak, J.; Lee, H.; Lee, C.; Zentel, R.; Char, K. *Acs Nano* **2009,** 3, (5), 1063-1068.
6. Kang, H.; Detcheverry, F. A.; Mangham, A. N.; Stoykovich, M. P.; Daoulas, K. C.; Hamers, R. J.; Muller, M.; de Pablo, J. J.; Nealey, P. F. *Physical Review Letters* **2008,** 100, (14).
7. Ginzburg, V. V. *Macromolecules* **2005,** 38, (6), 2362-2367.
8. Ferreira, P. G.; Ajdari, A.; Leibler, L. *Macromolecules* **1998,** 31, (12), 3994-4003.
9. Borukhov, I.; Leibler, L. *Macromolecules* **2002,** 35, (13), 5171-5182.
10. Xu, J. J.; Qiu, F.; Zhang, H. D.; Yang, Y. L. *Journal of Polymer Science Part B-Polymer Physics* **2006,** 44, (19), 2811-2820.
11. Matsen, M. W.; Gardiner, J. M. *Journal of Chemical Physics* **2001,** 115, (6), 2794-2804.
12. Brown, K. R.; Walter, D. G.; Natan, M. J. *Chemistry of Materials* **2000,** 12, (2), 306-313.
13. Kreibig, U.; Vollmer, M., *Optical Properties of Metal Clusters*. Springer: 1995; Vol. 25.
14. Elghanian, R.; Storhoff, J. J.; Mucic, R. C.; Letsinger, R. L.; Mirkin, C. A. *Science* **1997,** 277, (5329), 1078-1081.
15. Linden, S.; Kuhl, J.; Giessen, H. *Physical Review Letters* **2001,** 86, (20), 4688-4691.
16. Kitson, S. C.; Barnes, W. L.; Sambles, J. R. *Physical Review Letters* **1996,** 77, (13), 2670-2673.
17. Haynes, C. L.; Van Duyne, R. P. *Journal of Physical Chemistry B* **2001,** 105, (24), 5599-5611.
18. Link, S.; El-Sayed, M. A. *Journal of Physical Chemistry B* **1999,** 103, (40), 8410-8426.
19. Wiley, B. J.; Chen, Y. C.; McLellan, J. M.; Xiong, Y. J.; Li, Z. Y.; Ginger, D.; Xia, Y. N. *Nano Letters* **2007,** 7, (4), 1032-1036.

20. Dulkeith, E.; Morteani, A. C.; Niedereichholz, T.; Klar, T. A.; Feldmann, J.; Levi, S. A.; van Veggel, F.; Reinhoudt, D. N.; Moller, M.; Gittins, D. I. *Physical Review Letters* **2002,** 89, (20).
21. Tam, F.; Goodrich, G. P.; Johnson, B. R.; Halas, N. J. *Nano Letters* **2007,** 7, (2), 496-501.
22. Fan, C. H.; Wang, S.; Hong, J. W.; Bazan, G. C.; Plaxco, K. W.; Heeger, A. J. *Proceedings of the National Academy of Sciences of the United States of America* **2003,** 100, (11), 6297-6301.
23. Jain, P. K.; Lee, K. S.; El-Sayed, I. H.; El-Sayed, M. A. *Journal of Physical Chemistry B* **2006,** 110, (14), 7238-7248.
24. Meli, L.; Li, Y.; Lim, K. T.; Johnston, K. P.; Green, P. F. *Macromolecules* **2007,** 40, (18), 6713-6720.
25. Zhan, Y.; Mattice, W. L. *Macromolecules* **1994,** 27, (3), 677-682.
26. Gohy, J. F., Block copolymer micelles. In *Block Copolymers Ii*, Springer-Verlag Berlin: Berlin, 2005; Vol. 190, pp 65-136.
27. Kinning, D. J.; Winey, K. I.; Thomas, E. L. *Macromolecules* **1988,** 21, (12), 3502-3506.
28. Leibler, L.; Orland, H.; Wheeler, J. C. *Journal of Chemical Physics* **1983,** 79, (7), 3550-3557.
29. Whitmore, M. D.; Noolandi, J. *Macromolecules* **1985,** 18, (4), 657-665.
30. Esselink, F. J.; Semenov, A. N.; Tenbrinke, G.; Hadziioannou, G.; Oostergetel, G. T. *Physical Review B* **1993,** 48, (18), 13451-13458.
31. Tucker, P. S.; Paul, D. R. *Macromolecules* **1988,** 21, (9), 2801-2807.
32. Klymko, T.; Subbotin, A.; ten Brinke, G. *Macromolecules* **2007,** 40, (8), 2863-2871.
33. Akiyama, M.; Jamieson, A. M. *Polymer* **1992,** 33, (17), 3582-3592.
34. Loewenhaupt, B.; Steurer, A.; Hellmann, G. P.; Gallot, Y. *Macromolecules* **1994,** 27, (4), 908-916.
35. Iizuka, N.; Bodycomb, J.; Hasegawa, H.; Hashimoto, T. *Macromolecules* **1998,** 31, (21), 7256-7266.
36. Lee, J. H.; Balsara, N. P.; Chakraborty, A. K.; Krishnamoorti, R.; Hammouda, B. *Macromolecules* **2002,** 35, (20), 7748-7757.
37. Tirumala, V. R.; Daga, V.; Bosse, A. W.; Romang, A.; Ilavsky, J.; Lin, E. K.; Watkins, J. J. *Macromolecules* **2008,** 41, (21), 7978-7985.
38. LefeÃÄvre, N.; Daoulas, K. C.; MuÃàller, M.; Gohy, J.-F. o.; Fustin, C.-A. *Macromolecules* **2010,** 43, (18), 7734-7743.

Chapter 2

Structure Of Thin Film Polymer/Nanoparticle Systems: Polystyrene (PS) Coated-Au Nanoparticle/ Tetramethyl Bisphenol-A Polycarbonate (TMPC) Mixtures

2.1 Introduction

Diverse applications rely on the properties and performance of material surfaces onto which molecules are grafted: stabilization of colloidal suspensions [39-41], "tailoring" the wettability of surfaces [42-44], and stimulus-responsive environments [45, 46]. Polymer chains are grafted onto the surface of nanoparticles, which are then incorporated within polymer hosts, to make functional nanocomposites with various optical, mechanical and biomedical properties, for different applications [3-6, 47, 48]. Grafting is one strategy used to enable control of the spatial distribution of nanoparticles within a polymer host, which typically poses challenges due to complex enthalpic and entropic interactions[8-10, 49-52]. Appropriate choices of the chemistry of the grafted molecules, in principle, enable control of the thermodynamic interactions between the grafted layers and the host chains and hence the morphology and properties of the nanocomposite.

In thin films, external interfaces may have an important influence on the overall phase miscibility of the system[49, 50]. Depending on the relative polymer/nanoparticle size and monomer/particle size, the particles may exhibit a tendency to segregate to interfaces,

displacing the linear chains; the linear chains gain conformational entropy, as a result[53]. In the specific case of grafted nanoparticles, the tethered NPs suffer a smaller loss of entropy at the interfaces than linear chains at the interfaces; this effect is diminished with increasing N. For chemically dissimilar melt and brush chains, the surface energies and the relative chain-substrate interactions may have the most dominant effect on interfacial segregation[54]. Additionally, there may exist van der Waals attractive force between the nanoparticle cores and the substrate[50]. These factors contribute to preferential segregation of the nanoparticles to interfaces, which influences the structure of the polymer nanocomposite (PNC).

Meli et al.[50] showed that small gold nanoparticles of core radius $R_{core}\approx 1$ nm ($R_{core}<<P^{1/2}a$; a is the monomer size), onto which short PS chains (N=10) were grafted, were relatively miscible in PS hosts of P=125, whereas larger nanoparticles with core radii R_{core}=2-3 nm, onto which chains of N=10 monomers were attached, were completely immiscible; the nanoparticles resided exclusively at the interfaces. The grafting densities were 2 chains/nm^2. However, when the degree of polymerization of the grafted chains was increased to N=480, the nanoparticles were entirely miscible, implicating the role of favorable brush/melt chain interactions. In the case of the former the host chains are incompatible with the grafted layer, which forms a so-called "dry brush." A thin layer of the host PS chains would dewet a surface onto which the N=10 PS chains were grafted. A "wet brush" is formed by the longer grafted chains, enabling interpenetration by the host chains. The thickness of the long-chain grafted brush layer was sufficient to screen the van der Waals interactions with the substrate; hence segregation to the substrate was minimized.

Kim and Green[49] subsequently showed that the structure of athermal PS-coated Au/PS host thin film is characterized by a morphological phase diagram. To this end, three important observations were made. (1) In the limit where P>>N, nanoparticles of radii R_{NP}=5 nm (R_{NP}<<<<R_g(P) segregated exclusively to both interfaces of the PS films; R_{NP} is defined as R_{core}+d, where d is the brush thickness of 2.5 nm. (2) For P/N<3, the system was miscible, the nanoparticles are dispersed throughout the host chains. (3) For very large values of N and P, with R_g(N)>>R_{core}, phase separation occured and was accompanied by interfacial instabilities. This behavior is reminescient of polymer/polymer phase separation in thin films. They argued that since R_g(N)>> R_{core} the grafted nanoparticles might be considered multi-arm star shaped molecules; star/linear mixtures are thermodynamically unstable compared to linear/linear mixtures, due to entropic effects. In this regard the behavior of the polymer/grafted nanoparticle system could be considered analogous to a linear chain/star molecule mixture. For the situation where R_g(N)<<R_g(P) and R_g(N)~ D_{core}, the nanoparticles behave like hard spheres.

In many practical situations, the grafted layers on the nanoparticles and the host chains are chemically dissimilar and little is understood about the structure and morphology of such systems. In this paper we examine the phase behavior of thin film PS-coated Au nanoparticles mixed with tetramethyl bisphenol-A polycarbonate (TMPC); TMPC is thermodynamically compatible with polystyrene[55]. The case of chemically dissimilar melt-chain/grafted-chain interactions is particularly of practical significance, compared to the athermal case. However the thermodynamic, or enthalpic, interactions offer a new level of complexity. The role of the relative enthalpic and entropic

interactions towards the morphology of the system is investigated. A phase diagram is constructed to show the areas of miscibility and phase separation between the polymer chains and the nanoparticles. The phase boundaries are sensitive to nanoparticle size as well as the size of the polymer host chains, and that of the grafted chains. We find that additional factors, such as asymmetries in the monomer size, and or stiffness, not considered in current theories, must be considered in order to understand the behavior of the PS/TMPC system. They evidently play a non-trivial role.

2.2 Experimental

2.2.1 Synthesis and characterization of the Au NPs

Thiol terminated polystyrene (PS) stabilized Au nanoparticles were synthesized using the Brust method[56]. Gold(III) chloride hydrate ($HAuCl_4$), tetraoctylammonium bromide (TOAB), sodium borohydride ($NaBH_4$), and toluene were purchased from Sigma-Aldrich. Thiol terminated polystyrene (PS) with a series of molecular weights were purchased from Polymer Source Inc. Ultrapure water (resistivity = 18.3 MΩ-cm, NANOpureII, Barnstead) was used throughout this work. Briefly, Au(III) ions were transferred from an aqueous solution of $HAuCl_4$ to toluene with the presence of TOAB. After discarding the aqueous phase, an aqueous solution containing $NaBH_4$ was slowly added. The reaction mixture was allowed to stir for 2 – 24 hours before the Au NPs were passivated with thiol terminated PS ligands. NPs with core diamters of 2 – 5 nm were obtained from this method by using various concentrations of $HAuCl_4$ solutions and stirring times before passivating with the PS ligands.

The NPs were subsequently precipitated into methanol and redissolved in toluene to remove excess ligands in the reaction mixture. This procedure was repeated at least 10 times. Subsequently, in order to obtain NPs with more homogeneous size distributions, they were precipitated gradually, small portions each time, into a mixture of toluene and methanol. The heaviest particles precipitated first; the lightest ones precipitated last. The final precipitates were dried in a vacuum oven at room temperature for 24 hours and dissolved in toluene for use.

The physical characteristics of the Au NPs were determined by a combination of scanning transmission electron microcopy (STEM) and thermogravimetric analysis (TGA), as listed in Table 2-1. A drop of the nanoparticle solution was cast onto a 300 mesh carbon supported copper grid and dried in air in order to prepare a STEM sample. The samples were examined under a JEOL 2010F TEM, with an accelerating voltage of 200 kV, equipped with a high-angle annular dark-field (HAADF) detector. More than 300 NPs were analyzed to obtain the average diameter of the Au NPs. The length of the PS brush was estimated from the average edge-to-edge distance between the NPs by using at least 100 pairs of particles. A TA 2960 TGA, heating rate rate 10 °C/min, was used to determine the weight ratio between the Au cores and the PS ligands. The grafting densities of the NPs were estimated from calculating the average number of ligands grafted on a particle and the average surface area of a particle.

2.2.2 Preparation and morphological characterization of polymer nanocomposite thin films

Tetramethyl bisphenol-A polycarbonate (TMPC) (M_w = 37 900, PDI = 2.75, Bayer) and polystyrene (M_w = 13 000, PDI ≤ 1.06, Polymer Source Inc.) were dissolved

in toluene separately and the solutions were shaken for overnight. The polymer solutions were subsequently mixed with various Au NP solutions to obtain 5 wt% Au/polymer solutions. The solutions were spincoated onto Si_3N_4 substrates (WaferNet, Inc.). The film thicknesses were controlled to be 100 ± 3 nm. The films were dried in vacuum at 65 °C for 24 hours before further solvent annealing.

Solvent annealing of the samples was done in-situ on a variable angle spectroscopic ellipsometer (J.A.Woollam Co., Inc.) equipped with a custom-made heating stage. Toluene vapor with controlled vapor pressure was introduced into the heating stage, as described by Cavicchi and Russell[57]. The heating stage was kept at a constant temperature of 25 °C. Samples were stabilized in the stage for an hour before the vapor flow started. Film thickness was determined by fitting the ellipsometric angles, Δ and Ψ, to a Cauchy model in the WVASE32 software. The swelling of the samples were controlled to be around 35% by adjusting the flow rate (10 – 50 mL/min) of the pure N_2 flow and the N_2 bubbling through a toluene containing flask. Maximum swelling was reached in 10 to 50 min for different samples. The Au/PS samples were annealed for 30 – 60 min and the Au/TMPC samples were annealed for 16 – 36 hours.

The surface topography of the films was examined with a scanning probe microscope (SPM, MFP-3D, Asylum Research) operated in AC mode before and after solvent annealing. The films were subsequently measured using dynamic secondary ion mass spectroscopy, SIMS, a Physical Electronics 6650 Quadrupole instrument), by Dr. Tom Mates, to obtain the depth profiles of the Au NPs. A deuterated PS film was floated on top of the each sample before the SIMS measurements, to mark the location of the free surface of the films. The in-plane structures of Au/PS and Au/TMPC nanocomposites

were investigated with STEM. Thin films of Au/PS and Au/TMPC were spincoated from corresponding solutions onto glass substrates, floated on ultrapure water and picked up onto silicon nitride window grids (SPI Supplies). The annealing process was the same as described for the SIMS samples.

Table 2-1 Characteristics of Au nanoparticles

Nanoparticle	M_n *(g/mol)*[a]	D_{core} *(nm)*[b]	σ *(chains/nm^2)*[c]
Au(1.9)-PS_{10}	1000	1.9 ± 0.5	3.2
Au(2.8)-PS_{10}	1000	2.8 ± 0.8	2.7
Au(3.5)-PS_{30}	3000	3.5 ± 0.9	2.5
Au(2.4)-PS_{50}	5000	2.4 ± 0.8	2.0
Au(3.0)-PS_{110}	11500	3.0 ± 1.1	1.2
Au(4.1)-PS_{10}	1000	4.1 ± 0.9	1.8
Au(5.0)-PS_{30}	3000	5.0 ± 1.7	1.9
Au(4.2)-PS_{60}	6500	4.2 ± 1.4	1.1
Au(3.9)-PS_{110}	12000	4.5 ± 1.6	1.5
Au(4.5)-PS_{280}	29000	4.5 ± 1.6	1.6

[a]M_n, number average molecular weight of thiol-terminated polystyrene; [b]D_{core}, the average diameter of Au cores measured from STEM images; [c]σ, grafting density of the ligands.

2.3 Results and Discussion

2.3.1 Effects of the grafted chain length N

We begin by discussing the effect of the degree of polymerization of the grafted chains, N, on the structure of the Au-PS/TMPC systems. For the convenience we use the following notation: Au(d)-PS_N denotes Au NPs with a core diameter $D_{core} = d$ nm and grafted chain with degree of polymerization N. The spatial distributions of Au NPs, with constant core diameter $D_{core} \approx 4.3$ nm, throughout TMPC hosts, each of fixed degree of polymerization, P=120, are described in Fig.1. The information in Fig.1a-1c reveals that Au(4.1)-PS_{10} nanoparticles reside exclusively at the interfaces in TMPC thin films. The nanoparticles form close-packed aggregates at the free surface of the film (Fig. 2.1a and 2.1b) and the depth profile of Au (Fig. 2.1c) indicates that the majority of the Au NPs reside at the free surface. The NPs become dispersed with increasing N; when N=280, the Au(4.5)-PS_{280} nanoparticles are completely dispersed throughout the TMPC host, both laterally and normal to the substrate (Figs. 2.1d-2.1f). The morphologies investigated throughout this work are representative of equilibrium morphologies. The Au depth profiles of the Au-PS/TMPC samples were measured at different time intervals; samples typically reached equilibrium between 16 to 36 hours of annealing. The Au depth profile of an as-cast Au(4.1)-PS_{10} /TMPC sample is shown in the inset of Fig. 2.1c. The profile in Fig. 2.1c is that of the sample after 36 hours of annealing.

The basic principles behind polymer/brush melt interactions are now discussed. Conditions under which the free chains may completely interpenetrate the grafted chains, the so-called "wet brush" condition, or become largely excluded from the brush layer, the "dry brush" are specified entirely in terms of the parameters, N, P and σ[8]. For planar

surfaces, or surfaces of low curvature, the transition from wet-brush to dry-brush conditions occurs when $\sigma N^{1/2} > (N/P)^{-1/2}$, provided P/N < 1, and is $\sigma N^{1/2} = 1$ if P/N >1[8]. The curvature of the surface is important when $1/R >> 1/R_g(N)$; $R_g(N)$ is the radius of gyration of the grafted chains[10]. Under these conditions, the interactions are weaker than the interactions between two flat surfaces, because the effective grafting density is lower on a curved surface of the same grafting density. Matsen *et al.* have shown that for the situation in which the melt and brush chains are identical, the interfacial tension between the melt and brush layers is always positive, $\gamma_{brush/host} > 0$[11]. The finite interfacial tension leads to a long-range attraction between nanoparticles and this attraction decreases with increasing N/P; when N/P $\geq$ 1, $\gamma_{brush/host}$ becomes negligible. The nanoparticles are attracted to the interfaces, for reasons discussed earlier.

We are now in a position to understand the observations in Fig.2.1: Au(4.1)-PS_{10} nanoparticle phase separated from the TMPC host and with increasing N, Au(4.5)-PS_{280} nanoparticle dispersed in TMPC. The dispersion of nanoparticles, onto which chains are grafted (Fig.2.1d-f), occurs largely due to the enhancement of the interpenetration between the host chains and the brush layer, as N increases (at constant P, D_{core} and σ). The loss of conformational entropy of the brush chains, due to interpenetration, is offset by the gain in translational entropy of the host chains. The nanoparticles are attracted to the substrate due to van der Waals interactions; these interactions become increasing screened with increasing N. They are attracted to the free surface because PS has a lower surface energy than TMPC. The phase separation (Fig. 2.1a-2.1c) is believed to be a first order phase transition, engendered by the lower surface energy of the PS chains and the gain in entropy of the host chains[53].

2.3.2 Relative role of enthalpic and entropic effects

The foregoing discussion illustrates the effect of increasing N on the miscibility in polymer nanocomposite thin films; we now consider the role of the specific enthalpic interactions between the host and brush chains. The specific situation in which the degrees of polymerization of the PS and TMPC host chains are identical, $P_{PS}=P_{TMPC}=P=120$, is examined. As shown in Fig. 2.2a for the 5 wt% Au(4.3)-PS_N/TMPC systems, miscibility increases with increasing N. A phase transition, from complete phase separation to miscibility, occurs within the range of values of N: $110< N < 280$. For comparison, we also show that miscibility in the 5 wt% Au(4.3)-PS_N/PS system increases with increasing N (Fig. 2.2b). Surprisingly, the transition between surface enrichment and complete dispersion occurs for smaller N in the PS hosts: $60 < N <110$. This result is unexpected because $\chi<0$; presumably this favorable enthalpic interaction would lead to enhanced miscibility of the nanoparticles in the TMPC host.

To quantify the extent of the dispersion of nanoparticles in the PS and TMPC hosts, we computed the interfacial excess, in relation to the interior of the film, from the SIMS data using the following equation: $z=A_{FS}+A_S-(A_I/h_I)h$; the parameters are defined in Fig. 2.2c. z is plotted as a function of N, in Fig. 2d, for Au-PS_N in $TMPC_{120}$ and in PS_{120}. The relative increase in miscibility of the nanoparticles in the TMPC and the PS hosts, with increasing N, is more apparent in this figure. All the films examined in this study were approximately the same thickness, h = 100 ± 3 nm; the films also contained the same concentration of Au. This allows us to show the relative changes in the segregation of the nanoparticles. A value of z = 0 nm indicates that the particles are homogeneously distributed throughout the film, whereas z = 100 nm means that the

particles are completely segregated to the interfaces of the film. Therefore z is a relative measure of the extent of interfacial segregation in this system. Based on the actual data, and accounting for experimental error of the SIMS spectra, we define the criteria for dispersion and phase separation. It was appropriate to identify samples with values of $z \geq$ 80 nm as phase separated; Fig. 2.1a-2.1c illustrate such an example. The morphologies of films in this state are typical of those in Fig. 1a and 1b. When 20 nm $\leq z <$ 80 nm, the Au NPs are partially dispersed within the hosts. The Au NPs are spatially well dispersed throughout the hosts when $z <$ 20 nm; no ordering of the Au NPs is observed. Using these criteria, the transition between partial dispersion and complete dispersion in TMPC occurs at N ≈ 210 (N/P ≈ 1.75), whereas it occurs for N ≈ 80, (N/P ≈ 0.67) in the PS hosts. The location of the phase transition within the PS hosts is consistent with Matsen's calculations, which indicate that that flat brush/polymer interactions undergo a transition from non-wetting to wetting when N/P ≥ 1 and for a curved brush in our case, the transition should happen before N/P reaches 1.

That the miscibility transition occurred at larger values of N/P in the more compatible TMPC hosts deserves further discussion. To understand the role of the χ parameter, we note that Borukov and Liebler calculated the "diagram of states" for grafted polymer chains in contact with a thermodynamically compatible polymer melt, with $\chi_{brush\text{-}melt}<0$ [9]. They found that when $|\chi| > N^{-1}$, two new regimes appeared in the otherwise solely-entropy-driven diagram in the athermal case: (1) the enthalpic dry brush and (2) the enthalpic wet brush regimes. As $|\chi|$ increases, the enthalpic-driven regimes enlarge and gradually dominate the entropic-driven regimes; a new enthalpic regime, the enthalpic mushroom regime appears when $|\chi| > N^{-1/2}$. As $|\chi|$ further increases to $|\chi| >1$, the

entropic regimes completely disappear and the diagram of states is determined solely by the enthalpy. The transition from entropy dominated regimes to enthalpy dominated regimes occurs at $|\chi|P \approx 1$ in each of the above conditions. It follows from the foregoing that our system of varying N and fixed P = 120, the conditions for enthalpic dominated phases are $|\chi| > N^{-1}$, and $|\chi| \geq P^{-1} = 0.0083$.

The effects of increasing N on the thermodynamic interactions in the Au-PS/TMPC systems are two-fold. When $N^{-1} > |\chi|$, the enthalpic interactions are too weak to influence the brush structure, i.e.: entropic interactions dominate. Therefore, as N increases from 10 to 280 (N^{-1} decreases from 0.1 to 0.0036), for a constant χ, the enthalpy would naturally play an increasingly important role. Furthermore, the weight fraction of the brush grafted on these nanoparticles increase as the brush length N increase (note that the ratio of the Au cores/TMPC remains constant $w(Au)/[w(Au)+w(TMPC)] = 5\%$). Since the Flory-Huggins interaction parameter χ between TMPC and deuterated-PS is composition dependent[58], there would necessarily be a variation in χ with increasing N. In fact it follows that when w(PS) < 0.15, the blend behaves in a manner akin to an athermal system. However, when w(PS) > 0.25, the behavior of the blend should exhibit the influence of stronger thermodynamic interactions. In the 5% Au(4.1)-PS_N/TMPC mixtures, the weight fractions of the brush components are 0.011, 0.044, 0.099 and 0.21, for N = 10, 60, 110 and 280, respectively. Consequently the enthalpic interactions would not be sufficiently strong to affect the brush structure when N≤110 ($|\chi| << N^{-1}$, and $|\chi|P << 1$). Therefore the enthalpic dominated regime is not observed. However, when N = 280, χ is calculated to be -0.07 for T = 298.15K and w(PS)

= 0.25[58]. Since $N^{-1/2}<|\chi|<1$, $|\chi|^{1/2}<\sigma = 0.42<N^{-6/5}|\chi|^{-2/5}$, $|\chi| > 0.0083$, the brush structure falls in the enthalpic wet brush regime.

The failure of the predictions to capture the observation that the NPs are more readily dispersed within PS, than in TMPC, may be related to entropic effects associated with the asymmetries in monomer dimensions and stiffness. The theories assume that the monomer sizes of the grafted chains and the melt chains are identical. However there is a difference of a factor of 3 between the size of the PS and TMPC monomers; the monomer size of TMPC is a_{TMPC}=1.83 nm[59], whereas it is, a_{PS}=0.55 nm, for PS [50] . With this in mind it is tempting to examine an effective grafted chain length, N_{eff}, where the melt/brush interactions change from partial dispersion to complete dispersion. This value of N where the transition occurs is N_{TMPC}~210 for the TMPC host and N_{PS}~80 for the PS host. It is interesting that N_{TMPC}~3N_{PS} and that a_{TMPC}~3a_{PS}. The results qualitatively suggest that with the use of the appropriate scaling parameters that account for disparities in monomer size, important insight into the phase behavior of systems in with the grafted chains and host chains are chemically dissimilar may be obtained.

2.3.3 Effects of the nanoparticle size

We now examine the "dry-brush" situation in which N=10 and P = 120 are kept constant, the weight fraction of Au still being 5%, while the nanoparticle core size changes. The STEM image in Fig.3c and the depth profile in Fig. 2.3g indicate that when D_{core} = 4.1 nm the particles phase separated from TMPC. However as nanoparticle curvature increases, the extent of miscibility of nanoparticles within the film increases. When D_{core} < 2.8 nm particles are completely dispersed (Fig. 2.3a, 2.3b and 2.3g). For the Au-PS_{10}/PS systems, when D_{core} = 4.1 nm the nanoparticles also phase separated PS. As

the nanoparticle core size decreases, the extent of miscibility increases. However, when D_{core} = 2.8 nm, aggregates of particles can still be observed from the in-plane image (Fig. 2.3e); when D_{core} further decrease to 1.9 nm, the nanoparticles partially dispersed in PS (Fig. 2.3h, 2.3i). The interfacial excess as a function of nanoparticle size in Fig. 2.3i shows that decrease in the core diameter doesn't have as a strong effect in PS host than in TMPC.

The effect of the nanoparticle size on the phase behavior is also important because of its contribution to the entropy. Ignoring, for a moment, the polymer chain/nanoparticle enthalpic interactions, the polymer/nanoparticle miscibility would be determined by the competition between the particle-particle interactions, entropy of mixing and the conformational entropy. The entropy of mixing favors dispersion of the nanoparticles within the host chains: $F_{mix} \sim (\phi/R_{NP}^3)\ln\phi$, where ϕ is the particle volume fraction and R_{NP} is the radius of the nanoparticles. Mixing is opposed by the elastic energy, which increases as $F_{stretching} \sim [R_{NP}/R_g(P)]^{2}$ [7], with increasing nanoparticle size; $R_g(P)$ is the radius of gyration of the host chains. The particle-particle interactions can become attractive, due to the van der Waals forces, also opposing dispersion. Additionally, the host chains tend to migrate away from between particles in proximity in order to gain entropy, further contributing to aggregation of the nanoparticles. The particle-particle attractions are long-ranged, but are repulsive at short-range. It is evident that the particles which behave like hard spheres (short chains grafted at high density) are more miscible in TMPC than in PS. The results are consistent with the notion that with the same degree of polymerization, TMPC has a larger radius of gyration R_g, which means that TMPC host chains suffer less entropic penalty to accommodate the nanoparticles.

2.3.4 Phase behavior of Au/TMPC mixtures

Finally, a phase diagram of the miscibility of nanoparticles of varying core diameters, plotted as a function of N, in TMPC, is shown in Fig. 2.4. We begin by noting that while the grafting density can influence the interactions, within the range of grafting densities considered (Table 1), the effect is negligible compared to the particle size and N. The nanoparticles are dispersed for large values of N/P because the interpenetration of the brush chains by the host chains is associated with favorable enthalpic interactions. Additionally, nanoparticles of high curvature are also dispersed. They become immiscible when their curvature decreases and there is an insufficient change in energy associated with host-chain/brush-chain interactions to accommodate dispersion.

2.4 Conclusions

The phase behavior of PS-coated nanoparticles and TMPC mixtures was investigated. We showed that despite the favorable the enthalpic interactions between PS and TMPC, that entropic effects due to the brush/host chain interactions, total nanoparticle diameter, D, and asymmetries in monomer sizes of the host chains and grafted chains, can play the dominant role toward determining the phase miscibility of thin film nanoparticle homopolymer mixtures. Current theoretical studies of brush/melt interactions do not directly address the role of asymmetry in monomer sizes and chain flexibility on miscibility. These results have important implications on the design of brush coated nanoparticle/homopolymer mixtures for different applications.

2.5 REFERENCES

1. P. Pincus, *Macromolecules*, 1991, **24**, 2912-2919.
2. B. P. Binks, R. Murakami, S. P. Armes and S. Fujii, *Angewandte Chemie International Edition*, 2005, **44**, 4795-4798.
3. B. P. Binks and R. Murakami, *Nat Mater*, 2006, **5**, 865-869.
4. S. W. Hu, X. Q. Ren, M. Bachman, C. E. Sims, G. P. Li and N. Allbritton, *Anal. Chem.*, 2002, **74**, 4117-4123.
5. O. Azzaroni, A. A. Brown and W. T. S. Huck, *Angewandte Chemie International Edition*, 2006, **45**, 1770-1774.
6. M. Motornov, R. Sheparovych, I. Tokarev, Y. Roiter and S. Minko, *Langmuir*, 2006, **23**, 13-19.
7. S. Santer, A. Kopyshev, J. Donges, H.-K. Yang and J. R¸he, *Advanced Materials*, 2006, **18**, 2359-2362.
8. R. Sheparovych, M. Motornov and S. Minko, *Advanced Materials*, 2009, **21**, 1840-1844.
9. R. A. Vaia and J. F. Maguire, *Chem. Mat.*, 2007, **19**, 2736-2751.
10. L. S. Schadler, S. K. Kumar, B. C. Benicewicz, S. L. Lewis and S. E. Harton, *MRS Bull.*, 2007, **32**, 335-340.
11. M. Zorn, W. K. Bae, J. Kwak, H. Lee, C. Lee, R. Zentel and K. Char, *ACS Nano*, 2009, **3**, 1063-1068.
12. H. Kang, F. A. Detcheverry, A. N. Mangham, M. P. Stoykovich, K. C. Daoulas, R. J. Hamers, M. Muller, J. J. de Pablo and P. F. Nealey, *Phys. Rev. Lett.*, 2008, **100**.
13. A. Bansal, H. Yang, C. Li, B. C. Benicewicz, S. K. Kumar and L. S. Schadler, *Journal of Polymer Science Part B: Polymer Physics*, 2006, **44**, 2944-2950.
14. S. Laurent, D. Forge, M. Port, A. Roch, C. Robic, L. Vander Elst and R. N. Muller, *Chem. Rev.*, 2008, **108**, 2064-2110.
15. I. Borukhov and L. Leibler, *Macromolecules*, 2002, **35**, 5171-5182.
16. P. G. Ferreira, A. Ajdari and L. Leibler, *Macromolecules*, 1998, **31**, 3994-4003.
17. J. Kim and P. F. Green, *Macromolecules*, **43**, 1524-1529.
18. L. Meli, A. Arceo and P. F. Green, *Soft Matter*, 2009, **5**, 533-537.
19. J. J. Xu, F. Qiu, H. D. Zhang and Y. L. Yang, *J. Polym. Sci. Pt. B-Polym. Phys.*, 2006, **44**, 2811-2820.
20. L. M. Hall, A. Jayaraman and K. S. Schweizer, *Current Opinion in Solid State and Materials Science*, 2010, **14**, 38-48.
21. P. Akcora, H. Liu, S. K. Kumar, J. Moll, Y. Li, B. C. Benicewicz, L. S. Schadler, D. Acehan, A. Z. Panagiotopoulos, V. Pryamitsyn, V. Ganesan, J. Ilavsky, P. Thiyagarajan, R. H. Colby and J. F. Douglas, *Nat Mater*, 2009, **8**, 354-359.
22. E. S. McGarrity, A. L. Frischknecht and M. E. Mackay, *J. Chem. Phys.*, 2008, **128**.
23. X. C. Chen and P. F. Green, *Langmuir*, 2009, **26**, 3659-3665.
24. E. Kim, E. J. Kramer and J. O. Osby, *Macromolecules*, 1995, **28**, 1979-1989.

25. M. Brust, M. Walker, D. Bethell, D. J. Schiffrin and R. Whyman, *J. Chem. Soc.-Chem. Commun.*, 1994, 801-802.
26. K. A. Cavicchi and T. P. Russell, *Macromolecules*, 2007, **40**, 1181-1186.
27. M. W. Matsen and J. M. Gardiner, *J. Chem. Phys.*, 2001, **115**, 2794-2804.
28. E. J. K. Eugene Kim, John O. Osby, David J. Walsh,, *Journal of Polymer Science Part B: Polymer Physics*, 1995, **33**, 467-478.
29. H. Yang and J. M. O'Reilly, *Mat. Res. Soc. Symp. Proc.*, 1987, **79**, 129.
30. V. V. Ginzburg, *Macromolecules*, 2005, **38**, 2362-2367.

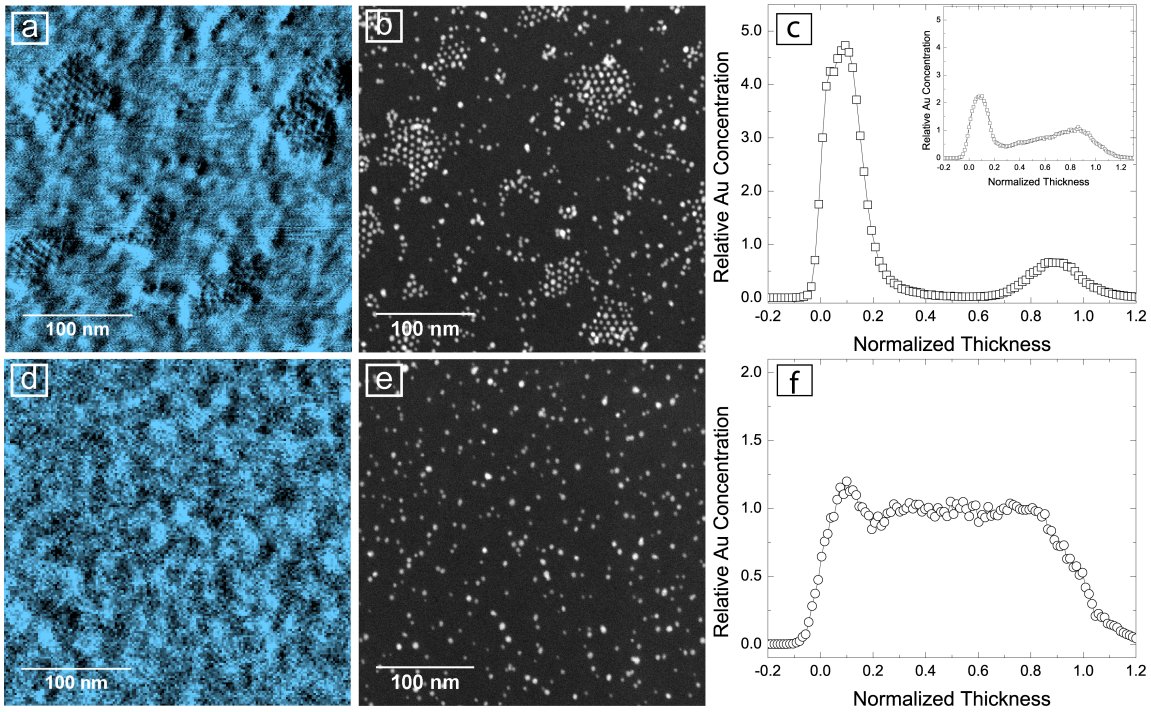

Figure 2.1 SPM images, STEM images and SIMS depth profiles of Au in the thin film Au/TMPC nanocomposites are shown here. (a, d) phase contrast images of the free surfaces of Au(4.1)-PS_{10}/TMPC films (part a) and of Au(4.5)-PS_{280}/TMPC (part d) were obtained using SPM; (b, e) lateral distributions of the Au NPs, obtained using STEM, are shown for Au(4.1)-PS_{10}/TMPC (part b) and Au(4.5)-PS_{280}/TMPC (part e). (c, f) The depth profiles of Au NPs, obtained using SIMS, for Au(4.1)-PS_{10}/TMPC (part c) and Au(4.5)-PS_{280}/TMPC (part f), are shown. In part c, the profile in the inset is that of the as-cast film. The main profile is that of the sample after it was annealed for 36 hours. The profile remained constant beyond this time.

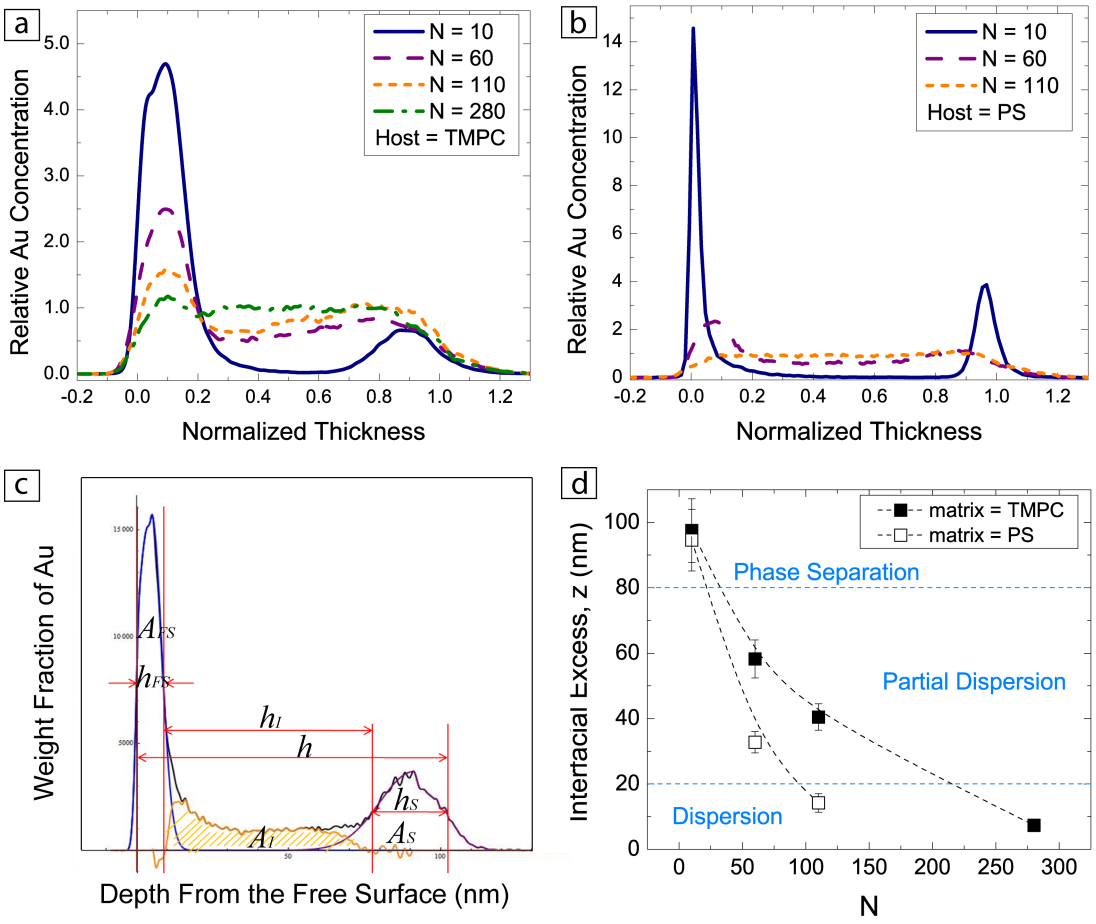

Figure 2.2 Shown here are the SIMS depth profiles of 5% Au NPs in: (a) TMPC and (b) PS (N = 10 (blue solid lines), N = 60 (purple dashed lines), N = 110 (orange short dashed lines) and N = 280 (green dash-dotted line). The core diameter of these particles is around 4.3 nm. (c) A schematic illustrating how the interfacial excess was determined for each sample. (d) The interfacial excess z is plotted as a function of the grafted chain length, N, in both TMPC and PS hosts.

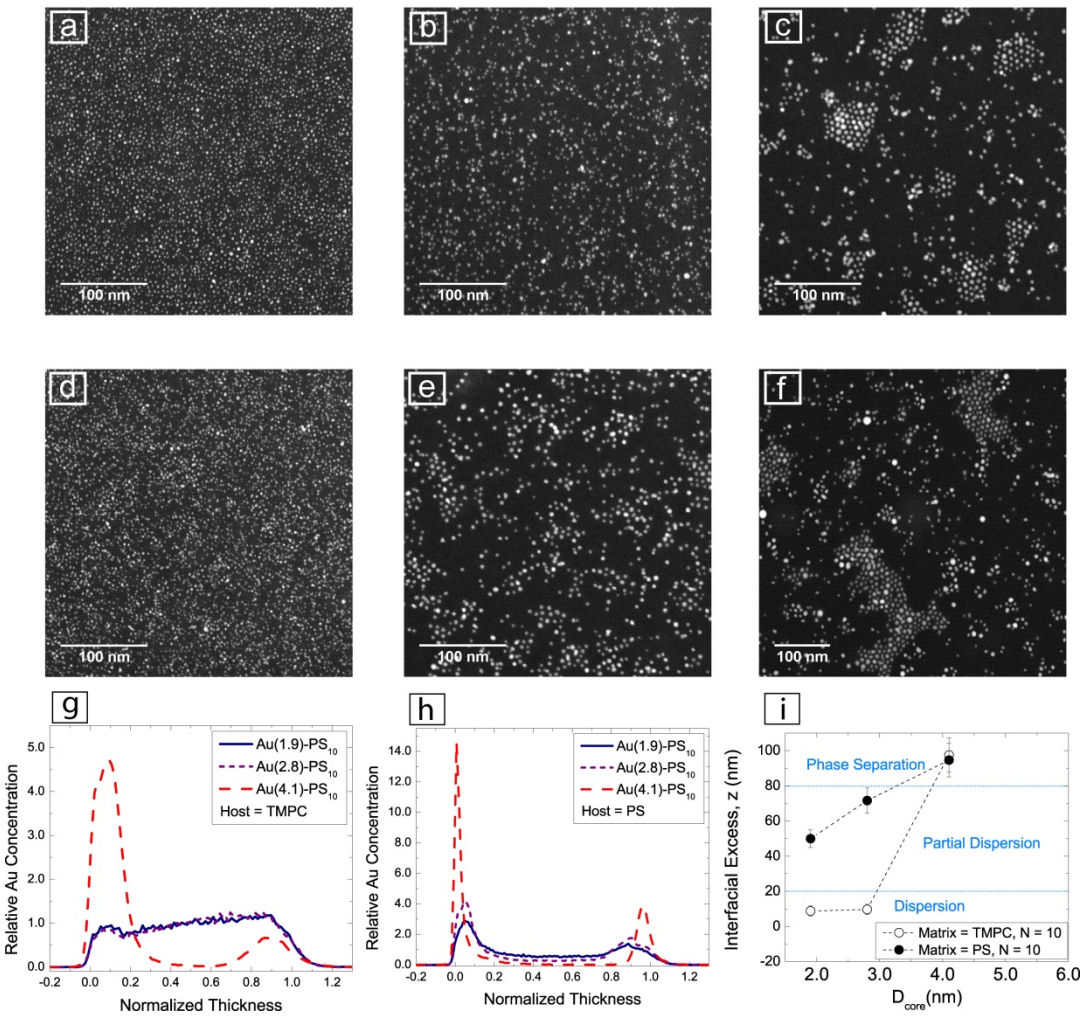

Figure 2.3 STEM images of 5 wt% of Au(1.9)-PS_{10} (part a), Au(2.8)-PS_{10} (part b) and Au(4.1)-PS_{10} (part c) NPs in TMPC, with the corresponding depth profiles in part g; as well as 5 wt% of Au(1.9)-PS_{10} (part d), Au(2.8)-PS_{10} (part e) and Au(4.1)-PS_{10} (part f) NPs in PS, with the corresponding depth profiles in part h. Interfacial excess, z, as a function of the nanoparticle core diameter, with fixed N = 10, in Au/TMPC (open circles) and Au/PS (solid circles) nanocomposites is shown in part i.

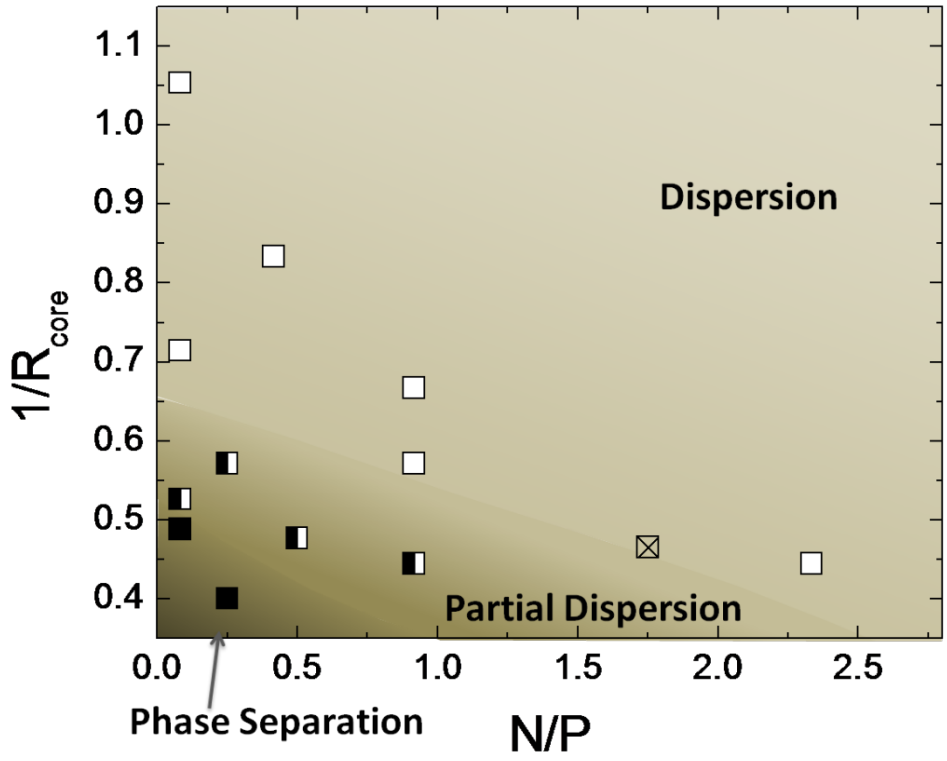

Figure 2.4 The phase diagram of Au/TMPC thin film nanocomposites. Solid, half filled, open points represent nanocomposites with the morphology of phase separation, partial dispersion and dispersion, respectively. The cross-filled point represents the boundary that was discussed in figure 2.

Chapter 3

Control of Morphology and Its Effect on the Optical Properties of Polymer Nanocomposites

3.1 Introduction

Nanoparticles (NPs) are incorporated within polymer hosts in order to create nanocomposites, or hybrid materials, with "tailored" properties[60-64]. The presence of a small volume fraction of nanoparticles often has a significant impact on the properties of the polymer[65]. Despite recent advances in understanding and controlling the structure of polymer nanocomposites (PNCs), particle aggregation remains a significant issue. One strategy for achieving particle dispersion involves grafting polymer chains onto the surfaces of the nanoparticles[66]. Control of the spatial distribution of the nanoparticles, and hence the morphology, enables control of the properties of the system. In this paper we show, through effective use of grafting, how the gold nanoparticle distribution in a fluorescent polymer host may be controlled. Secondly we show the connection between the spatial distribution of the nanoparticles and the fluorescence properties of the polymer nanocomposites.

In general, the brush/polymer host chain interactions are determined by the enthalpic interaction parameter between the host chains and the grafted chains, χ, the grafting density, σ, and the degrees of polymerization of the grafted chains and the host

chains, N and P, respectively[67]. For a systems where χ=0, the entropic interactions make the primary contribution to the free energy, and at reasonable grafting densities, and for P>>N, the host chains would be excluded from the grafted brush layer, creating the so-called "dry" brush condition. Alternatively, the so-called "wet" brush condition, where the host chains interpenetrate the grafted brush layers, occurs when N and P are comparable and the grafting density σ is not too high.

The nanoparticle distribution, and hence the morphology of such a system, for which χ=0, depends on the size of the nanoparticles, D, as well as on N, P and σ. Under dry brush conditions, nanoparticle aggregation would be favored in order to minimize the interfacial tension between the brush and host chains, whereas nanoparticle dispersion is favored under wet brush conditions. Of course the translational entropy favors particle dispersion and its influence increases with decreasing particle size. A competing effect that favors phase separation is that chains confined between the nanoparticles experience reduced conformational entropy, which becomes more severe with increasing P. For dissimilar melt and brush chains ($\chi \neq 0$), enthalpic interactions become important and this case is less understood [9]. We are particularly interested in a thin film system in which χ is non-zero. Thin films have the added attribute wherein the nanoparticles exhibit interfacial segregation under certain conditions, such as phase separation [24].

The foregoing summarized an effective strategy to control the nanoparticle distribution throughout a polymer host. In this study we report a simple way to create different spatial distributions of Au nanoparticles, within a fluorescent polymer, poly[2-methoxy-5-(2-ethylhexyloxy)-1,4-phenylenevinylene] (MEH-PPV) host. Further, we show how, at a fixed Au concentration of 5 wt.%, the fluorescence quenching of MEH-

PPV is changed from 4% to as much as 80%, through control of Au NP size, grafting layer thickness and NP spatial distribution.

This problem is of technological importance for the following reasons. Noble metal nanoparticles are endowed with strong light absorbing and scattering properties, exhibiting various colors in solutions, due to the collective oscillations of conduction electrons induced by incident light (surface plasmon resonance)[12, 13]. Such properties render them uniquely beneficial for applications in chemical and biomolecular detection[14], surface-enhanced spectroscopies[15], subwavelength optics[16] and lithographic tools[17]. When placed near fluorescent molecules, metal NPs influence the fluorescence emission of the fluorophores by changing the near field optical intensity and the radiative and non-radiative decay rates of the molecules[20-22], all of which are highly sensitive to the size and shape of the NPs as well as the structure of the nanocomposites.

3.2 Experimental

Gold NPs with diameters 2 nm and 5 nm were prepared by two-phase arrested precipitation, as described by Brust et al[56, 68]. The following chemicals, and their sources, were used to prepare the chain grafted gold nanoparticles. Gold(III) chloride hydrate ($HAuCl_4$), tetraoctylammonium bromide (TOAB), sodium borohydride ($NaBH_4$), dodecanethiol (DT) and toluene were purchased from Sigma-Aldrich. Thiol terminated polystyrene (PS) with nominal average molecular weight (M_n) of 1,000 g/mol and 50,000 g/mol were purchased from Polymer Source Inc. Chloroform was purchased from Fisher Scientific Inc. Ultrapure water (resistivity = 18.3 MΩ-cm, NANOpureII, Barnstead) was

used for solution preparation and cleaning. All glassware was treated with aqua regia prior to use.

The 5 nm Au nanoparticles were prepared as follows. A 15 mL aqueous solution of 0.07 M $HAuCl_4$ was mixed with 25 mL of 0.2 M TOAB in toluene. The aqueous phase was then separated and discarded after 30 min of stirring. A 30 mL aqueous solution of $NaBH_4$ was added slowly, dropwise, into the organic phase during vigorous stirring; the reaction mixture was stirred for 24 hours. Subsequently, the ligands were dissolved in toluene and added to the reaction mixture, which was then stirred for an hour. The molar ratios of Au to ligands were 1:1 (DT), 5:1 (PS, M_n = 1000 g/mol) and 19:1 (PS, M_n = 50000 g/mol), respectively.

With regard to the 2 nm Au NPs, 10 μM of $HAuCl_4$ in 3.0 mL of H_2O was transferred to 50 mL of toluene containing 1.8 mM TOAB. After discarding the aqueous phase, a 2.5 mL aqueous solution containing 1.0 mM of $NaBH_4$ was added, dropwise, into the organic phase. Only the thiol terminated PS of M_n=1000 g/mol was used for preparation of the 2 nm Au NPs. The thiols were added immediately after adding the reducing agent; the molar ratio of Au:ligands was 5:1. The aqueous phase was discarded after the NPs were passivated with the ligands.

The 2 nm and 5 nm grafted NPs were subsequently purified by precipitation into methanol and repeatedly dissolved in toluene, ten times. The final precipitate was dried in vacuum at room temperature for 24 hours and redissolved in chloroform.

The diameters of the Au cores and the thicknesses of the brush layers were determined from scanning transmission electron microscopy (STEM) images, obtained using JEOL 2010F TEM, operated at an accelerating voltage of 200kV with the high-

angle annular dark-field (HAADF) detector. A dilute toluene solution of the particles was cast onto a 300 mesh copper grid (Ted Pella). The thicknesses of the brush grafted on Au surfaces were estimated from the nearest neighbor distance between particles by analyzing approximately 100 pairs of particles in a nanoparticle monolayer film. The grafting densities of the particles were estimated from the surface area of the Au cores calculated from STEM images and weight fractions of the Au core and the ligands obtained from thermogravimetric analysis (TGA, TA 2960), heating rate 5 °C/min.

MEH-PPV (Aldrich, M_n = 70,000 – 100,000 g/mol) was dissolved in chloroform and the solution was shaken for a week; it was then filtered using PTFE filters of pore size 0.45 μm. Solutions containing Au/MEH-PPV nanocomposites were prepared by mixing the solutions of Au nanoparticles with MEH-PPV solutions at different weight ratios. Thin films were spincoated onto glass substrates. The substrates were sonicated in diluted alkaline concentrate (Hellma GmbH & Co.), ultrapure water (resistivity = 18.3 MΩ-cm, NANOpureII, Barnstead) and acetone (Sigma-Aldrich) at 40 °C in sequence and dried in nitrogen gas. Film thicknesses, between 40 and 60 nm, were measured using atomic force microscopy (AFM, Digital Instruments CP-II, Veeco Instruments Inc.) by scratching the films with a razor blade.

A series of PS/MEH-PPV blends were also prepared using the procedure described above to make the Au/MEH-PPV nanocomposite films. One-to-one (weight ratio) PS/MEH-PPV thin film blends with polystyrene (Pressure Chemical Co.) were prepared. Different samples containing PS of M_n = 1000, 4000 and 49000 g/mol were prepared. The film thicknesses were 60 ±5 nm.

The topographies of the films were determined using contact mode AFM. The in-plane structures of Au/MEH-PPV nanocomposites and PS/MEH-PPV blends were investigated using STEM. Samples for STEM were prepared by spincoating the solutions onto glass slides; the films were then floated on ultrapure water and picked up onto copper grids. The depth distribution of the gold nanoparticles in the nanocomposites was measured by Dr. Tom Mates (University of California, Santa Barbara), using dynamic secondary ion mass spectroscopy (DSIMS), a Physical Electronics 6650 Quadrupole instrument. The absorption spectra were measured using a Varian Cary 50 Bio. A Quantamaster florometer equipped with an integrating sphere (Photon Technologies International Inc.) was used to collect photoluminescence (PL) spectra and to determine the absolute quantum yield of the nanocomposites.

3.3 Results and Discussion

3.3.1 Morphology

The nanoparticles used in this study are identified as Au(2)-PS_{10}, Au(5)-PS_{10}, Au(5)-PS_{480} and Au(5)-DT, where the number in the parenthesis represents the diameter of Au cores and the subscript denotes the number of repeat units/chain on each PS brush attached to the gold nanoparticle surfaces; the characteristics of the Au NPs are summarized in Table 3.1. Au/MEH-PPV nanocomposite thin films with different nanoparticle distributions were prepared and analyzed. STEM images, in-plane views, of the particle distributions and the topographies of the corresponding films are shown in Fig.3.1 for four different nanocomposites. Each sample was of thickness 50± 10 nm and

contained 10 wt% Au. Shown in Fig. 3.1a is an STEM image of the lateral distribution of the dodecanethiol stabilized particles (Au(5)-DT), which formed aggregates throughout the film. The SIMS profile of this sample, Fig. 3. 2a, indicates that nanoparticles primarily reside at the free surface, with a small fraction at the polymer/substrate interface. The segregation to the free surface may be understood on the basis that dodecane is incompatible with PS and possesses a lower surface energy than MEH-PPV; these issues are addressed later. A schematic of the Au(5)-DT particle distribution is shown in the inset of Fig. 3. 2a. We note, in passing, that the dodecane coated nanoparticles form aggregates with a hexagonal close packed structure; something we observed in a number of thin film mixtures involving other polymers[69].

The nanoparticle distributions in the other nanocomposite films are significantly different. We begin by discussing the nanocomposites containing the Au(5)-PS_{480} nanoparticles (Fig. 3.1b). The STEM and the AFM topography images reveal phase separation between the NPs and the host. Specifically, Fig. 3. 1b shows aggregation of the nanoparticles; the surface of the film is also rough. These factors, aggregation and surface roughness, are evidence of lateral phase separation between the nanoparticles and the host chains. The SIMS profile (Fig. 3.2b) shows a non-uniform distribution of Au(5)-PS_{480} nanoparticles throughout the film, which is consistent with this assessment. The nanoparticles Au(2)-PS_{10} and Au(5)-PS_{10} in the nanocomposites are uniformly distributed throughout the film, as indicated by the STEM, AFM and SIMS measurements (Fig. 3. 1c, 1d, 2c and 2d). No apparent clustering of particles occurred, as indicated by the STEM images. Moreover, no surface instabilities occurred; the topographies of the films were flat. The differences between the morphologies of the MEH-PPV/Au-PS_{10} (N=10)

and MEH-PPV/Au-PS_{480} (N=480) systems are associated with the fact that the interactions between the grafted PS chains and the MEH-PPV host largely determine the thermodynamics/miscibility and the morphology of the films. To understand this further, we begin by discussing the interfacial segregation of the nanoparticles. In thin films, the grafted nanoparticles would reside at the interfaces for different reasons. If the grafted molecules possess a lower surface energy than the host chains, then particles would reside preferentially at the free surface to minimize the free energy. For example, the segregation of the Au(5)-DT nanoparticles to the free surface is understood in terms of dodecane's surface energy ($\gamma_{DT\text{-}air}$ = 25.4 mJ/m^2), which is lower than that of MEH-PPV ($\gamma_{MEH\text{-}PPV\text{-}air}$ = 30.75 mJ/m^2)[70], hence the driving force for segregation to the free surface .

Experiments in our laboratory suggest that low molecular weight mixtures of PS and MEH-PPV have some degree of miscibility, whereas the high molecular weight PS molecules do not. Specifically, 1:1 mixtures of PS of molecular weight M_n=1000, 4000 and 49,000 g/mol (denoted as PS_{10}, PS_{40} and PS_{470}) were mixed with MEH-PPV, respectively. The STEM images (with better than 1 nm spatial resolution), of the thin film blends, annealed in saturated chloroform vapor for 1h and stained with ruthenium tetroxide, are shown in Fig. 3. 3. The phase boundaries between PS_{470} and MEH-PPV (Fig. 3. 3c) are clearly delineated, which is consistent with the phase separation we observed between Au(5)-PS_{480} and MEH-PPV. As the molecular weight of PS decreases, MEH-PPV and PS become more miscible; the blends of PS_{10}/MEH-PPV and PS_{40}/MEH-PPV show no clear phase boundaries (Fig. 3. 3a and b). In fact the transition from phase separation to partial miscibility occurs for a PS chains of molecular weights between M_n=4,000 and 7,500 g/mol. We then exposed the films to a solvent selective to PS,

diethyl ether, and the films were only partially (~30%) dissolved. These results also strongly suggest partial miscibility of PS with MEH-PPV.

To explore the morphology of PS/MEH-PPV blends further, deuterated PS of molecular weight M_n=4000 g/mol was mixed with MEH-PPV. The deuterium profile, determined by SIMS, of the as-cast film is shown in Fig. 3.4; it indicates that PS is distributed throughout the film. MEH-PPV has a reported glass transition temperature (T_g) of 65°C to 75°C[71, 72], and PS (M_n = 4000 g/mol) has a T_g of around 70°C. The film was subsequently annealed for 16 hours, at 120 °C, and the resulting SIMS profile shows that the d-PS chains are still distributed throughout the film. In addition, there is an enrichment of the free surface, reflecting the fact that d-PS has a lower surface energy than MEH-PPV. To this end, we note that the unfavorable positive enthalpic parameter, χ, of the high molecular weight PS/MEH-PPV mixtures is the major cause of the phase separation between Au-PS_{480} and MEH-PPV, whereas partial miscibility between low molecular weight PS and MEH-PPV is one of the factors that account for the dispersion of Au-PS_{10} NPs in the host.

The role of the nanoparticle size toward formation of the overall morphology of the system is now considered. First consider a simple case where the enthalpic interactions between the host chains and the nanoparticles can be neglected, i.e.: the free energy is dominated by entropic forces only[8-10, 73]. The translational entropy would promote distribution of the nanoparticles throughout the host, and its contribution to the free energy is $F_{trans}\sim(\varphi/D^3)\ln\varphi$, which means that for smaller the particles, with increasing curvature, the extent of dispersion throughout the host improves[74]. φ is the volume fraction of nanoparticles. Furthermore, there exists an energy penalty associated with

stretching of the host chains in order to accommodate particles that are larger than the radius of gyration of the host chains. When the radii of the nanoparticles are smaller than the radius of gyration of the host chains, nanoparticle dispersion would be favored. Finally, when the grafted chains are short, in our case, the PS_{10} ligands, they may not be able to screen the strong van der Waals attraction between two Au cores or that between an Au core and the substrate completely; the particles are prone to aggregation. Calculations have shown that such attractions are much stronger for the D = 5nm cores than for the D = 2 nm cores[50].

Indeed, our grafted chains are not chemically identical to the host chains, i.e., enthalpic interactions cannot be completely neglected. The morphology of the nanocomposites is a result of the interplay of entropic and enthalpic interactions. The systems that contained the long grafted chains exhibited phase separation, The Au(2)-PS_{10} nanoparticles were more readily dispersed throughout the MEH-PPV hosts, which may not be totally unexpected, as the low molecular weight PS chains are miscible with MEH-PPV at low concentrations. The Au(5)-PS_{10} nanoparticles are also dispersed; we, admittedly were somewhat surprised at this because of the larger size of the nanoparticles [50, 64]. To confirm our observations, we annealed the as-cast samples for different periods of time in chloroform and noted that the nanoparticle distributions remained qualitatively the same after 1 or 2 hours; there was no evidence of phase separation. The thermodynamics of this system is clearly very interesting and we have plans to further examine this system as part of a future study.

3.3.2 Fluorescence Properties

The foregoing results indicate that the spatial distribution of the nanoparticles may be controlled through changing the grafting chain length and chemistry. We now discuss the fluorescence properties of these nanocomposites, which are sensitive to sample morphology (Fig. 3. 5). We begin by examining the optical properties Au NPs, specifically the absorption and photoluminescence (PL). MEH-PPV absorbs photons which excite delocalized electrons; electrons may relax to ground state by emitting photons; this is photoluminescence.

The normalized absorption spectra of the Au nanoparticles (Fig. 3. 5a) indicate that Au(5)-PS_{10} and Au (5)-PS_{480} both exhibit surface plasmon resonance peaks at λ_{max} = 524 nm; Au(5)-DT exhibits a peak at a slightly lower wavelength, λ_{max} = 515 nm. This difference is primarily due to the difference between the refractive indices of DT (n_{DT} = 1.4) and PS (n_{ps} = 1.6). The plasmon band of Au(2)-PS_{10} the extinction spectrum is broadened significantly, due, in part, to the decreased particle size[18, 75]. Shown in Fig. 3. 5b are the absorption spectra of pristine MEH-PPV and four Au/MEH-PPV nanocomposites. Pristine MEH-PPV possesses an absorption peak at λ_{abs}= 504 nm; the incorporation of 10 wt% of Au NPs red-shifted λ_{abs} by about 0.5 – 2 nm depending on the particle type. It is known that chain packing plays an important role in the absorption and photoluminescence of conjugated polymer thin films. The presence of a substrate becomes important when the films become thin (less than 100 nm); as the chains pack differently at the substrate than in the bulk, thickness dependencies of the absorption and PL have been observed. We point out that within our controlled range of thicknesses (50 ±10 nm) and NP concentrations (0 – 15 wt %), the effect of NPs on the absorption peak

λ_{abs} is limited. No ground-state charge-transfer between the polymer and the NPs were observed.

The shapes of the PL spectra (Fig. 3. 5c) are affected by the presence of the Au NPs. The PL spectrum of pristine MEH-PPV exhibits a major photoluminescence emission peak at λ_{em}= 581 nm and another at 621nm, which can be attributed to the interaction between adjacent chains (π-π stacking)[76]. λ_{em} is redshifted by 8 nm in the presence of Au NPs and the intensity of the second peak is decreased. Au(5)-PS_{480}/MEH-PPV composite exhibits a lower second peak than the other composites with the same Au weight fraction due to its much longer grafted PS chains; in other words the presence of the larger grafted PS chains have a larger overall dilution effect than the other nanoparticles onto which shorter chains are grafted. It is generally believed that the dilution effect of a second component will result in a blue shift in the absorption and PL spectra of the emissive component[77], but our experimental results show redshifts in both λ_{abs} and λ_{em}. In fact, others have observed similar redshifts in thin MEH-PPV and composite films[76, 78]. We speculate that the presence of the nanoparticles affect the packing of the MEH-PPV chains and contribute to extending the conjugation length of MEH-PPV backbones, leading to redshifts in the absorption and PL spectra.

Nanoparticle size, spatial distribution and grafting layer thickness have a strong influence on the quenching efficiency of the nanocomposites. The fluorescence of the nanocomposites is characterized by the absolute quantum yield, determined using the integrating sphere method[79], which accounts for the difference in the amount of MEH-PPV molecules in each sample due to the variations of particle concentrations and sample thicknesses (Fig. 3.5d). The absolute quantum yield (QY) = total number of photons

emitted/total number of photons absorbed. QY of pristine MEH-PPV was determined to be 9.0%. Fig. 3. 5d shows that QY decreases monotonically with increasing concentration of Au NPs, for all nanocomposites.

It is clear that more dispersed, and smaller, particles are effective at fluorescence quenching. Based on the quantum yield of the nanocomposites containing the three larger core nanoparticles, Au(5)-DT, Au(5)-PS_{480} and Au(5)-PS_{10}, fluorescence quenching by Au(5)-PS_{10} is most efficient, for the same Au volume concentration. The fact that Au(5)-DT possesses a smaller average core size (D= 4.1 nm) than Au(5)-PS_{10} (D = 4.8 nm), and that its brush thickness, h_b(DT)=1.3 nm, is shorter than that of Au-PS_{10} ($h_b(PS_{10})$= 2.0 nm), quenching by the Au-DT nanoparticle should be most efficient[20, 23]. However, the morphologies of the nanocomposites play a dominant role toward fluorescence quenching: spatially dispersed Au (5)-PS_{10} particles quench the fluorescence of MEH-PPV more efficiently than the interfacially segregated Au(5)-DT nanoparticles and Au(5)-PS_{480} nanoparticles. Au(5)-PS_{480} nanoparticles have a weak effect on the quantum yield of MEH-PPV compared to Au(5)-PS_{10}. This difference is due largely to the thick grafted PS layers, which act as a "shield" between the surface of Au NPs and MEH-PPV chains. In principle, the amount of quenching may be tailored simply by changing h_{brush}. Furthermore, the extent of quenching is influenced by particle size, as seen in the difference between the quenching efficiencies in the MEH-PPV/Au(5)-PS_{10} and of MEH-PPV/Au(2)-PS_{10} nanocomposites, both of which possess the same morphologies (i.e. nanoparticle distributions). It is noteworthy that for a fixed Au concentration as low as 5 wt%, the fluorescence quenching ratio can be varied from 4%

to 80% by controlling the Au NP size, grafting layer thickness, and spatial distribution of NPs.

Reasons for the particle induced quenching are now discussed. The light absorption and scattering properties of an Au nanoparticle can be expressed in terms of its absorption and scattering cross sections C_{abs} and C_{sca}, the hypothetical cross sectional areas which every incident photon enters is absorbed or scattered. The sum of C_{abs} and C_{sca}, the extinction cross section C_{ext}, contributes to the total extinction spectrum of gold nanoparticles. Based on Mie theory[19, 23, 80], it is evident that as the size of a metal nanoparticle decreases, its scattering cross section decreases at a faster rate than its absorption cross section; hence the ratio of C_{abs}/C_{sca} increases as the particle becomes smaller. There exists a threshold particle size where particles absorb more light than they scatter. In a medium with a refractive index n=1.33, this threshold particle size is between 60 nm and 80 nm[80]. For a gold nanosphere with a diameter D = 20nm, extinction is almost exclusively due to absorption[23]. Hence the nanoparticles in our system, due to their sizes, should act as quenchers. The difference between the quenching efficiencies of Au(5)-PS_{10} and of Au(2)-PS_{10} is readily understood. This result is consistent with the notion that because Au(2) NPs possess a larger C_{abs}/C_{sca} ratio, they are better quenchers than Au(5) NPs.

The absorbance of fluorescent molecules can be enhanced due to the incident optical field enhancement induced by metal nanoparticles[81], while the fluorescence of such molecules in direct contact with gold nanoparticles will be quenched[20], due to an increased non-radiative decay rate R_{nonrad} and a decreased radiative decay rate R_{rad} [quantum yield = $R_{rad}/(R_{rad} + R_{nonrad})$]. The overall effect of metal nanoparticles on the

fluorescence of nearby molecules is the result of the combination of several factors: the local field, change in radiative and non-radiative decay rates and molecule-particle distance[82]. When incorporated into a fluorescent polymer host, the fact that same weight percentage of the smaller Au(2) NPs has more total surface area than Au(5) NPs also contributes to more quenching of the fluorescence.

3.4 Concluding Remarks

We have shown that the relative surface energies of the grafted molecules, the relative size of the grafted molecules, the size of the nanoparticles in relation to the host chain size, and the grafted chain/host chain interactions determine the morphology of the material. This enabled us to show that the fluorescence properties of the nanocomposites are interrelated with sample morphology.

The fluorescence of Au/MEH-PPV nanocomposites was changed by over an order of magnitude, as a fixed volume fraction of Au, by controlling the Au particle size, the spatial distribution of nanoparticles throughout the MEH-PPV host, and the brush layer thickness. The quantum yield decreased monotonically with increasing nanoparticle concentration. Smaller particles were more efficient at quenching. As the ligand chain length, h_{brush}, increased, the quenching became less efficient. This length-scale sensitivity (h_{brush}) can be exploited in many applications. The self-assembly of Au NPs – with different interparticle spacing controlled by brush length – can impact the collective optical properties of the particle aggregates, as well; which will affect the adjacent fluorophores differently. The methods described herein are straightforward and can readily be applied to different systems.

3.5 References

1. Kojima, Y.; Usuki, A.; Kawasumi, M.; Okada, A.; Fukushima, Y.; Kurauchi, T.; Kamigaito, O. *J. Mater. Res.* **1993**, *8*, 1185-1189.
2. Huynh, W. U.; Dittmer, J. J.; Alivisatos, A. P. *Science* **2002**, *295*, 2425-2427.
3. Gupta, S.; Zhang, Q. L.; Emrick, T.; Balazs, A. C.; Russell, T. P. *Nat. Mater.* **2006**, *5*, 229-233.
4. Oh, H.; Green, P. F. *Nat. Mater.* **2009**, *8*,139-143.
5. Arceo, A.; Meli, L.; Green, P. F. *Nano Lett.* **2008**, *8*, 2271-2276.
6. Winey, K. I.; Vaia, R. A. *MRS Bull.* **2007**, *32*, 314-319.
7. Daniel, M. C.; Astruc, D. *Chem. Rev.* **2004**, *104*, 293-346.
8. Degennes, P. G. *Macromolecules* **1980**, *13*, 1069-1075.
9. Borukhov, I.; Leibler, L. *Macromolecules* **2002**, *35*, 5171-5182.
10. Meli, L.; Li, Y.; Lim, K. T.; Johnston, K. P.; Green, P. F. *Macromolecules* **2007**, *40*, 6713-6720.
11. Kreibig, U.; Vollmer, M., *Optical Properties of Metal Clusters*. Springer: 1995; Vol. 25.
12. Brown, K. R.; Walter, D. G.; Natan, M. J. *Chem. Mat.* **2000**, *12*, 306-313.
13. Elghanian, R.; Storhoff, J. J.; Mucic, R. C.; Letsinger, R. L.; Mirkin, C. A. *Science* **1997**, *277*, 1078-1081.
14. Linden, S.; Kuhl, J.; Giessen, H. *Phys. Rev. Lett.* **2001**, *86*, 4688-4691.
15. Kitson, S. C.; Barnes, W. L.; Sambles, J. R. *Phys. Rev. Lett.* **1996**, *77*, 2670-2673.
16. Haynes, C. L.; Van Duyne, R. P. *J. Phys. Chem. B* **2001**, *105*, 5599-5611.
17. Dulkeith, E.; Morteani, A. C.; Niedereichholz, T.; Klar, T. A.; Feldmann, J.; Levi, S. A.; van Veggel, F.; Reinhoudt, D. N.; Moller, M.; Gittins, D. I. *Phys. Rev. Lett.* **2002**, *89*, 203002.
18. Tam, F.; Goodrich, G. P.; Johnson, B. R.; Halas, N. J. *Nano Lett.* **2007**, *7*, 496-501.
19. Fan, C. H.; Wang, S.; Hong, J. W.; Bazan, G. C.; Plaxco, K. W.; Heeger, A. J. *Proc. Natl. Acad. Sci. U. S. A.* **2003**, *100*, 6297-6301.
20. Brust, M.; Walker, M.; Bethell, D.; Schiffrin, D. J.; Whyman, R. *J. Chem. Soc.-Chem. Commun.* **1994**, 801-802.
21. Saunders, A. E.; Sigman, M. B.; Korgel, B. A. *J. Phys. Chem. B* **2004**, *108*, 193-199.
22. Meli, L.; Green, P. F. *ACS Nano* **2008**, *2*, 1305-1312.
23. Zhong, Z.; Yin, S.; Liu, C.; Zhong, Y.; Zhang, W.; Shi, D.; Wang, C. a. *Applied Surface Science* **2003**, *207*, 183-189.
24. Lee, T. W.; Park, O. O. *Advanced Materials* **2000**, *12*, 801-804.
25. Liu, J.; Guo, T. F.; Yang, Y. *J. Appl. Phys.* **2002**, *91*, 1595-1600.
26. Ferreira, P. G.; Ajdari, A.; Leibler, L. *Macromolecules* **1998**, *31*, 3994-4003.
27. Xu, J. J.; Qiu, F.; Zhang, H. D.; Yang, Y. L. *J. Polym. Sci. Pt. B-Polym. Phys.* **2006**, *44*, 2811-2820.
28. Frischknecht, A. L. *J Chem Phys* **2008**, *128*, 224902.

29. Smith, G. D.; Bedrov, D. *Langmuir* **2009**, *25*, 11239-11243.
30. Meli, L.; Arceo, A.; Green, P. F. *Soft Matter* **2009**, *5*, 533-537.
31. Link, S.; El-Sayed, M. A. *J. Phys. Chem. B* **1999**, *103*, 8410-8426.
32. Creighton, J. A.; Eadon, D. G. *J. Chem. Soc.-Faraday Trans.* **1991**, *87*, 3881-3891.
33. Shi, Y.; Liu, J.; Yang, Y. *J. Appl. Phys.* **2000**, *87*, 4254-4263.
34. Chen, H.-J.; Wang, L.; Chiu, W.-Y. *Eur. Polym. J.* **2007**, *43*, 4750-4761.
35. Marletta, A.; Goncalves, V. C.; Balogh, D. T. *J. Lumines.* **2006**, *116*, 87-93.
36. Greenham, N. C.; Samuel, I. D. W.; Hayes, G. R.; Phillips, R. T.; Kessener, Y.; Moratti, S. C.; Holmes, A. B.; Friend, R. H. *Chem. Phys. Lett.* **1995**, *241*, 89-96.
37. Jain, P. K.; Lee, K. S.; El-Sayed, I. H.; El-Sayed, M. A. *J. Phys. Chem. B* **2006**, *110*, 7238-7248.
38. Wiley, B. J.; Chen, Y. C.; McLellan, J. M.; Xiong, Y. J.; Li, Z. Y.; Ginger, D.; Xia, Y. N. *Nano Lett.* **2007**, *7*, 1032-1036.
39. Yguerabide, J.; Yguerabide, E. E. *Anal. Biochem.* **1998**, *262*, 137-156.
40. Rand, B. P.; Peumans, P.; Forrest, S. R. *J. Appl. Phys.* **2004**, *96*, 7519-7526.
41. Anger, P.; Bharadwaj, P.; Novotny, L. *Phys. Rev. Lett.* **2006**, *96*, 113002.

Table 3-1 Characteristics of the Au nanoparticles

Nanoparticle	M_n *(g/mol)*[a]	$2R_{core}$ *(nm)*[b]	h_{brush} *(nm)*[c]	$f_{ligands}$[d]	σ *(chains/nm^2)*[e]
Au(5)-DT	202	4.1 ± 0.7	1.3 ± 0.5	1:1	1.9
Au(5)-PS_{10}	1000	4.8 ± 1.3	2.0 ± 0.6	1:5	1.7
Au(5)-PS_{480}	50000	4.8 ± 1.1	26.5 ± 5.4	1:19	1.4
Au(2)-PS_{10}	1000	2.0 ± 0.9	2.0 ± 0.6	1:5	1.8

[a]M_n, molar mass (for DT) and number average molecular weight (for PS) of the ligands; [b]$2R_{core}$, the average diameter of Au cores measured from STEM images; [c] h_{brush}, thickness of the brush grafted on Au surface, estimated from the nearest neighbor distance between particles by analyzing about 100 pairs of particles in a nanoparticle monolayer film; [d]$f_{ligands}$, molar ratio of ligands : $HAuCl_4$ in the particle synthesis and [e]σ, grafting density of the ligands.

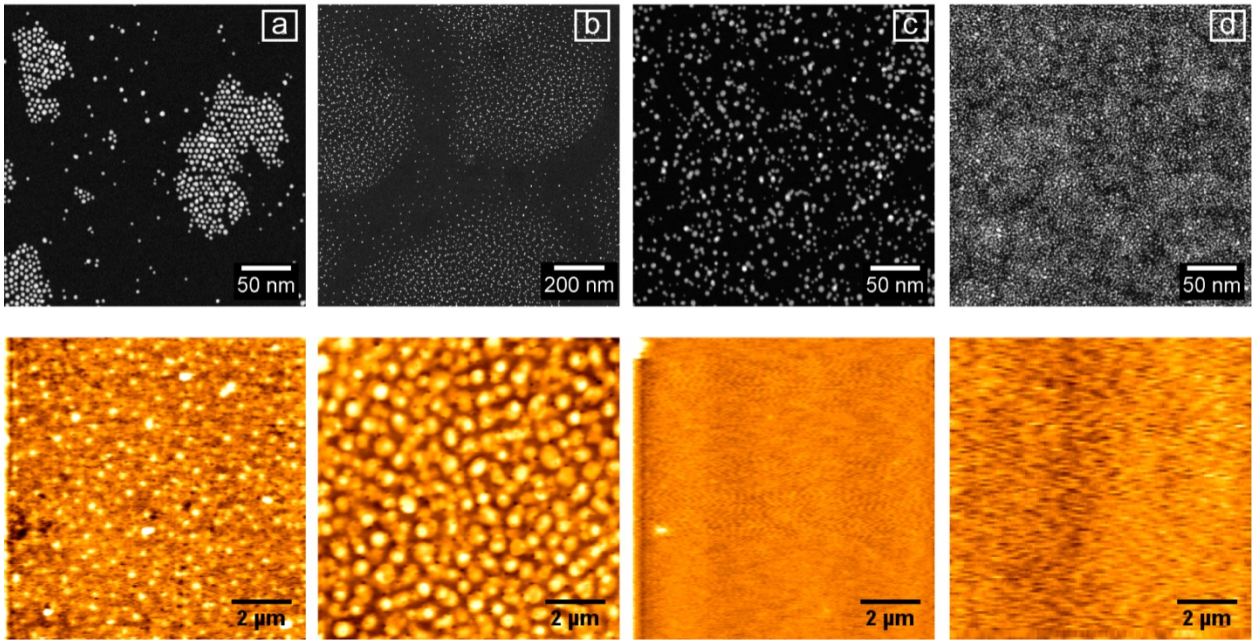

Figure 3.1 Morphology of Au/MEH-PPV nanocomposites. Shown here are STEM (top row) and the corresponding AFM (bottom row) images of 10% Au nanoparticle/MEH-PPV composite films of 40-60 nm in thickness. a, Au(5)-DT/MEH-PPV; b, Au(5)-PS_{480}/MEH-PPV; c, Au(5)-PS_{10}/MEH-PPV and d, Au(2)-PS_{10}/MEH-PPV.

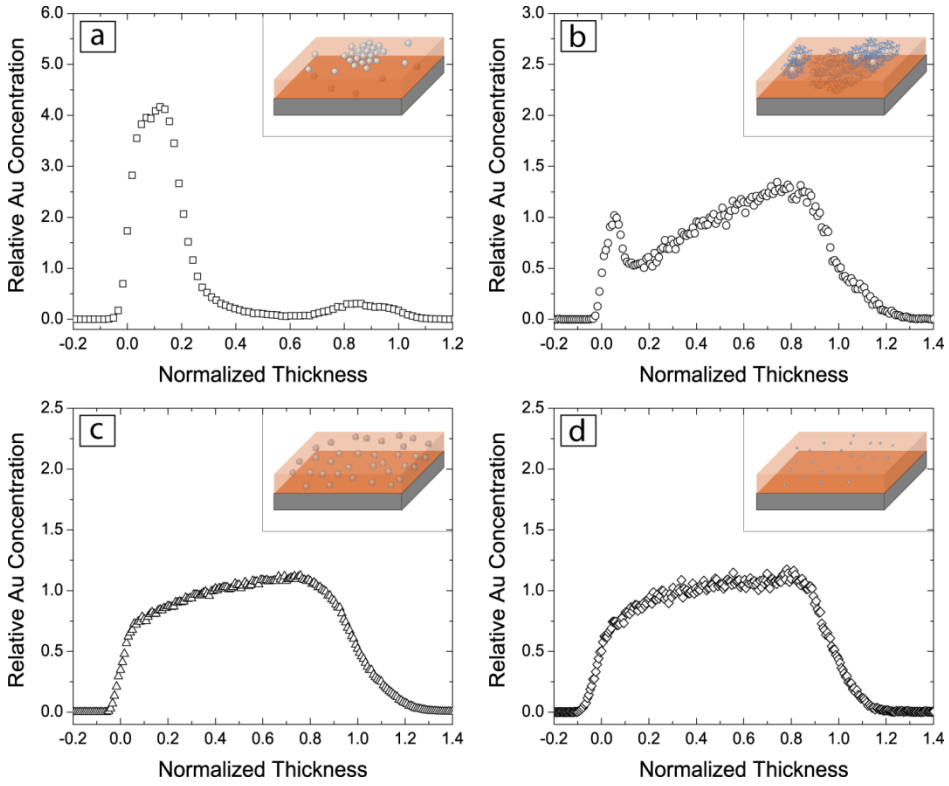

Figure 3.2 Normalized depth profiles of different Au nanoparticles in MEH-PPV, measured by SIMS, are shown here: (a), 30% Au(5)-DT/MEH-PPV; (b) 10% Au(5)-PS480/MEH-PPV; (c) 30% Au(5)-PS10/MEH-PPV and (d) 30% Au(2)-PS10/MEH-PPV. The films are approximately 150nm thick. We evaporated a layer of pure Au on top of our nanocomposites and (from the SIMS data) calculated the molar concentration of Au atoms from the ratio of signal strength of Au atoms in the composites to that of the pure (evaporated) Au layer. The thicknesses of the films were normalized for the ease of comparison where 0.0 is the free surface of the film and 1.0 is the substrate. Au concentrations were then normalized, divided by the total area under the profiles so that the integration of Au concentrations over normalized thickness is equal to 1. The insets are the schematics of the corresponding spatial distribution of nanoparticles in MEH-PPV.

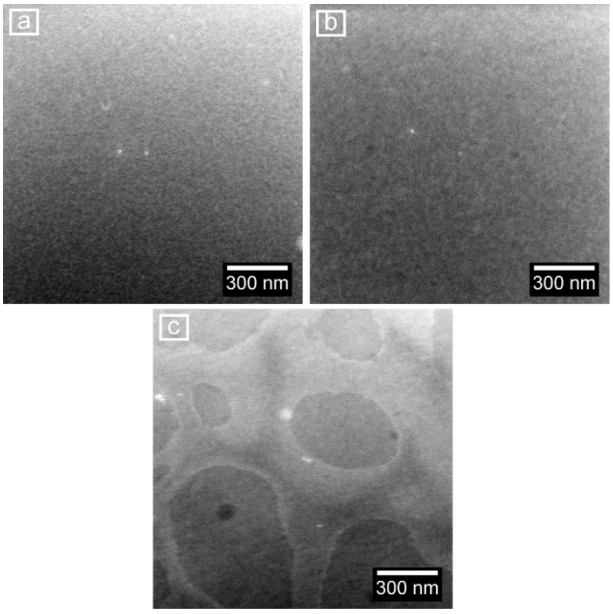

Figure 3.3 Morphology of 1:1 PS/MEH-PPV blends, the molecular weight of PS being Mn = 1000 g/mol in a, 4000 g/mol in b and 49000 g/mol in c. The thin film blends were annealed in chloroform vapor for 1h and then stained in ruthenium tetroxide vapor for 10 minutes. Images were taken on STEM.

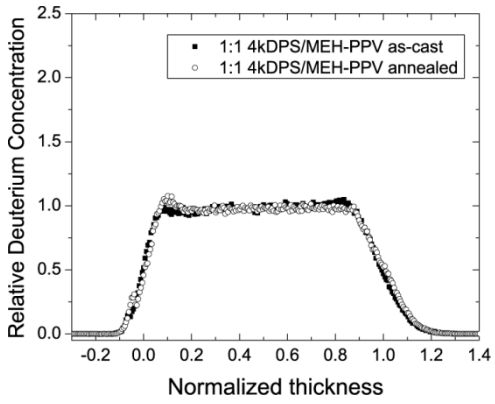

Figure 3.4 Deuterium depth profiles of thin film 1:1 mixtures of deuterated-PS with average molecular weight Mn= 4000 g/mol and MEH-PPV measured by SIMS, are shown here. Solid squares, as-cast sample; empty circles, vacuum annealed at 120 °C for 16 hours. The deuterium concentrations and thicknesses were normalized in the same way as described in Fig.3.2.

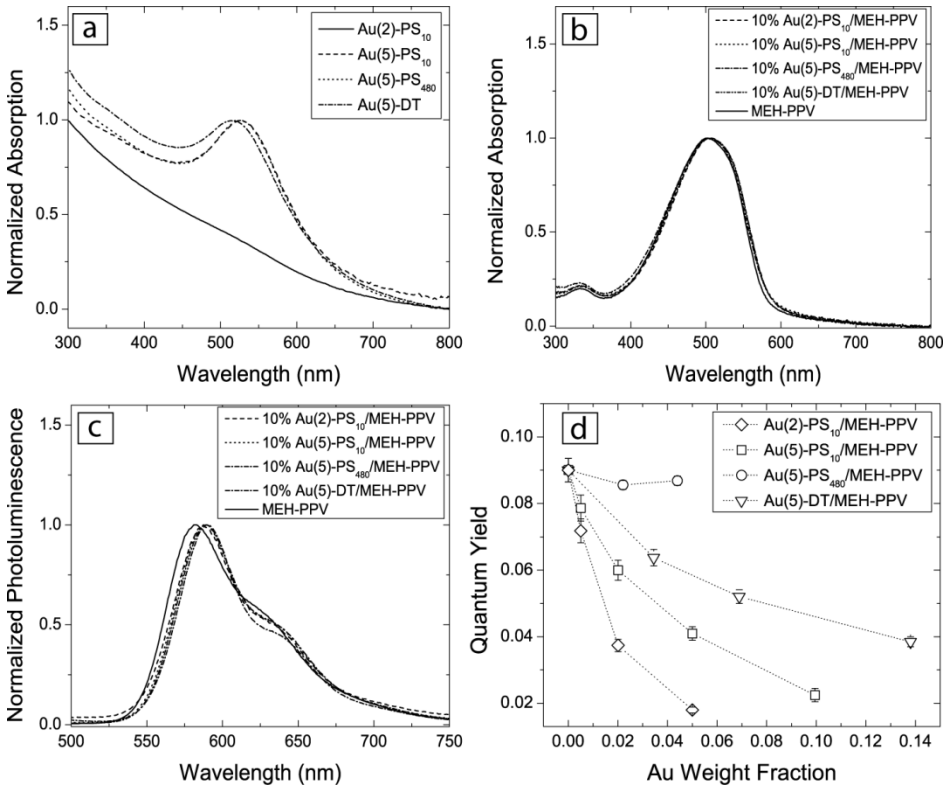

Figure 3.5 Optical properties of Au/MEH-PPV nanocomposites. a, Normalized absorption spectra of Au nanoparticles in chloroform; b and c, normalized absorption and photoluminescence (PL) spectra of Au/MEH-PPV thin films on glass and d, the quantum yield of Au/MEH-PPV nanocomposites, as a function of nanoparticle concentration. PL and quantum yield measurements were performed at excitation wavelength of 472nm. The films used for these measurements were between 40 to 60 nm in thickness.

Chapter 4

Tethered-Polymer Structures in Thin Film Polymer Melts

4.1 Introduction

A-b-B diblock copolymers, apart from self-organizing into A-rich and B-rich domains of different symmetries (cylinders, spheres, lamellae) possessing long-range order[1], exhibit significant interfacial activity, which has the effect of modifying the behavior of different systems for various applications[2-12]: the wettability of surfaces, stabilization of colloidal particles, enhancement of adhesion, and reducing the interfacial tension leading to an enhancement of the compatibility of dissimilar phases. When dissolved in a selective solvent, A-b-B copolymers can self-assemble into micelles that can be employed for applications that include the sequestration nanoparticles[13] as well as for drug delivery applications[14, 15].

Micelle formation in block copolymer/homopolymer mixtures has been of interest, both theoretically[16-21] and experimentally[4, 5, 22-27] for nearly three decades, yet there remain important unresolved questions, particularly in relation to the role of confinement on the formation and organization of micelles. In a selective solvent environment, such as a homopolymer of type-A, the A-b-B diblock copolymer chains of sufficiently low concentration form micelles with an inner core composed of the B-component and a corona composed of the A-component. Based on the asymmetries between the degrees of

polymerization of the two blocks, N_A and N_B, the Flory-Huggins interaction parameter χ and the composition, micelles of different geometries may form[15, 21, 28]. For example, when N_A is much larger than N_B, the micelles are spherical. Liebler et al.[16] calculated the free energy of formation of micelles in a copolymer/homopolymer melt under conditions where the homopolymer chains of type A, of degree of polymerization P, were sufficiently short such that they readily intermixed with the corona. They predicted that the copolymers would aggregate to form micelles at concentrations greater than a critical micelle concentration (cmc), which is a function of χN_B, in order to minimize the unfavorable A/B contacts. The calculations were restricted to the case of symmetric copolymers, where N_A=N_B. Whitmore and Noolandi[17] subsequently extended the work to include the effects of varying N_A, N_B and P on the structure of the system. Shull et al.[23] showed that the micelles exhibited a tendency to migrate to interfaces in thin films, thereby demonstrating the role of micelle-interfacial interactions on the structure of the mixtures. Esselink et al.[24] described the interactions between deuterated polystyrene-*b*-poly(2-vinylpyridine) (dPS-b-P2VP) micelles in thin film polystyrene (PS) hosts, revealing the possibility of the formation of an ordered phase of micelles. More recently, Cavallo et al.[21] used coarse-grained, Monte Carlo, lattice simulations to understand the role of an interacting interface on the structure of the copolymer/homopolymer system. They predicted a "diagram of states", which described the conditions under which different phases (bulk and surface micelles, brush layers, free copolymer chains) would coexist.

Some time ago it was shown that symmetric polystrene-*b*-polymethyl methacrylate (PS-b-PMMA) diblock copolymers, $P>>N$) at concentrations below $\varphi_{cmc,}$

segregated to the SiO_x substrate, leaving free copolymer chains in the interior of a thin film PS-b-PMMA:PS/SiO_x mixture[3]. In a more recent study[29], our group found that PS-b-PMMA diblock copolymers preferentially adsorbed onto the substrate to form a brush layer at concentrations even for $\varphi > \varphi_{cmc}$, prior to micelle formation, provided the film was sufficiently thin. In the study described herein, we examine the conditions that determine the equilibrium number and dimensions of the micelles and the brush layer thickness in thin film polystyrene-*b*-poly(2-vinylpyridine) (PS-b-P2VP)/PS mixtures. The effects of host molecular weight on the micellar core sizes, micelle-micelle interactions and on the corona/homopolymer interactions are discussed. The effects of the host molecular weight on the equilibrium of the system, between the copolymer chains in the micelles, those adsorbed onto the surface to form the brush layer and the free copolymer chains in the system are also examined. The behavior of these thin film systems is compared to PS thin film systems containing nanoparticles onto which PS chains of degree of polymerization N are grafted.

4.2 Experimental

Solutions of the diblock copolymer polystyrene-*b*-poly(2-vinylpyridine) (PS-b-P2VP, Polymer Source Inc.) and a series of PS homopolymer with different molecular weights, ranging between 13,000 and 1,600,000 g/mol (Pressure Chemical Co.), were prepared in toluene. The number average molecular weights of the components of the diblock are M_n (PS)= 50,900 and M_n(P2VP)=29,100; their degrees of polymerization were N_{PS}=489; N_{P2VP}= 277; N = 766 and the polydispersity index PDI = 1.06). These solutions were blended so that the weight ratio of the diblock copolymer to PS

homopolymer is 1:4. For the study of the brush layer, the blended solutions were spincoated onto Si_3N_4 substrates (WaferNet, Inc.); for the study of the micelle formation, they were spincoated onto glass slides, and the films were floated from deionized water and picked up on Si_3N_4 (grids) substrates (Structure Probe, Inc). The thickness of the films was controlled to be 110 ± 4 nm, measured using a variable angle spectroscopic ellipsometer (J.A.Woollam Co., Inc.), and fitting the ellipsometric angles, Δ and Ψ, to a Cauchy model in the WVASE32 software. The films were subsequently dried in vacuum at 65 °C for 24 hours and then annealed at 160 °C for 8 to 72 hours.

For the study of the brush layer, the films, after annealing, were gently washed in toluene, a selective solvent for PS, in order to expose the underlying brush layer in contact with the substrate. After washing with toluene, the films were dried in vacuum at 65 °C for overnight and then annealed at 160 °C for 24 hours. The thicknesses of the brush layers were then determined using ellipsometry, and independently by scanning probe microscopy (SPM, Asylum Research) after scratching them with a razor blade.

Scanning transmission electron microscopy (STEM), using a spherical aberration corrected JEOL 2100F instrument with a high angle annular dark field detector, was used to investigate micelle formation of PS-b-P2VP chains in thin film PS hosts. Prior to analysis the films were stained in iodine vapor for 10 seconds to 5 minutes in order to make the P2VP component visible. The size of the micellar cores and the number density of the micelles were calculated in ImageJ software; groups of at least 100 micelles from three different areas of each film were analyzed. The following experimental detail is worth mentioning: the size of the micelles stained in iodine vapor for 10s, 1min and 5

min changed by less than 3%, which is within the range of experimental error; the samples examined in our experiments were stained for less than 5 minutes.

The depth profiles of the micelles (specifically the P2VP block) were measured using secondary ion mass spectroscopy (SIMS). These measurements were performed on a Physical Electronics 6650 Quadrupole instrument, by Dr Tom Mates, the University of California, Santa Barbara. The samples that were analyzed by SIMS were of the following configuration: a thin layer of deuterated-PS is in contact with the outer surface of the copolymer homopolymer thin film mixture, which was supported by the substrate. The deuterated-PS layer is necessary to ensure a constant etch rate, hence consistency, in the SIMS experiments. Profiles of individual elements or fragments of the molecules,, including Si, H, D, carbon, CN, in the samples were readily determined by the measurement.

4.3 Results and Discussion

In thin film A-b-B diblock copolymer/A-homopolymer mixtures supported by a substrate, the copolymer chains generally exhibit a tendency to aggregate to form micelles, possessing an inner core of the B-component, and an outer corona of the A-component, and may segregate to one, or both interfaces, forming a brush layer, in order to minimize the free energy of the entire system. Brush layers would be absent if the A-homopolymer chains were preferentially attracted to the substrate and to the free surface. Since PS possesses a lower surface energy than P2VP, PS resides at the free surface; the P2VP component exhibits a preferential affinity for the more polar substrate[23, 29]. In our system, micelles possessing a P2VP-core and PS-corona would form and a PS-b-P2VP

brush layer would develop at the substrate. The STEM images in Fig.1 reveal that spherical micelles develop in all the PS hosts, regardless of their degrees of polymerization, P, after annealing. In these images, the P2VP cores appear to be bright, due to staining by iodine. Three things are evident from Fig.1 and Fig.2: 1) the micellar cores increase in size with increasing PS host molecular weight, reaching a plateau for $P \geq 5660$ ($M_n \geq 590$K); 2) the number density of micelles decrease with increasing P, reaching a plateau in the same regime of P where core size becomes constant; 3) the organization of the micelles exhibit hexagonally close-packed symmetry in higher molecular weight PS hosts ($P \geq 5660$, Fig. 1e-1g). The data in Fig. 2a reveal that the average diameter of the micellar core, D_{core}, increases from 22 nm when $P = 125$ hosts to a value of 42± 5 nm for $P \geq 5660$ ($M_n = 590$K). We note that micelles were fully developed within a few hours of annealing and the size of the micelles remained constant with further annealing.

The rationale behind the decrease in diameter of the micellar cores with decreasing P is now discussed. It is known that the size of the micelles is determined by a balance between the following factors: the interfacial tension between the A and B species, which favors the formation of large micelles, the stretching energy of the copolymer chains that compose the micelles, which favors smaller micelles, and the translational entropies of the free copolymer and the homopolymer host chains.[16] In the limit where $P >> N_{PS}$, the homopolymer chains would be largely excluded from the micellar coronas. This would be the so-called "dry brush" regime. Note that under dry-brush conditions, there is a finite penetration depth, λ, between the homopolymer chains and chains end-graded onto a surface, which is proportional to the relative length of the

grafted chains to the homopolymer chains, $\lambda \sim N/P$,.[30] In this regime the core size and the micellar size would be largest.

Shull et al.[23] showed that under conditions where $P>>N_{PS}$ the radius of micelle core would be

$$R_{core}^3 = \frac{3}{4\pi}\frac{gQ}{\rho_0}N_{core} \qquad 1.$$

and the radius of the micelle would be specified by $R_{micelle}^3 = \frac{3Q}{4\pi\rho_0}N_{core}$. In these equations N_{core} is the degree of polymerization of the blocks that comprise the micelle core, ρ_0 is the reciprocal of the segmental volume, $g=N_{core}/N$, and Q is the number of chains per micelle, specified by

$$Q = (\chi^{\frac{1}{2}} g\rho_0 a^3 N_c)/(0.337 - 0.194g^{\frac{1}{3}}) \qquad 2.$$

Using the following information, ρ_0=9.4x10^{-3} mol/cm^3, χ=0.11, a=0.69 nm, N_{core}=277, N=766 and g=0.362 we calculated that $R_{micelle}$= 30 nm. The micellar core diameter was calculated to be $D_{core}=2R_{core}$=44 nm, which is in excellent agreement with the experimentally determined values (Fig. 2a). In this regime, the average diameter of the cores should be largest.

The rationale behind the decrease in D_{core} with decreasing P is two-fold. As P decreases, the penetration depth λ of the homopolymer chains into the corona begins to increase, as it is proportional to N_{PS}/P. D_{core} largely remains constant in this region, as indicated by our experimental results, when $P \geq 5660$, see Fig.2. As P further decreases, to below a threshold value, P_m, the host chains readily intermix with the corona, the so-called "wet-brush" regime. The intermixing between the host chains and the corona

causes the stretching of the corona block, which leads to a smaller micellar core to maintain constant segmental density in the cores. Equally importantly, in this regime, host chains gain translational entropy due to the intermixing with the corona, which directly leads to a decrease in the aggregation number of the micelles, in order to maximize the total contact area between the host chains and the corona. We estimate that the threshold value P_m, which is the transition from dry to wet brush regime, is $3N_{PS} < P_m < 11N_{PS}$. We will later return to the implication of the location of this transition, $P_m/N_{PS}>3$, as we compare the behavior of this system with the chain end-tethered surfaces with fixed number of chains per unit area Σ_0.

SIMS was used to determine the depth profiles of the micelles and the brush layers of copolymer chains that adsorbed to the substrates of the samples. The SIMS experiments directly measured the CN group concentration, which provides direct information about the PVP component. SIMS data, plotted in Figure 4a for the case PS host of P=15400 ($P>>N_{PS}$), reveal that the micelles are located preferentially at the free surface. The micelles are more uniformly distributed throughout the sample, as expected due to the enhanced intermixing between the host chains and the corona of the micelles, as shown in Figure 4b for the sample containing PS host chains of P=125. Note that the average size of the micellar core estimated from the data is consistent with that obtained from STEM images.

In addition to the micelles, evidence of the brush layer is also clear from the SIMS profiles in both Figures. For the case of $P >> N_{PS}$, the brush layer is approximately h_{brush}=19 nm. Since the depth resolution of SIMS is ~15 nm, we prepared standards of known thicknesses and compared the normalized SIMS profiles of all the samples. This

allowed us to accurately estimate the thickness of the brush layer. The brush layer of the other sample (Fig. 4b) is necessarily smaller, as expected. The dependence of h_{brush} as a function of P is plotted in Fig. 3 (circles); h_{brush} increases with increasing P and appears to reach a plateau.

It turns out that another means by which the brush layer may be determined is to rinse the films with toluene (a poor solvent for P2VP), which removes the PS component, thereby exposing the underlying diblock brush layer. The thicknesses of the brush layers, h_{brush}, are plotted as a function of host PS molecular weight in Fig. 3 (squares); h_{brush} increases with increasing P and approaches a plateau at high P. The maximum brush thickness P is consistent with the conclusions drawn from the SIMS data. Our experiments show that in the pure diblock copolymer the layer in contact with the substrate is of thickness $L/2=L_{PS}+L_{P2VP}=22$ nm$> h_{brush}$. Using the parameters mentioned earlier, we calculate the interlamellar spacing, in the strong segregation limit, to be $L = aN^{2/3}\chi^{1/6}=40$ nm, which agrees well with our experimental results. Recall that equilibrium of the system must be established between the copolymer chains in the micelles, those adsorbed onto the surface to form the brush layer and the free copolymer chains in the system. Hence the homopolymer chains would always have some degree of intermixing with the PS components in the micelles and the brush layer. This implies that the brush in the blend is never pure even in the high *P* regime; so it never reaches the ideal copolymer case.

Similarities between the structural organization of this system and that of polymer brush-grafted nanoparticles in a thin film homopolymer melt[31] are noteworthy and provide insight into the physics of tethered entities in confinement. In reference 31, we

found that for Au nanoparticles possessing core a diameter of 4.3 nm, onto which the chains are grafted, in a PS melt, the transition between wet-brush to dry-brush transition occurred when P/N = 1.5; this transition is slightly higher than the predicted value of P/N>1 for a planar surface. This is not unexpected; for a spherical surface the effective grafting density $\Sigma_{sphere}<\Sigma_{planar}$; hence the lower effective grafting density, associated with the curvature of the nanoparticles, is responsible for shift the transition to a larger value of P/N. Therefore, the lower effective grafting density on curved surfaces is responsibility for enhanced miscibility, compared to planar surfaces.

The images in Fig. 1 and 2 indicate that the micellar core size is largest for $P>3N_{PS}$, and decreases with decreasing P. The decrease is, in part, consistent with intermixing between the host chains and the micelle coronas in the "wet" brush regime.[30] Here the chains that compose the corona would stretch in order to accommodate intermixing with the free P-mer host chains; concurrently the P2VP blocks in the core would have to become compressed in order to maintain a constant segmental density. There is however an important additional consideration with regard to the structure of the micellar system, which we will now describe.

The fundamental difference between the spherical micelle system and the chain end-tethered hard spheres is that the grafting densities, Σ_0, as well as the core size, of the chain end-tethered hard spheres are fixed; this has important consequences on the structure of the system. We determined that in the regime $P_m=3N_{PS}$, where the average micelle diameter remains constant, D=44 nm, the micelle "grafting density" (the total number of PS blocks in one micelle/surface area of the core) is $\Sigma_{micelle}$ =0.17 chains/nm^2. The values of the "grafting densities" for mixtures containing the three lowest values of P

are $\Sigma_{micelle}$ =0.09, 0.11 and 0.14 chains/nm^2, for P=125, 470 and 1460, respectively. For these calculations we used the experimentally determined D_{core} to calculate the volume of the core, from which the number of copolymer chains in a micelle was determined (M_n(P2VP)=29100 g/mol; density of P2VP is 1.18 g/cm^3, density of PS is 1.045 g/cm^3). This enabled the calculation of $\Sigma_{micelle}$. Clearly, the "grafting density" $\Sigma_{micelle}$ of the micelles decreased as the size of the P-mer host chains decreased. There appears to be two contributions to the reduction of the core size of the micelle: a reduction in the number of chains/micelle and presumably stretching of the corona and the associated shrinking of the chains in the core. The translational entropy of the free P-mer chains is enhanced with a larger number of micelles, and smaller micelles, each possessing lower "grafting densities." This reduces the elastic energy associated with stretching of the corona chains to accommodate the P-mer chains.

It was just shown that decrease of D_{core} with decreasing P (accompanied by an increase of $n_{micelle}$) is consistent with the notion that the micellar system has an ability to reduce the number of chains/micelle, and decreasing micellar size, as P decreases. In the regime $P>3N_{PS}$ D_{core}=constant and $\Sigma_{micelle}$ =0.1 chains/nm^2. The grafting density of the tethered surface where the wet-brush/dry-brush transition occurred for P/N~1 was Σ_0~1.5 chains/nm^2, in other words $\Sigma_0 >> \Sigma_{micelle}$. That this wet-brush to dry-brush transition occurred for $P_m >> N_{PS}$, instead of $P^* \sim N_{PS}$, is not surprising. The size of the *P-mer* chains must necessarily be large in comparison to N_{PS} in order to reach the dry-brush condition for these smaller values of $\Sigma_{micelle}$, compared to Σ_0.

The interactions between the micelles are now further discussed in light of the behavior of chain end-tethered nanoparticles. In a thin film polymer brush-coated

nanoparticle/homopolymer system, assuming the size of the nanoparticle cores is sufficiently large, and the brush is relatively short compared to the homopolymer host chains, the nanoparticles form close-packed aggregates and they segregate towards both the free surface and the substrate of the film. The data in Figures 1d-1f show aggregation of micelles into close packed structures, at large P. There is no correlation between the positions of the micelles shown in Figures 1a-1c. Note that it is only when the density of micelles is low that it becomes clear that local aggregates of micelle reside throughout the films. Semenov et al.[18, 24] used analytical mean field theory to calculate the interaction strength between micelles and found that there exists a long range attraction between micelles when the host homopolymer molecular weight exceeds a critical value, $P > P^*$:

$$P^* \approx 0.66\,(1-f)^{4/3} N(\chi N)^{-1/9} f^{-2/9}(1-f^{1/3})^{-2/3}(1.74-f^{1/3})^{2/9} \qquad 3.$$

where $N = N_{PS} + N_{P2VP}$, $f = N_{P2VP}/N$. The maximum energy of attraction U_{attr}, is proportional to the diameter of the entire micelle, $D = D_{core}+2h_{corona}$, suggesting an increasing micelle-micelle attraction with increasing micelle size. For our systems this prediction indicates that $P^* = 492 \sim N_{PS}$, suggesting that host molecular weight larger than 51,000 g/mol. the micelles should attract each other. However, micelle interactions (attraction, hence aggregation) were observed only for values of $P_m > 3N_{PS}$ instead of the predicted value of $P^* \sim N_{PS}$. The theory is, nevertheless, qualitatively correct in predicting the attraction between the micelles, which should occur at sufficiently large P.

In light of this discussion of micelle-micelle interactions, it is worthwhile to note that Matsen and Gardiner[32] showed that there should exist a finite interfacial tension

between the corona (brush) layers and the host chains, which should increase with increasing *P*. This would be another source of the long-range attraction between the micelles, as it leads to a reduction of the brush/free chain interfacial area. The attraction between the micelles would lead to the formation of close packed structures.[18, 24] In prior studies, we have observed the interfacial segregation of grafted spherical particles, despite the fact that the grafted chains and the host chains are of identical chemical structure.[33,34] The segregation occurs because the host chains gain configurational entropy and the tethered chains suffer a smaller loss in conformational entropy than the linear chains when they reside at the interfaces. These are also the reasons that the micelles migrate to the free surface, as shown by the SIMS profile when $P>>N_{PS}$.

4.4 Conclusions

We showed that in thin film PS-b-P2VP/PS diblock copolymer systems that micelles with an inner core of the P2VP-component and corona of the PS-component form within the PS host. The copolymer chains, in addition to forming micelles, also adsorb onto the substrate, with the P2VP-component exhibiting strong attraction, forming a brush layer. At equilibrium the chemical potential of copolymer chains in the micelles, $\mu_{micelle}$, and at the substrate, $\mu_{substrate}$, as well as that of the free chains, μ_{free}, must be equal; this determines the size of the micelles and the thickness of the brush layer. The micellar core diameter, D_{core}, increased with increasing degree of polymerization of the homopolymer, *P*, and became constant at large P, under the so-called dry-brush conditions. The increase in D_{core} was accompanied by a decrease in the number density of micelles; the number density of micelles reached a constant value at large P.

Additionally, the copolymer brush layer thickness increased with increasing P, reaching a plateau at large P. In the large P regime the micelles aggregated to form close packed structures and resided preferentially at the free surface in an effort to minimize the free energy of the system. In contrast to brush coated nanoparticle systems, where the grafting density of fixed, Σ_0, the micellar system has the ability to reduce the micellar size, in part by reducing the number of chains/micelle, and increasing the number of micelles, each possessing a lower grafting density. This has the effect of increasing the translational entropy of the free host chains and minimizing the elastic energy the corona blocks must undergo in order to accommodate intermixing with the host chains.

4.5 References

1. Bates, F. S.; Fredrickson, G. H. *Annual Review of Physical Chemistry* **1990,** 41, 525-557.
2. Green, P. F.; Russell, T. P. *Macromolecules* **1991,** 24, (10), 2931-2935.
3. Green, P. F.; Russell, T. P. *Macromolecules* **1992,** 25, (2), 783-787.
4. Shull, K. R.; Kramer, E. J.; Hadziioannou, G.; Tang, W. *Macromolecules* **1990,** 23, (22), 4780-4787.
5. Retsos, H.; Terzis, A. F.; Anastasiadis, S. H.; Anastassopoulos, D. L.; Toprakcioglu, C.; Theodorou, D. N.; Smith, G. S.; Menelle, A.; Gill, R. E.; Hadziioannou, G.; Gallot, Y. *Macromolecules* **2002,** 35, (3), 1116-1132.
6. Costa, A. C.; Geoghegan, M.; Vlcek, P.; Composto, R. J. *Macromolecules* **2003,** 36, (26), 9897-9904.
7. Green, P. F. *Journal of Polymer Science Part B-Polymer Physics* **2003,** 41, (19), 2219-2235.
8. Brown, H. R.; Deline, V. R.; Green, P. F. *Nature* **1989,** 341, (6239), 221-222.
9. Oslanec, R.; Costa, A. C.; Composto, R. J.; Vlcek, P. *Macromolecules* **2000,** 33, (15), 5505-5512.
10. Ruzette, A.-V.; Leibler, L. *Nat Mater* **2005,** 4, (1), 19-31.
11. Yokoyama, H.; Kramer, E. J. *Macromolecules* **2000,** 33, (5), 1871-1877.
12. Dai, K. H.; Kramer, E. J. *Journal of Polymer Science Part B-Polymer Physics* **1994,** 32, (11), 1943-1950.

13. Meli, L.; Li, Y.; Lim, K. T.; Johnston, K. P.; Green, P. F. *Macromolecules* **2007,** 40, (18), 6713-6720.
14. Zhan, Y.; Mattice, W. L. *Macromolecules* **1994,** 27, (3), 677-682.
15. Gohy, J. F., Block copolymer micelles. In *Block Copolymers Ii*, Springer-Verlag Berlin: Berlin, 2005; Vol. 190, pp 65-136.
16. Leibler, L.; Orland, H.; Wheeler, J. C. *Journal of Chemical Physics* **1983,** 79, (7), 3550-3557.
17. Whitmore, M. D.; Noolandi, J. *Macromolecules* **1985,** 18, (12), 2486-2497.
18. Semenov, A. N. *Macromolecules* **1992,** 25, (19), 4967-4977.
19. Pepin, M. P.; Whitmore, M. D. *Macromolecules* **2000,** 33, (23), 8644-8653.
20. Uneyama, T.; Doi, M. *Macromolecules* **2005,** 38, (13), 5817-5825.
21. Cavallo, A.; MuÌˆller, M.; Binder, K. *Macromolecules* **2008,** 41, (13), 4937-4944.
22. Winey, K. I.; Thomas, E. L.; Fetters, L. J. *Macromolecules* **1991,** 24, (23), 6182-6188.
23. Shull, K. R.; Winey, K. I.; Thomas, E. L.; Kramer, E. J. *Macromolecules* **1991,** 24, (10), 2748-2751.
24. Esselink, F. J.; Semenov, A. N.; Tenbrinke, G.; Hadziioannou, G.; Oostergetel, G. T. *Physical Review B* **1993,** 48, (18), 13451-13458.
25. Koizumi, S.; Hasegawa, H.; Hashimoto, T. *Macromolecules* **1994,** 27, (22), 6532-6540.
26. Floudas, G.; Hadjichristidis, N.; Stamm, M.; Likhtman, A. E.; Semenov, A. N. *Journal of Chemical Physics* **1997,** 106, (8), 3318-3328.
27. Adedeji, A.; Lyu, S.; Macosko, C. W. *Macromolecules* **2001,** 34, (25), 8663-8668.
28. Shull, K. R. *Macromolecules* **1993,** 26, (9), 2346-2360.
29. Oh, H.; Green, P. F. *Macromolecules* **2008,** 41, (7), 2561-2566.
30. Borukhov, I.; Leibler, L. *Macromolecules* **2002,** 35, (13), 5171-5182.
31. Chen, X. C.; Green, P. F. *Soft Matter* **2010**, ASAP.
32. Matsen, M. W.; Gardiner, J. M. *Journal of Chemical Physics* **2001,** 115, (6), 2794-2804.
33. Meli, L.; Arceo, A.; Green, P. F. *Soft Matter* **2009,** 5, (3), 533-537.
34. Kim, J.; Green, P. F. *Macromolecules* **2010,** 43, (3), 1524-1529.

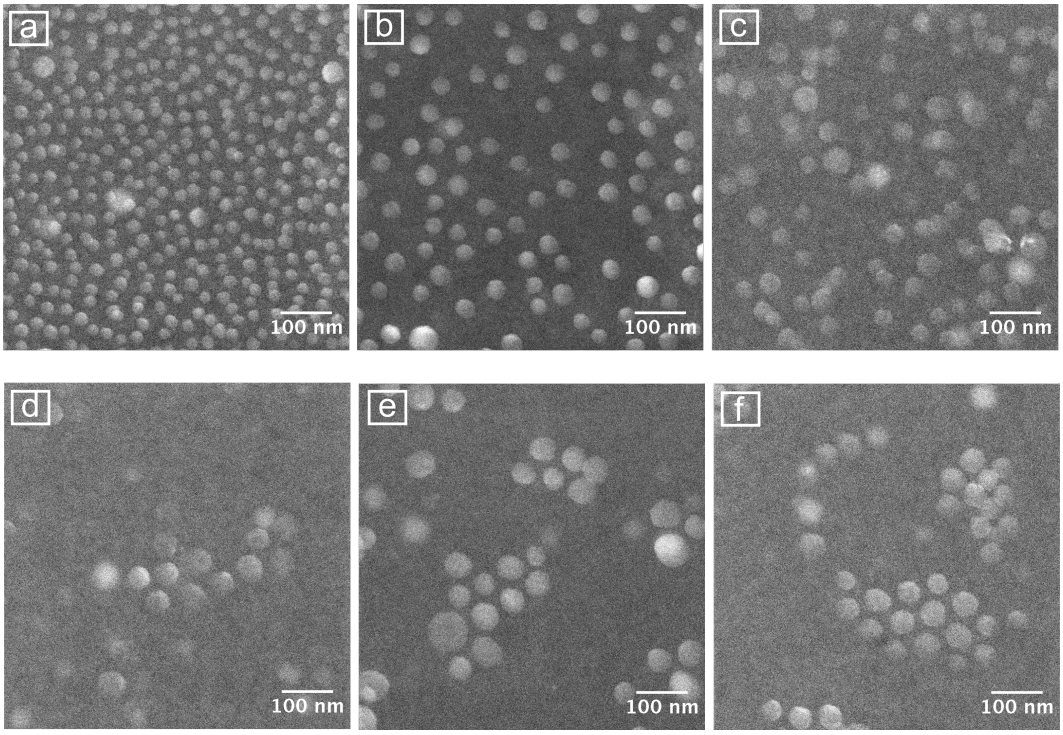

Figure 4.1 Scanning transmission electron micrographs (STEM) of 20% PS-b-P2VP in PS homopolymers with degree of polymerization of *P* = 125(a), 470(b), 1460(c), 5660(d), 8640(e) and 15400(f) are shown. All films were approximately 110 nm, annealed in vacuum at 160 °C and stained in iodine vapor.

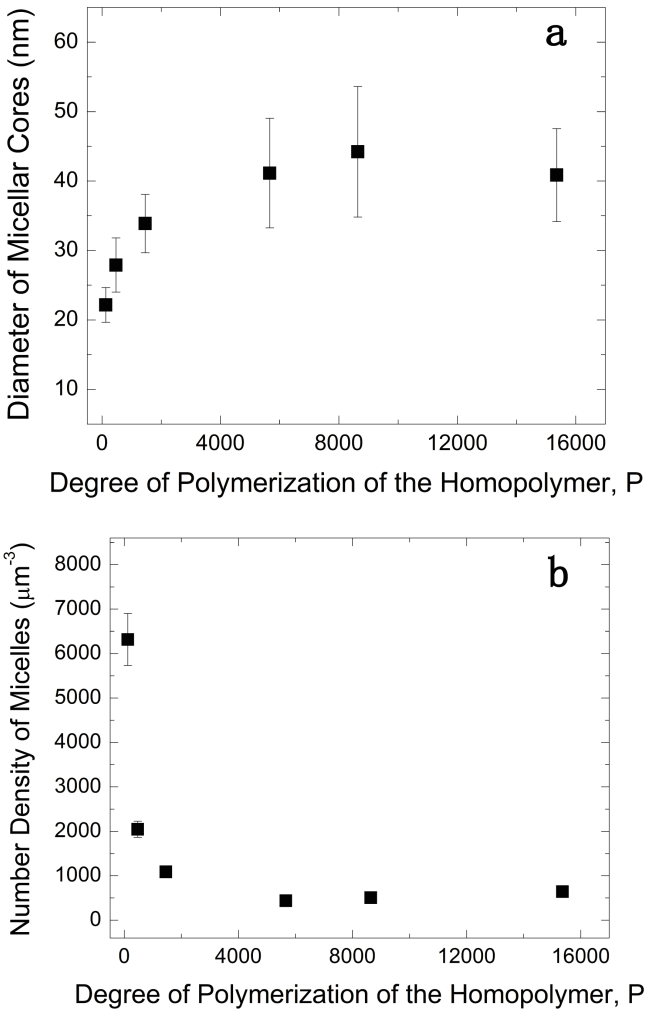

Figure 4.2 (a) the dependence of the micelle core diameter and (b) the number density of micelles are shown here as a function of the host molecular weight.

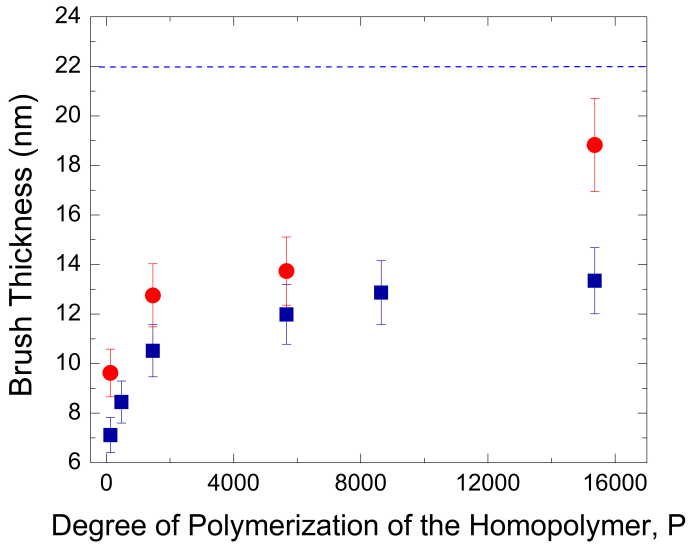

Figure 4.3 The brush layer thicknesses as a function of the molecular weight of host homopolymer. The circles represent the brush thicknesses measured using SIMS and the squares were determined from samples subjected to the toluene washing process. The dashed line represents the brush thickness of a pure PS-b-P2VP thin film of h=L/2.

.

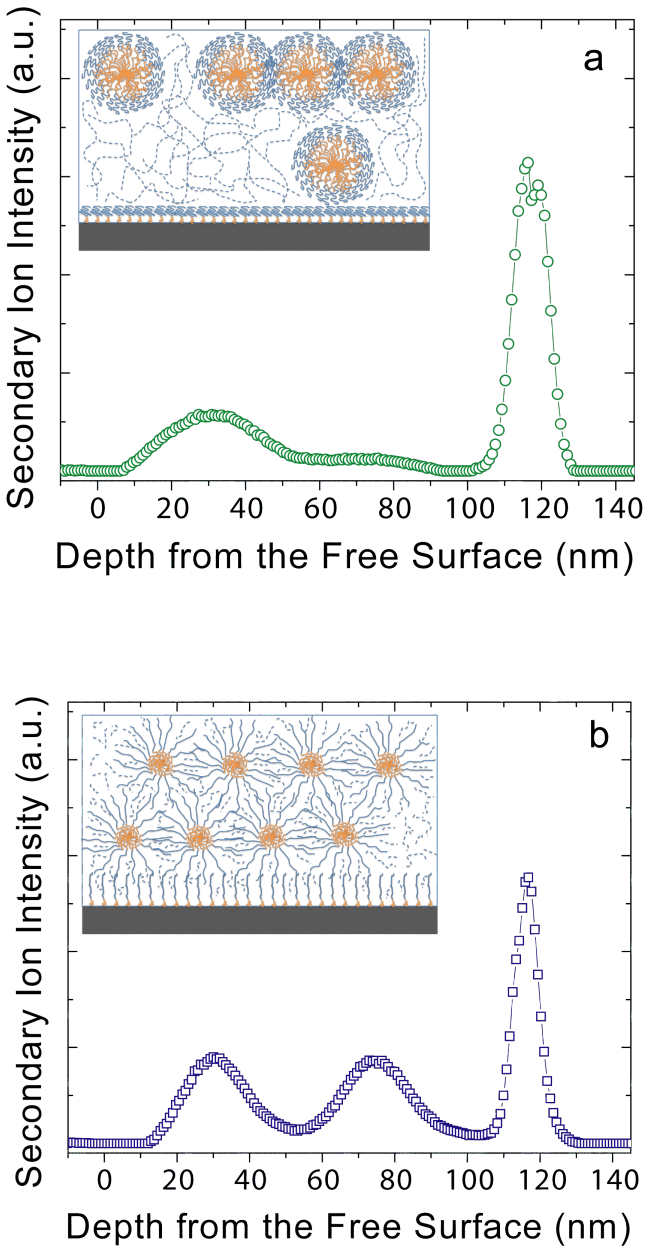

Figure 4.4 The depth profiles of P2VP in the PS-b-P2VP/PS(P=15,400) sample (part a), and of the PS-b-P2VP/PS (P=125) sample (part b), measured by SIMS, are shown. The insets are schematics of the corresponding morphologies of the films.

Chapter 5

Micelle Formation in Thin Film Homopolymer/Diblock Copolymer Blends: Role of Enthalpy

5.1 Introduction

A-*b*-B diblock copolymers, consist of two contiguous blocks of monomers, A and B, often incompatible, exhibit rich interfacial behavior. When dissolved into a selective solvent, say, a homopolymer consist of H monomers, at a low concentration, they can self-assemble into micelles of various shapes, such as spheres, cylinders, lamellae, and vesicles[1]. The self-assembly of diblock copolymers has important applications in sequestration of nanoparticles, drug delivery systems, and bottom-up nanotechnologies including copolymer lithography and membranes. The vast majority of research done on the topic has focused on the case where the homopolymer H is identical to one of the blocks of the copolymer[2-11], i.e. H = A, $\chi_{H\text{-}A} = 0$, $\chi_{A\text{-}B} = \chi_{H\text{-}B} > 0$, where $\chi_{A\text{-}B}$ is the Flory-Huggins interaction parameter between A and B blocks, and $\chi_{H\text{-}A}$ and and $\chi_{H\text{-}B}$ are those between the homopolymer H and block A, and between H and B, respectively. For such an A-*b*-B/A system, the structure of the micelles formed is determined by the degrees of polymerization of A and B blocks, N_A and N_B, the degree of polymerization of the host homopolymer, P, $\chi_{A\text{-}B}$, and the concentration[3].

From a practical point of view, we need to be able to precisely tune the structure of the micelles to match the requirement of a specific application, for example, a specific size or shape of the micelles. This can be achieved by varying N_A, N_B and P of the system, but more often that's not enough to obtain a desired morphology. In this case, it is very useful to add a "tuner" that has favorable enthalpic interactions with A or B block, which leads to more sophisticated phase behavior of the system and a larger variety of structures to choose from.

In an A-*b*-B/H blend where H and A have favorable enthalpic interactions, while H and B are incompatible, A and B are also incompatible, i.e., $\chi_{H\text{-}A} < 0$ and $\chi_{H\text{-}B} > 0$, $\chi_{A\text{-}B} > 0$, the existence of $\chi_{H\text{-}A}$ exerts significant impact on the phase behavior of the system. For example, in a system where both macrophase separation, between the homopolymer and the dibock copolymer, and microphase separation, between B species and the compatible A/H species, can occur, the relative strength of $\chi_{A\text{-}B}$, $\chi_{H\text{-}B}$ and $\chi_{H\text{-}A}$ is the key factor to determine the phase boundaries of the macro/microphase transition. The more negative $\chi_{H\text{-}A}$ is, the less macrophase separation is expected. In the microphase separation regime, enthalpic interactions can be utilized to tune the shape and size of the self-assembled structures, the domain spacings of ordered microphases, as well as shifting the location of the order-disorder transition.

The A-*b*-B/H systems have been investigated by a number of groups in the past two decades[1, 12-31]. Tucker and Paul studied the mixing between poly(2,6-dimethyl-1,4-phenylene oxide) (PPO) and styrene based copolymers[12]. They constructed a simple scaling model to show the effects of favorable enthalpy of mixing between PS block and PPO homopolymer on the maximum solubility of the homopolymer in the microphase

separated copolymer. The same system was re-examined two decades later by Brinke and coworkers[27] where they calculated the concentration profile of the homopolymer in the lamella-assembled diblock copolymer. Akiyama and Jamieson[14] showed the effects of specific interactions between homopolymer poly(styrene-co-acrylonitrile) (SAN) and poly(methyl methacrylate) (PMMA), on the structure of micelles formed in blends of SAN and poly(styrene-*b*-methyl methacrylate) (PS-*b*-PMMA) by systematically changing the acrylonitrile content in SAN. SAN/PS-b-PMMA system was also studied by Lowenhaupt et al.[15] where the phase behavior showed both micro- and macrophase separation. They used random phase approximation calculations (RPA) to predict phase boundaries and compared that to their experimental results. Hashimoto and coworkers[19] investigated the blends of poly(vinyl methyl ether) (PVME) and poly(styrene-*b*-isoprene) (SI) by small angle X-ray scattering. PVME and polystyrene (PS) are known to show LCST behavior. Similar phase behavior was studied by Balsara and coworkers[23] using poly(ethylene-*b*-propylene) (PE-*b*-PP)/polyisobutylene (PIB) blends. Self-consistent theoretical simulations were used to calculate the cylindrical-to-lamellar transitions of several systems including poly(oxyethylene-oxypropylene-oxyethylene) copolymers (PEO-PPO-PEO)/poly(acrylic acid) (PAA) and polystyrene-*b*-poly(ethylene oxide) (PS-*b*-PEO)/PAA blends[31, 32].

In a previous study[33], we examined micelle formation in thin film PS/polystyrene-*b*-poly(2-vinylpyridine) (PS-*b*-P2VP) blends. We studied the effects of host molecular weight on the morphology of the system, the wet-brush to dry-brush transition and the organization of micelles. Herein, we introduce enthalpic interactions into the system by adding tetramethyl bisphenol-A polycarbonate (TMPC) as a special "tuner". We are

particularly interested how the specific interactions between TMPC and PS can affect the structure and organization of the micelles, as well as host-copolymer interactions. We begin by examining micelle formation and organization in ternary blends of PS/TMPC/PS-*b*-P2VP by systematically changing the concentration of TMPC. Following that thickness dependence of micelle formation of the ternary blends is discussed. For a geometrically confined thin film blend, a good portion of the PS-*b*-P2VP chains adsorb onto the substrate, contributing to minimizing the free energy of the system. Therefore the role of enthalpy on how the diblock copolymer chains partition in micelle formation and surface adsorption is also investigated.

5.2 Experimental

The homopolymers and diblock copolymer used in this work are listed in Table 1. Stock solutions of each homopolymer and the diblock copolymer were prepared in toluene. The solutions were subsequently mixed so that the copolymer/homopolymer composition is 20/80. The homopolymer hosts we used were neat PS, a blend of PS and TMPC of different ratios, and a blend of PS/PS with different molecular weights. The mixed solutions were spincoated onto glass slides and the films were then floated from deionized water and picked up onto silicon nitride TEM substrates (SPI supplies). Film thickness was measured on a variable angle spectroscopic ellipsometer (J.A.Woollam Co., Inc.), by spincoating the same solution onto silicon nitride substrates (WaferNet Inc.). The films were dried in vacuum at 65 °C for 24 hours and then annealed in vacuum at 160 °C for 24 hours.

Micelle formation was examined by scanning transmission electron microscopy (STEM), a JEOL 2010F instrument with a high angle annular dark field detector operated at 200kV. Samples were stained in iodine vapor for 5 minutes. Iodine stains the P2VP component of the blends. The size of the micellar cores and the number density of the micelles were calculated in ImageJ software, by analyzing at least 300 micelles from three different areas of the films.

5.3 Results and Discussion

In a thin film diblock copolymer/homopolymer A-*b*-B/A blend, the diblock copolymer tends to self-assemble into micelles, composed of inner core of B component and an outer corona of A component. If B component has favorable interactions with one or both interfaces, the diblock copolymer chains will adsorb onto the surface to form brush layers. Both processes decrease the free energy of the system. Before we discuss micelle formation and surface adsorption in our system, it is important to note that not all the copolymer chains will self-assemble or adsorb onto the surface; there is always a certain amount of free copolymer chains in the blend to maintain the translational entropy of the system, referred to as the critical micelle concentration (cmc). Cmc is proportional to $\sim \exp(-\chi_{A\text{-}B}N_B)$[2, 3]. For PS/TMPC/PS-*b*-P2VP blends, the bulk cmc is very small, almost negligible. The structure of micelles formed in an A-*b*-B/A system is determined by a balance of the following factors: the interfacial tension between A and B species, which favors large micelles, to minimize total contact area between A and B species; note that by large we mean the total number of copolymer chains in a micelle is large; the translational entropy of the homopolymer chains when they penetrate into the corona,

which favors small micelles; and the conformational entropy of the homopolymer and the copolymer: as the homopolymer chains penetrate into the corona, both the homopolymer chains and the A block in the corona will stretch, hence losing conformational entropy.

We begin by examining micelle formation of PS-*b*-P2VP in PS_{15400}, where P (=15400) >> N_A (=489). In this case, the host homopolymer is very long, therefore the host chains are excluded from the vicinity of the micellar cores and reside only in the outer region of the corona, with a penetration depth $\lambda \sim N_A/P$[34]. This is the dry-brush condition. Under this condition, micelles are the largest; they also exhibit long-range attractions, as we can see from Fig. 1a where the micelles formed aggregates. As we gradually added TMPC into the matrix, while keeping the copolymer volume fraction fixed at 20%, micelles became smaller, as shown in Fig. 1b-1d and Fig. 3a, solid squares. In PS_{15400}, the diameter of the micelle cores, D_{core} = 42nm, in excellent agreement with what we obtained from a different microscope in an earlier study; in 25% TMPC/PS_{15400}, D_{core} quickly decreased to 36nm; and in 75% TMPC/PS_{15400}, D_{core} further decreased to 27 nm. The reasons why the diameter of the micelle cores decreases with increasing TMPC/PS_{15400} ratio could be two-fold. Firstly, the degree of polymerization of TMPC is P_{TMPC} = 122 < N_A. Since the TMPC chains are short, shorter than the PS block in the corona, it means that entropically TMPC and the corona make a wet-brush case; TMPC chains readily penetrate into the corona, stretching the corona, resulting in smaller micelles than the dry-brush condition. Secondly, from an enthalpic point of view, TMPC and PS are compatible, which could further promote mixing between TMPC chains and the corona, also contributing to smaller micelles.

In order to separate the entropic contributions to micelle formation from the enthalpic ones, we made a set of PS_{125}/PS_{15400}/PS-*b*-P2VP ternary blends in which the degree of polymerization of PS_{125} is essentially the same as that of the TMPC chains, but there is no enthalpic interactions between PS_{125} and the corona. The results are shown in Fig. 1e-1g and Fig. 3a, solid circles. We see similar trends in the micelles formed in TMPC/PS_{15400}/PS-*b*-P2VP blends, a decrease in D_{core} with increasing PS_{125}/PS_{15400} ratio, due to the entropic wet-brush situation between PS_{125} and the corona. However, the decrease is not as significant as adding TMPC. With the same amount of TMPC and PS_{125} in the matrix, micelles are smaller in TMPC/PS_{15400}/PS-*b*-P2VP. We note here that the entropic contributions from TMPC and PS_{125} are not exactly the same. As a matter of fact, with the same degree of polymerization, TMPC does not penetrate into the corona as easily as PS_{125}, because the monomer size of TMPC is 1.83 nm, almost three times as large as that of PS, 0.55 nm. This means that if there were only entropic effects contributing to the micelle formation in the system, the micelles would appear to be larger in TMPC/PS_{15400}/PS-*b*-P2VP than in PS_{125}/PS_{15400}/PS-*b*-P2VP blends. What we observed is the opposite, which proves that enthalpy indeed plays an important role. TMPC further penetrates into the corona, due to the favorable enthalpy of mixing, stretching the corona even more, causing the micelles to be smaller. We will come back to the detail of the effects of enthalpy on the micelle formation later.

Another fascinating observation we get from Fig.1 is how adding an enthalpic or an entropic "tuner" can change the organization of micelles. From Fig. 1a we see that micelles organized into hexagonal closepacked aggregates, due to their long-range attractions under the dry-brush condition. When we replaced 25% of PS_{15400} with TMPC

or PS_{125}, as shown in Fig. 1b and 1e, micelles still formed aggregates, but with larger spacings. This is technologically important because it suggests that we can precisely control the domain spacing of an ordered micelle array by adding a "tuner" without changing the major components of the system. When the matrix is 50% PS_{125}/PS_{15400}, micelles still attract to each other, compared to in 50% TMPC/PS_{15400}, where the micelles only show partial organization. When the matrix is 75% PS_{125}/PS_{15400}, micelles are partially organized, while in 75% TMPC/PS_{15400}, the micelles no longer attract to each other and distributed homogeneously in the matrix. This is another aspect of the enthalpic contributions to the system.

The effects of enthalpic interactions on micelle formation and organization are now explained. First let's look at the PS_{125}/PS_{15400}/PS-*b*-P2VP ternary blends where no enthalpy is involved. Before adding PS_{125}, micelles aggregated to minimize the conformational entropy loss of the long host chains around the dry micelles. When PS_{125} chains are added into PS_{15400}/PS-*b*-P2VP binary blends, if they stayed in the matrix without interacting with the corona, the free energy of the system would stay the same, as PS_{125}/PS_{15400} is an athermal mixture; if PS_{125} penetrated into the corona of the micelles, the system would gain translational entropy, hence the free energy would decrease. Therefore, PS_{125} chains penetrate into the corona instead of staying in the matrix. Alternatively, we can say that the corona swelled and solvated the PS_{125} chains. This explains why the intermicelle spacing increased with increasing PS_{125}/PS_{15400} ratio. On the other hand, PS_{15400} chains still lose conformational entropy around the swollen micelles because it's still a dry brush for PS_{15400}, hence the swollen micelles aggregated

to minimize the free energy of the system. This explains why even at 75% PS_{125}/PS_{15400}, micelles still showed some attraction and organization.

When TMPC is added into the system, the interactions are more complicated. The system gains enthalpy and entropy of mixing if TMPC chains penetrate into the corona; on the other hand, when TMPC is mixed with the host, the system also gains enthalpy and entropy of mixing. Indeed, our calculations show that a portion of TMPC chains mixed with the corona, and a portion of them mixed with the matrix. The portion that mixes with the corona decreases with decreasing molecular weight of PS in the matrix. Also, with the presence of TMPC, PS homopolymer chains do not penetrate into the corona unless it is very short. In TMPC/PS_{15400}/PS-*b*-P2VP ternary blends, the micelles are swollen by the portion of TMPC chains that mixed with the corona. For PS_{15400} chains, they suffer conformational entropy loss when they are in the vicinity of the micelles, but gain enthalpy when in contact with TMPC chains around the corona. Therefore as the concentration of TMPC increased, it prevented the micelles from aggregating by interacting favorably with PS_{15400}.

Now we decrease the length of the PS homopolymer to P = 1460, see Fig. 2 and Fig 3a, open squares and circles. From our previous study we know that this is a wet brush condition, where PS_{1460} chains intermix with the corona and the micelles don't aggregate, as shown in Fig. 2a. As we add TMPC or PS_{125} into the blend, D_{core} decreases with increasing TMPC/PS_{1460} or PS_{125}/PS_{1460} ratio. For the ternary blends, TMPC and PS_{125} chains gain more translational entropy than PS_{1460} when they mixed with the corona, and they stretched the corona more than PS_{1460}, therefore D_{core} decreases with increasing TMPC or PS_{125} concentration. We can see that the micelles are smaller in

TMPC/PS_{1460}/PS-*b*-P2VP than in PS_{125}/PS_{1460}/PS-*b*-P2VP, which means that enthalpy is important in this set of samples, too. But the size difference is not as significant as in the PS_{15400} ternary blends, consistent with our calculations, as less TMPC chains are mixed with the corona and more are mixed with the PS_{1460} homopolymer now.

From Fig.1 and Fig. 2 we also notice that the number density of micelles, $n_{micelle}$, increases with the TMPC and PS_{125} concentration. $n_{micelle}$ in different matrices is plotted in Fig. 3b. We can see that $n_{micelle}(PS_{125}/PS_{15400}) < n_{micelle}(TMPC/PS_{15400}) < n_{micelle}(PS_{125}/PS_{1460}) < n_{micelle}(TMPC/PS_{1460})$. The volume fraction of the diblock copolymer chains forming micelles, $v_{micelle}$, calculated from D_{core} and $n_{micelle}$, using N_B/N_A = 277/489, density of P2VP =1.18 g/cm^3, density of PS = 1.045 g/cm^3, is shown in Fig. 4a. Note that the thickness of all the samples used in Fig.1-4 was controlled to be 80 ± 3 nm. We can see that $v_{micelle}$ in PS_{15400} is smaller than in PS_{1460}, which is consistent with our findings in the previous work. $v_{micelle}$ increases with increasing TMPC and PS_{1460} concentration. In all matrices, $v_{micelle}$ is well below the total volume fraction of the copolymer chains in the system, 20%. As we mentioned earlier, the bulk critical micelle concentration in our system is negligible compared to micelle formation and surface adsorption. Therefore we can safely assume that the rest of the copolymer chains all adsorbed onto the substrate to form the brush layer, due to the preferential affinity between the P2VP component and the silicon nitride substrate. By accurately measuring the thickness of each sample, and knowing the volume fraction of the micelles, we calculated the brush layer thickness of the samples, h_{brush}, shown in Fig. 4b.

First let's compare h_{brush} in TMPC/PS_{15400} and PS_{125}/PS_{15400} matrices, the solid squares and solid circles in Fig. 4b. We can see that h_{brush} decreases with increasing

TMPC and PS_{125} concentration. In 25% TMPC/PS_{15400} and 25% PS_{125}/PS_{15400}, h_{brush} only shows a slight decrease from that in neat PS_{15400}, from 15 nm to 14 nm; h_{brush} in 25% TMPC/PS_{15400} is slightly smaller than in 25% PS_{125}/PS_{15400}, and as the ratio increased to above 50%, h_{brush} becomes a lot smaller in TMPC/PS_{15400} than in PS_{125}/PS_{15400} matrix. Similar to the host homopolymer-micelle interactions, PS_{15400} has only finite penetration depth into the brush layer and is a dry-brush; therefore h_{brush} in neat PS_{15400} is the largest in all matrices. TMPC and PS_{125} readily intermix with the PS blocks in the brush; hence we see a decrease in h_{brush} with increasing TMPC and PS_{125} concentration. However, the situation is slightly different from the interactions between the host chains and the micellar corona. For the micelles, the effective **"** grafting density**"** (the total number of PS blocks in one micelle/surface area of the core), $\Sigma_{micelle}$, is smaller than that of the brush layer (number of copolymer chains per unit area), Σ_{brush}, due to the curvature of the micelles. At low concentrations, TMPC and PS_{125} chains would mix with the corona of the micelles first, because it costs less elastic energy than penetrating into the brush layer. As the concentration of TMPC and PS_{125} increases, they start to mix with the brush layer, too. The favorable enthalpy of mixing between the TMPC and the PS block in the brush leads to a further decrease in h_{brush} in TMPC/PS_{15400} than in PS_{125}/PS_{15400}. On the other hand, we see that h_{brush} is the same in TMPC/PS_{1460} and PS_{125}/PS_{1460}, with the same TMPC and PS_{125} concentration. This is because there is increased amount of TMPC mixing with PS_{1460} in the matrix that aren't in the corona of the micelles or the brush layer.

In the foregoing we discussed the role of enthalpy in the formation and organization of micelles in TMPC/PS/PS-*b*-P2VP ternary blends by changing the matrix

homopolymer composition. For the rest of this work, we examine thickness dependence of micelle formation of the ternary blends. Fig. 5 shows the thickness dependence of micelle formation in two matrices: PS_{1460} and 50% TMPC/PS_{1460}. The volume fraction of the diblock copolymer is kept to be 20% in all samples. We can clearly see a thickness dependence of micelle formation from Fig. 5: $n_{micelle}$ decreases with decreasing film thickness, in both matrices. It is worth mentioning that, within experimental error, the size of the micelles don't appear to change with film thickness. In Fig. 6 we show the thickness dependence of micelle formation and surface adsorption in the matrices of PS_{1460}, TMPC/PS_{1460} and PS_{125}/PS_{1460}. We can see that $n_{micelle}$ and $v_{micelle}$ decrease with decreasing film thickness in all matrices (Fig. 6a and 6b), and there exists a threshold thickness, around 50 nm, below which no micelles can form because of geometrical confinement. Below the threshold thickness, only the surface adsorption process of the diblock copolymer chains occurs. Fig. 6c shows the brush layer thickness in these samples. Above the threshold thickness where both micelle formation and surface adsorption are present in the system the, h_{brush} also exhibit thickness dependence: it increases with increasing film thickness. It suggests that equilibrium of the system, between the copolymer chains in the micelles, those adsorbed onto the surface to form the brush layer and the free copolymer chains in the system is thickness dependent.

5.4 Conclusions

We showed the formation and organization of micelles in thin film ternary blends of TMPC/PS_P/PS-*b*-P2VP and PS_{125}/PS_P/PS-*b*-P2VP, where P = 15400 or 1460. With the same film thickness, the diameter of the micelle cores, D_{core}, decreased with increasing

TMPC and PS_{125} concentration, and the decrease is more significant in TMPC/PS_P matrices, due to the favorable enthalpic interactions between TMPC and the corona. When P = 15400, PS_{125} chains are solvated in the corona of the micelles, swelling the corona, while the organization of the micelles are not interrupted when the ratio of PS_{125}/PS_{15400} is below 75%. Part of the TMPC chains were solvated in the corona of the micelles, the rest stay in the matrix to minimize the free energy of the system. Micelle-micelle attractions are weakened by the presence of TMPC chains. When P = 1460, more TMPC chains remain in the matrix. PS-*b*-P2VP chains also adsorb onto the substrate to form a brush layer. At low TMPC or PS_{125} concentrations, they mix with the corona first instead of the brush layer due to less elastic energy cost resulted from the curvature of the micelles. Finally, there is a threshold thickness, approximately 50 nm, below which micelles cannot form due to geometrical confinement. Above the threshold thickness both micelle formation and surface adsorption show film thickness dependence.

5.5 References

1. Kinning, D. J.; Winey, K. I.; Thomas, E. L. *Macromolecules* **1988,** 21, (12), 3502-3506.
2. Leibler, L.; Orland, H.; Wheeler, J. C. *Journal of Chemical Physics* **1983,** 79, (7), 3550-3557.
3. Whitmore, M. D.; Noolandi, J. *Macromolecules* **1985,** 18, (4), 657-665.
4. Shull, K. R.; Kramer, E. J.; Hadziioannou, G.; Tang, W. *Macromolecules* **1990,** 23, (22), 4780-4787.
5. Shull, K. R.; Winey, K. I.; Thomas, E. L.; Kramer, E. J. *Macromolecules* **1991,** 24, (10), 2748-2751.
6. Green, P. F.; Russell, T. P. *Macromolecules* **1991,** 24, (10), 2931-2935.
7. Dai, K. H.; Kramer, E. J.; Shull, K. R. *Macromolecules* **1992,** 25, (1), 220-225.
8. Green, P. F.; Russell, T. P. *Macromolecules* **1992,** 25, (2), 783-787.
9. Semenov, A. N. *Macromolecules* **1992,** 25, (19), 4967-4977.
10. Esselink, F. J.; Semenov, A. N.; Tenbrinke, G.; Hadziioannou, G.; Oostergetel, G. T. *Physical Review B* **1993,** 48, (18), 13451-13458.

11. Oh, H.; Green, P. F. *Macromolecules* **2008,** 41, (7), 2561-2566.
12. Tucker, P. S.; Paul, D. R. *Macromolecules* **1988,** 21, (9), 2801-2807.
13. Löwenhaupt, B.; Hellmann, G. P. *Colloid & Polymer Science* **1990,** 268, (10), 885-894.
14. Akiyama, M.; Jamieson, A. M. *Polymer* **1992,** 33, (17), 3582-3592.
15. Loewenhaupt, B.; Steurer, A.; Hellmann, G. P.; Gallot, Y. *Macromolecules* **1994,** 27, (4), 908-916.
16. Lu, M.; Keskkula, H.; Paul, D. R. *Polymer* **1996,** 37, (1), 125-135.
17. Prahsarn, C.; Jamieson, A. M. *Polymer* **1997,** 38, (6), 1273-1283.
18. Zhao, J. Q.; Pearce, E. M.; Kwei, T. K. *Macromolecules* **1997,** 30, (23), 7119-7126.
19. Iizuka, N.; Bodycomb, J.; Hasegawa, H.; Hashimoto, T. *Macromolecules* **1998,** 31, (21), 7256-7266.
20. Han, Y.-K.; Pearce, E. M.; Kwei, T. K. *Macromolecules* **2000,** 33, (4), 1321-1329.
21. Ahn, J.-H.; Sohn, B.-H.; Zin, W.-C.; Noh, S.-T. *Macromolecules* **2001,** 34, (13), 4459-4465.
22. Ahn, J.-H.; Sohn, B.-H.; Zin, W.-C. *Polymer* **2002,** 43, (11), 3345-3351.
23. Lee, J. H.; Balsara, N. P.; Chakraborty, A. K.; Krishnamoorti, R.; Hammouda, B. *Macromolecules* **2002,** 35, (20), 7748-7757.
24. Kim, S. H.; Misner, M. J.; Russell, T. P. *Advanced Materials* **2004,** 16, (23-24), 2119-2123.
25. van Zoelen, W.; Alberda van Ekenstein, G.; Ikkala, O.; ten Brinke, G. *Macromolecules* **2006,** 39, (19), 6574-6579.
26. de Wit, J.; Alberda van Ekenstein, G.; ten Brinke, G. *Polymer* **2007,** 48, (6), 1606-1611.
27. Klymko, T.; Subbotin, A.; ten Brinke, G. *Macromolecules* **2007,** 40, (8), 2863-2871.
28. Tirumala, V. R.; Romang, A.; Agarwal, S.; Lin, E. K.; Watkins, J. J. *Advanced Materials* **2008,** 20, (9), 1603-+.
29. Bosse, A. W.; Tirumala, V. R.; Lin, E. K. *Journal of Polymer Science Part B: Polymer Physics* **2009,** 47, (21), 2083-2090.
30. Chen, S.-C.; Kuo, S.-W.; Jeng, U. S.; Su, C.-J.; Chang, F.-C. *Macromolecules* **2009,** 43, (2), 1083-1092.
31. LefeÃÄvre, N.; Daoulas, K. C.; MuÃàller, M.; Gohy, J.-F. o.; Fustin, C.-A. *Macromolecules* **2010,** 43, (18), 7734-7743.
32. Tirumala, V. R.; Daga, V.; Bosse, A. W.; Romang, A.; Ilavsky, J.; Lin, E. K.; Watkins, J. J. *Macromolecules* **2008,** 41, (21), 7978-7985.
33. Chen, X. C.; Yang, H.; Green, P. F. *Macromolecules* **2011**, null-null.
34. Borukhov, I.; Leibler, L. *Macromolecules* **2002,** 35, (13), 5171-5182.

	Mw (g/mol)	PDI	P	N_A/N_B	Source
PS_{15400}	1,600,000	1.16	15400		Pressure Chemical Co.
PS_{1460}	152,000	1.06	1460		Pressure Chemical Co.
PS_{125}	13,500	1.06	125		Pressure Chemical Co.
TMPC	37,900	2.75	122		Bayer
PS-*b*-P2VP	50,900/29,100	1.04		489/277	Polymer Source, Inc.

Table 5-1 Characteristics of homopolymers and the diblock copolymer used in this work

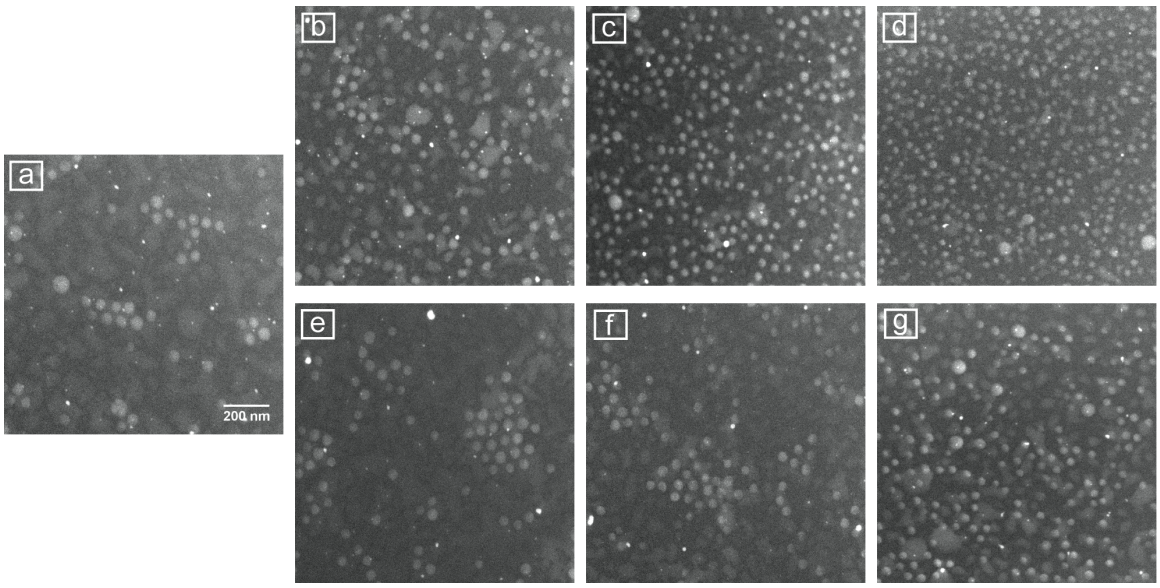

Figure 5.1 Scanning transmission electron microscopy (STEM) of 20% PS-*b*-P2VP in a matrix with the following composition: (a), PS_{15400}, (b), 25% TMPC/PS_{15400}, (c), 50% TMPC/PS_{15400}, (d), 75% TMPC/PS_{15400}, (e), 25% PS_{125}/PS_{15400}, (f) 50% PS_{125}/PS_{15400} and (g) 75% PS_{125}/PS_{15400}. Films were 80 ± 3 nm.

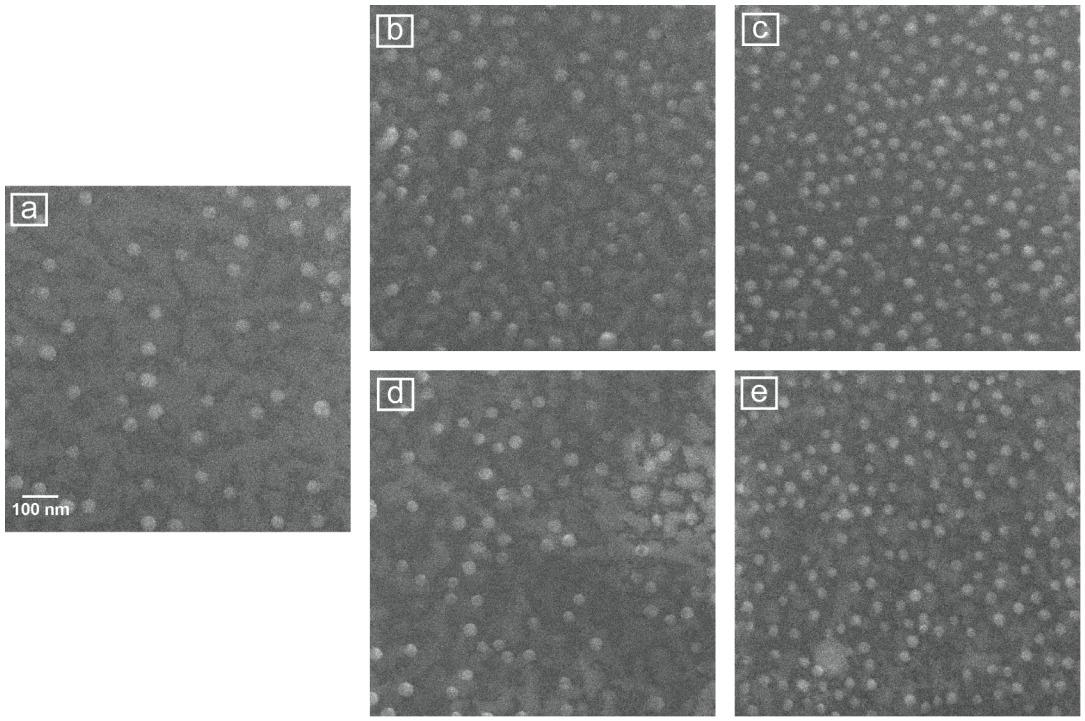

Figure 5.2 Scanning transmission electron microscopy (STEM) of 20% PS-*b*-P2VP in a matrix with the following composition: (a), PS_{1460}, (b), 25% TMPC/PS_{1460}, (c), 50% TMPC/PS_{1460}, (d), 25% PS_{125}/PS_{1460}, and (e), 50% PS_{125}/PS_{1460}. Films were 80 ± 3 nm.

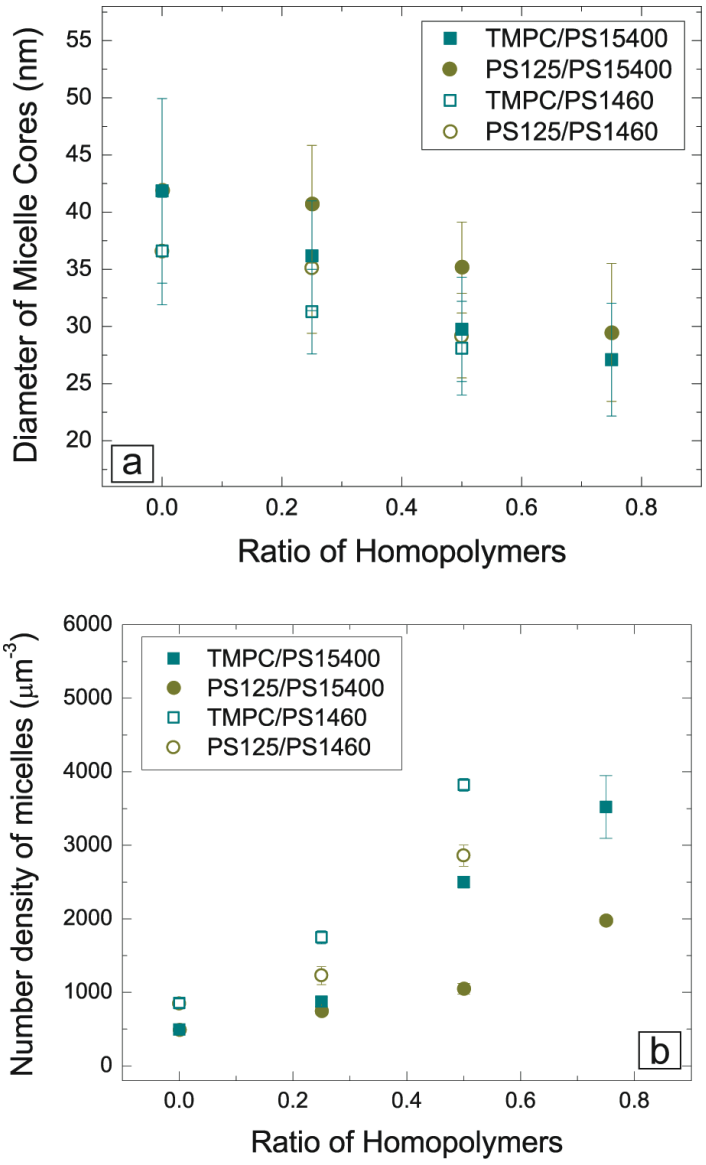

Figure 5.3 Diameters of micelle cores, (a), and number density of micelles, (b), as a function of host homopolymer composition are shown here. Solid squares, solid circles, open squares and open circles represent TMPC/PS_{15400}, PS_{125}/PS_{15400}, TMPC/PS_{1460}, and PS_{125}/PS_{1460}, respectively. The volume fraction of PS-*b*-P2VP was 20%. Films were 80 ± 3 nm.

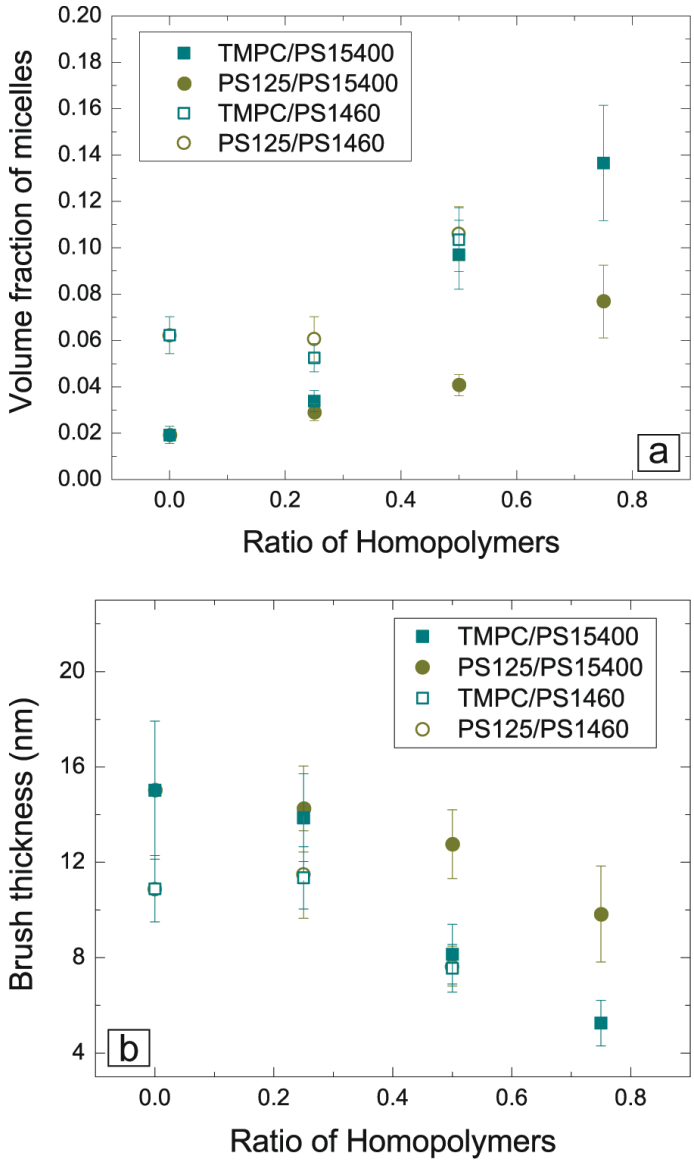

Figure 5.4 Volume fraction of the micelles, (a), and thickness of the brush layer, (b), as a function of host homopolymer composition are shown here. Solid squares, solid circles, open squares and open circles represent TMPC/PS_{15400}, PS_{125}/PS_{15400}, TMPC/PS_{1460}, and PS_{125}/PS_{1460}, respectively. The volume fraction of PS-*b*-P2VP was 20%. Films were 80 ± 3 nm.

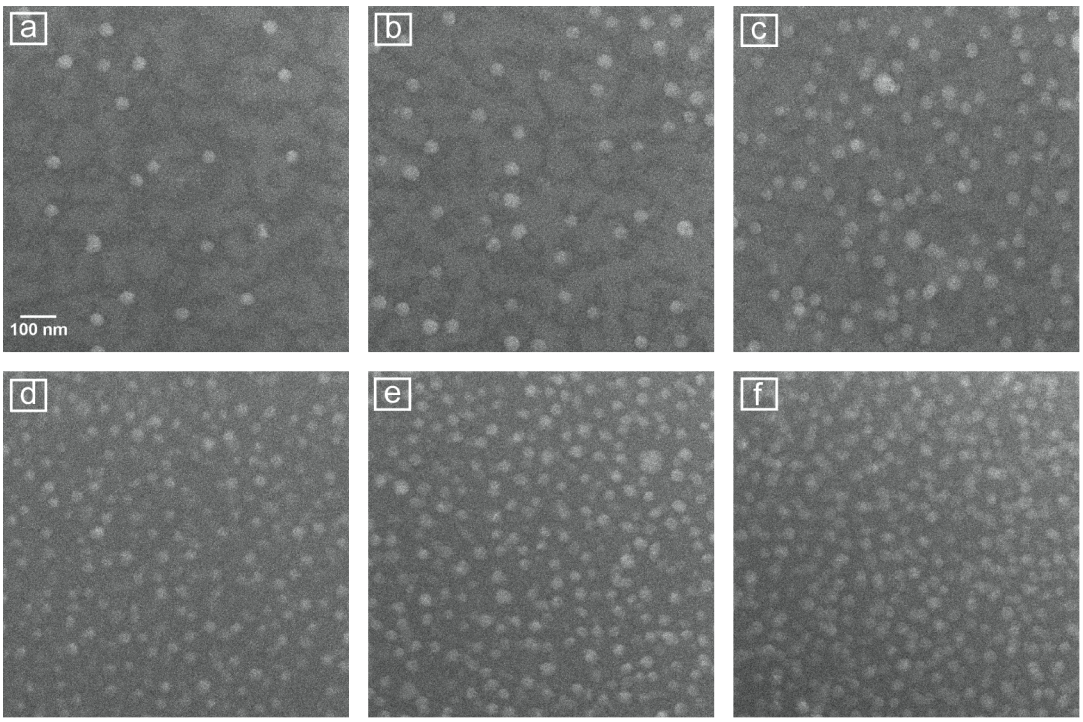

Figure 5.5 Scanning transmission electron microscopy (STEM) of 20% PS-*b*-P2VP in a matrix of PS_{1460} (a, b and c), and 50% TMPC/PS_{1460} (d, e and f). Film thicknesses were 60 nm (a and d), 80 nm (b and e), and 110 nm (c and f).

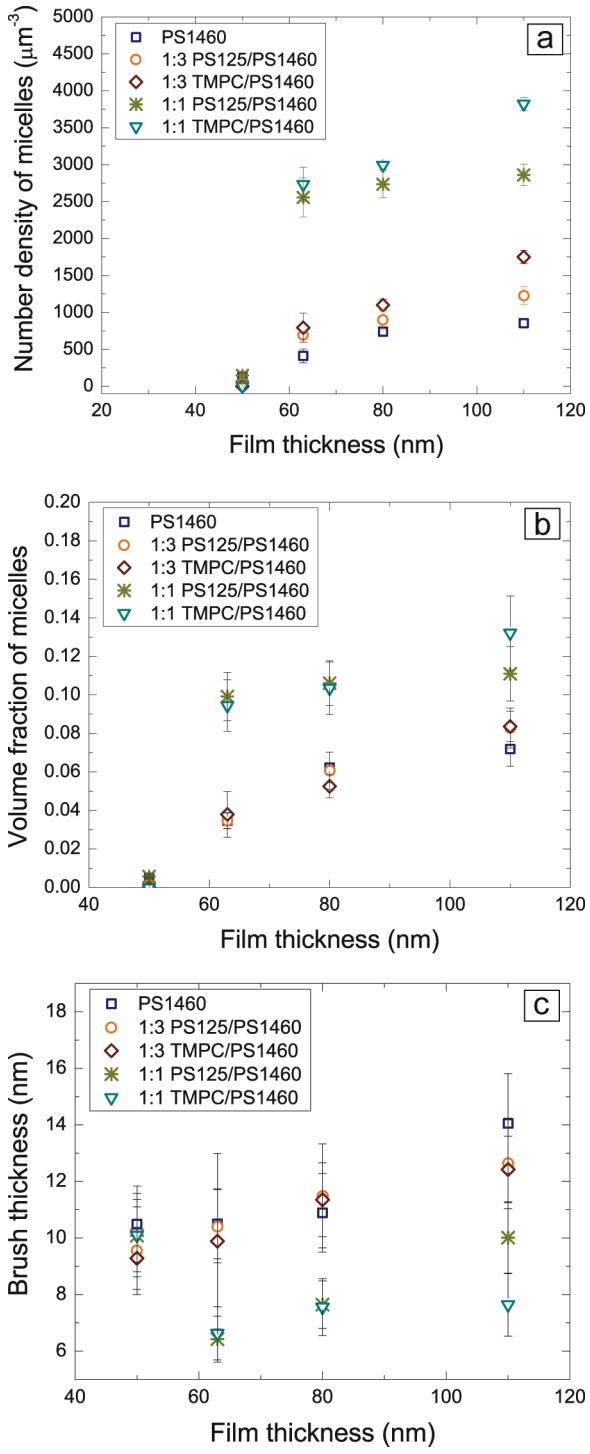

Figure 5.6 Number density of the micelles, (a), volume fraction of the micelles, (b), and thickness of the brush layer, (c), and as a function of film thickness are shown here. The volume fraction of PS-*b*-P2VP was 20%. The matrix is the following: squares, PS_{1460}, circles, 25% PS_{125}/PS_{1460}, diamonds, 25% TMPC/PS_{1460}, stars, 50% PS_{125}/PS_{1460}, and triangles, 50% TMPC/PS_{1460}

Chapter 6

Conclusions and Ongoing/Future Directions

6.1 Conclusions

Our research is aimed at gaining control of the structure and nano-scale morphology of thin film PNCs and understanding the structure-property relationships. Our goal is to design PNCs with tailored morphologies and desired properties for specific applications. In this work, we first explored the design rules of thin film PNCs by investigating the structure of polymer-tethered metal nanoparticles/polymer composites (chapter 1); then we designed a series of PNCs with tailored fluorescence properties using MEH-PPV (chapter 2). Following that we compared different tethered structures (nanoparticles vs diblock copolymer) in thin film PNCs. The roles of entropy and enthalpy in the micelle formation and surface adsorption of diblock copolymers in thin film homopolymer melts are examined. Below is a summary of the key findings of our work.

In chapter 2, the relative role of favorable enthalpic interactions and entropic interactions on the miscibility in thin film polymer A-brush coated nanoparticles within a chemically dissimilar homopolymer B host was investigated. Our results reveal that entropic effects, associated with the brush/host chain interactions, nanoparticle diameter, D, and asymmetries in monomer sizes of the host chains and grafted chains, can play a more important role than the favorable A/B enthalpic interactions toward determining the

phase miscibility of the system. A phase diagram is constructed to show the phase separated and dispersed regimes as a function of D, N, the degree of polymerization of the grafted chains and P, the degree of polymerization of the host chains, at a constant grafting density. These results have important implications on the design of brush coated nanoparticle/homopolymer mixtures for various applications.

In chapter 3, chain grafted Au nanoparticles were synthesized and incorporated into a fluorescent polymer, poly[2-methoxy-5-(2-ethylhexyloxy)-1,4-phenylenevinylene] (MEH-PPV) host. We showed that control of the Au nanoparticle distribution within MEH-PPV is achieved by manipulating the enthalpic and entropic interactions between the grafted brush layers and the host chains. Further, we showed that the fluorescence of these Au/MEH-PPV nanocomposite thin films may be "tailored" by as much as an order of magnitude, through changes in the nanoparticle distribution, brush length and nanoparticle size. The ideas presented herein represent reliable strategies for materials design for devices.

In chapter 4 we showed that polystyrene-*b*-poly(2-vinylpyridine) (PS-b-P2VP) diblock copolymer chains aggregate to form micelles, composed of an inner P2VP core and an outer PS corona, as well as adsorb onto the substrate, forming brush layers, in supported thin film PS/PS-b-P2VP mixtures. The degrees of polymerization of the chains that comprised the corona and core were N_{PS} and N_{P2VP}, respectively. The diameter of the micelle cores, D_{core}, increased with increasing degree of polymerization, P, of the PS host and became constant for large values of P. A decrease in the number density of micelles, $n_{micelle}$, accompanied the increase in D_{core}; $n_{micelle}$ reached a plateau in the same range of values of P where D_{core} became constant. The organization of the micelles

suggests the existence of attractive micelle-micelle interactions in the large P regime. Moreover, in this regime, the micelles preferentially migrated to the free surface. The morphology of this system is compared to thin film PS melts containing brush-coated nanoparticles. One fundamental difference between the two systems is that the micellar system has the ability to adjust the number of chains per micelle in order to mediate the host chain/brush (micelle corona) interactions. Consequently the condition under which the host chains are excluded from inter mixing with the corona, the wet-brush to dry-brush transition, occurs when P was considerably larger than N_{PS}, instead of $P/N_{PS}=1$ for chains grafted onto a flat surface.

In chapter 5 we examined the formation and organization of micelles in thin film ternary blends of TMPC/PS_P/PS-*b*-P2VP and PS_{125}/PS_P/PS-*b*-P2VP, where P = 15400 or 1460. With the same film thickness, the diameter of the micelle cores, D_{core}, decreased with increasing TMPC and PS_{125} concentration, and the decrease is more significant in TMPC/PS_P matrices, due to the favorable enthalpic interactions between TMPC and the corona. When P = 15400, PS_{125} chains are solvated in the corona of the micelles, swelling the corona, while the organization of the micelles are not interrupted when the ratio of PS_{125}/PS_{15400} is below 75%. Part of the TMPC chains were solvated in the corona of the micelles, the rest stay in the matrix to minimize the free energy of the system. Micelle-micelle attractions are weakened by the presence of TMPC chains. When P = 1460, more TMPC chains remain in the matrix. PS-*b*-P2VP chains also adsorb onto the substrate to form a brush layer. At low TMPC or PS_{125} concentrations, they mix with the corona first instead of the brush layer due to less elastic energy cost resulted from the curvature of the micelles. Finally, there is a threshold thickness, approximately 50 nm,

below which micelles cannot form due to geometrical confinement. Above the threshold thickness both micelle formation and surface adsorption show film thickness dependence.

6.2 Ongoing and future directions

There are a number of ongoing and future directions we are working or will be working on, in developing advanced techniques in the application of organic solar cells.

6.2.1 Advanced morphology characterization using energy-filtered TEM (EFTEM)

Bulk heterojunction (BHJ) polymer photovoltaics (PVs), containing a thin film blend of a hole transporting polymer and an electron transporting material, show promise in the search of new energy resources. Control of the morphology of the blend of electron and hole transporting materials is crucial to achieving better power conversion efficiency as it plays an important role in the charge separation and transport processes. Herein we investigate advanced technologies for morphology characterization and local property measurements in organic solar cells.

Energy-filtered transmission electron microscopy (EFTEM) is a powerful technique for chemical analysis. It utilizes electrons of particular kinetic energies to form the image or diffraction pattern, through an image filter. Fig. 6.1 shows an example of the morphology of a typical organic solar cell; we can see that the contrast is greatly enhance in EFTEM compared to the unfiltered image.

6.2.2 Advanced techniques for local electrical properties: photoconductive SPM

Photoconductive SPM is a modified mode of conductive SPM, which is a powerful current sensing technique which simultaneously measures the local topography

and current of a sample. The current measured by conductive SPM usually ranges from hundreds of femtoamps to nearly a microamp. It can be applied to thin dielectric films, ferro-electric films, nanotubes, conductive polymers, etc. For materials systems such as thin film organic solar cells, a focused laser beam can be utilized to shine on the sample from underneath passing the transparent substrate, thus local photocurrents as well as topography information can be generated simultaneously, which give useful information of the internal structure of the thin film solar cells, see Fig. 6.2.

6.2.3 Advanced technique for local dielectric properties: scanning impedance microscopy

We are in the process of setting up the scanning impedance microscopy, where a network analyzer is connected to the SPM. The tip of the SPM serves as the top electrode of the network analyzer to measure local dielectric properties of the sample. The setup of scanning impedance microscopy is shown in Fig. 6.3. It is very useful in the applications of measuring local dynamic properties of thin polymer nanocomposite films as well as charge carrier mobilities of optoelectronic devices.

poly-3(hexylthiophene) (P_3HT)/phenyl-C_{61}-butyric-acid-methyl ester (PCBM) blend

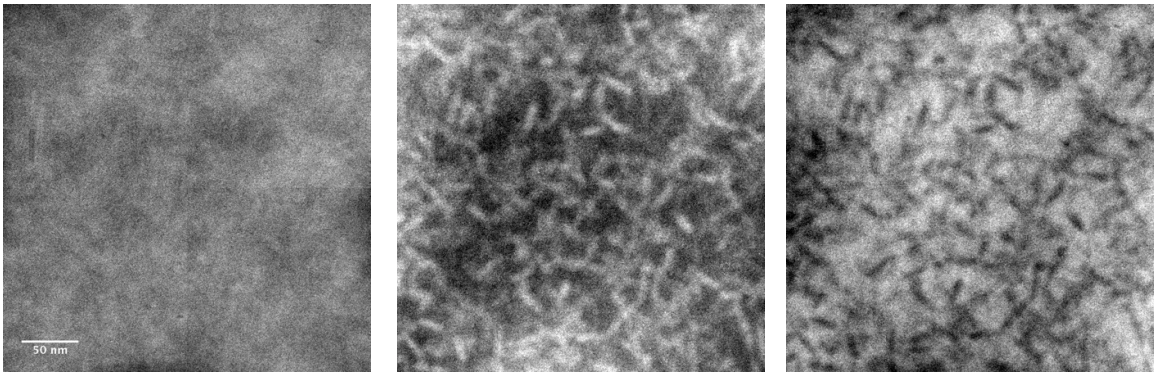

Zero-loss image

energy filtered TEM image
energy loss = 17.5-22.9eV
Bright region: P3HT

energy filtered TEM image
energy loss = 25.9-34.9eV
Bright region: PCBM

Figure 6.1 Zero-loss bright-field image and EFTEM images of P3HT/PCBM blend are shown here.

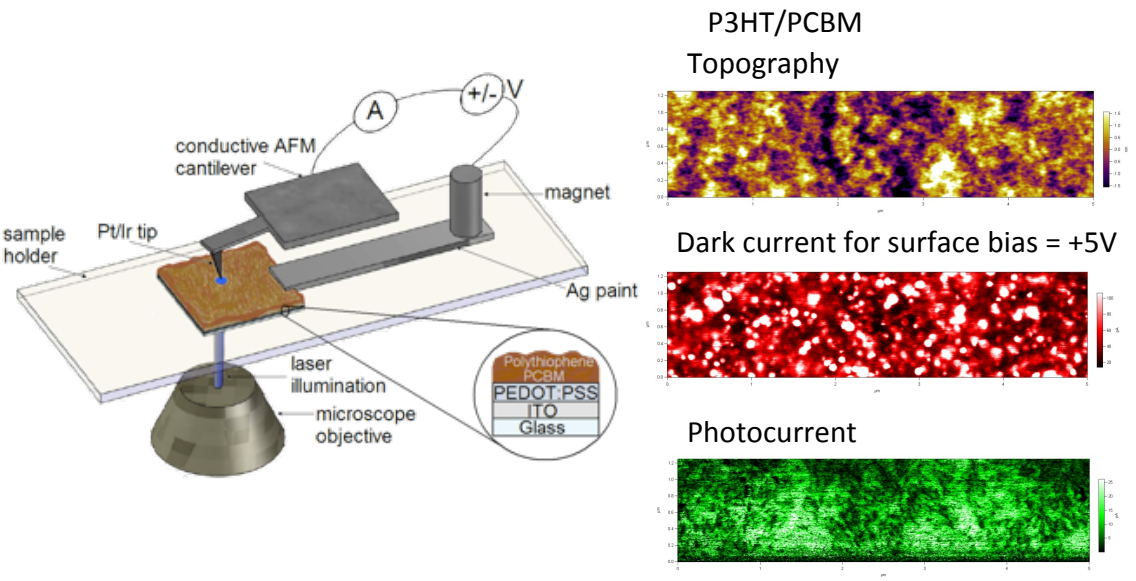

Figure 6.2 Schematic of photoconductive SPM and an example of the photoconductive SPM imaging on P3HT/PCBM solar cells. (Collaboration with Jojo Amonoo and Emmanouil Glynos)

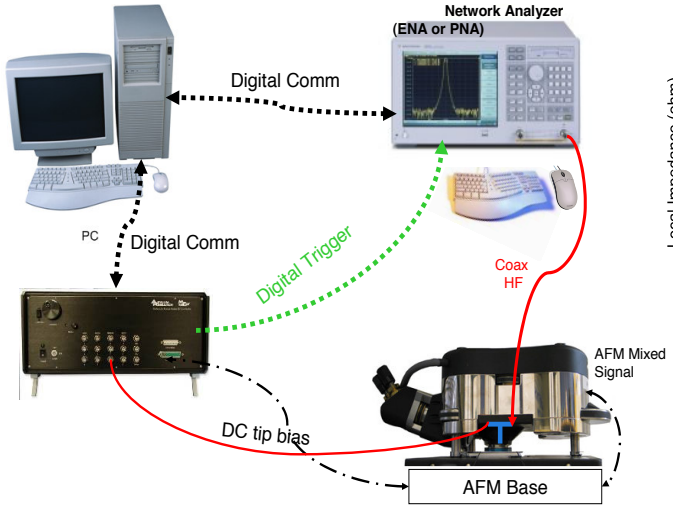

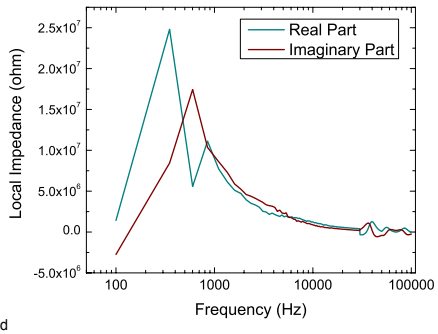

Local impedance of a P3HT thin film

Figure 6.3 Setup of scanning impedance microscopy.

Appendices

A1. Transmission electron microscopy

Transmission electron microscopy (TEM) is a microscopy technique using high-energy electron beam to image an ultra thin specimen, allowing for Angstrom image resolutions. It is the most important technique used throughout this work for morphology characterization of the polymer nanocomposites. In this subsection we introduce the basics of TEM and a special type of TEM, namely the scanning transmission electron microscopy (STEM).

A1.1. Interactions between electrons and the specimen

The maximum resolution, δ, of a light microscope can be specified by

$$\delta = \frac{0.61\lambda}{\mu sin\beta} \tag{A1.1}$$

where λ is the wavelength of light, μ is the refractive index of the viewing medium, and β is the collection semi-angle of the magnifying lens. Since λ of visible light is 400-700 nm, the maximum resolution of light microscope is about 300 nm. Electrons, having both wave and particle properties, can behave like a beam of electromagnetic radiation. The wavelength of electrons is related to their energy, shown by de Broglie's equation:

$$\lambda \approx \frac{h}{\sqrt{2m_0E\left(1+\frac{E}{2m_0c^2}\right)}} \tag{A1.2}$$

where h is Planck's constant, m_0 is the rest mass of an electron and E is the energy of the electron. If we ignore relativistic effects,

$$\lambda \sim \frac{1.22}{E^{1/2}} \tag{A1.3}$$

This means that for 100 keV acceleration voltages, λ of the electrons is about 4 pm! However, the actual resolution of TEM is much larger, in the sub-nanometer range, due to instrument limitations.

As a high-energy beam of electrons transmits through the specimen, electrons may interact with the specimen, as shown in Fig. A1.1. While unscattered electrons, elastically and inelastically scattered electrons can be used to construct diffraction patterns, bright field and dark field images, a wide range of secondary signals are generated from the specimen, which provide chemical information and other details about the specimen. Modern analytical TEMs use these signals for various microanalysis.

A1.2. How images are generated in TEM

A TEM is consisted of three essential components: the illumination system, the objective lens/stage, and the imaging system. The ray diagram of a generic TEM is shown in Fig. A1.2. The illumination system is the parts above the specimen, including the gun and the condenser lenses. The purpose of the illumination system is to take the electrons from the source and transfer them to the specimen. The objective lens/stage system is the heart of the TEM, where incident electron-specimen interactions take place and the images or diffraction patterns are generated. The imaging system contains the

intermediate lenses and the projector lens, used to magnify and focus the images or diffraction patterns to the viewing screen.

There are two basic operations of the TEM imaging system, the diffraction mode and the imaging mode. Electrons that have left the specimen at different points but at the same angle are brought together at the focal plane of the objective lens, i.e., the diffraction pattern is formed on the back focal plane of the objective lens. By adjusting the strength of the intermediate lens, the diffraction pattern can be selected as its object to be projected on the viewing screen. This is the diffraction mode. On the other hand, electrons passing through the specimen are focused by the objective lens to form an image at its image plane. In imaging mode, the image plane serves as the object for the intermediate lens, which produces a magnified image; this image in turn becomes the object of the projector lens, which projects the further-magnified final image on the viewing screen. This is the imaging mode. In imaging mode, electrons that pass through the same point of the specimen are brought together to the same point on the final image.

An image can be generated from either the directly transmitted (unscattered) electrons, or some or all of the scattered electrons. By inserting the objective aperture into the back focal plane of the objective lens, we can choose which electrons to form the images. When unscattered electrons pass through the objective aperture, a bright-field image is formed. Dark areas in the bright-field image arise from specimen regions which scatter electrons widely. If scattered electrons are selected, a dark-field image is produced. In the dark-field image bright areas are from specimen regions which scatter electrons widely. Dark-field images usually have much higher contrast than bright-field images, at the cost of reduced intensity, see Fig. A1.3 for an example.

A1.3. Scanning transmission electron microscopy

Scanning transmission electron microscopy (STEM) is a special type of TEM, which is a prerequisite for many types of microanalysis. In the traditional TEM, the electron beam is adjusted to be parallel, typically several micrometers. Unlike traditional TEM, STEM uses a focused convergent beam, serving as a probe to localize information coming from the specimen. The focused beam scan on the specimen with scan coils, and the signal is detected by an electron detector, amplified and synchronously displayed on a cathode-ray tube (CRT) with the scan coils. The electron detector can be a bright-field detector, a small disk on the column axis which detects only the transmitted beam to generate a bright-field STEM image. By simply shifting the stationery diffraction pattern so that the scattered electrons is on the optic axis, the bright-field detector can be used for dark-field imaging. However, an annular dark-field (ADF) detector, which surrounds the bright-field detector, is often used for dark field imaging. Regular ADF detector detects all of the scattered electrons, which contains both Z contrast and diffraction contrast information, sometimes can be difficult to interpret. True Z contrast images can be formed through an ADF detector with a very large central aperture, the so-called high-angle annular dark field (HAADF) detector, which detects electrons scattered through a semiangle of > 50 mrad. Fig. A1.4 shows an example of a HAADF STEM image of a Au nanoparticle/MEH-PPV nanocomposite.

A2. Scanning probe microscopy

Scanning force microscopy (SPM), previously known as the atomic force microscopy (AFM), is a nano- to micro- scale surface imaging technique which involves measuring the topography of a surface with a cantilever. State-of-art SPMs have atomic lateral resolution. In addition to the basic imaging function, multi-functional SPMs can detect various localized properties, such mechanical, dielectric, magnetic, electrical and piezoelectric properties. SPM can be used to investigate many materials systems, such as thin films, nanocomposites, coatings, ceramics, synthetic and biological membranes, metals, polymers, and semiconductors. It is an important tool for morphology characterization throughout our work. In this subsection, we introduce the basics of SPM and several imaging modes.

A2.1. How SPM works

SPM is based on the forces between the tip and the molecules of the sample surface, shown in Fig. A2.2. However, forces are not measured directly. They are calculated from Hook's law, $F = -kz$, k is the spring constant of the cantilever, z is the distance the cantilever is bent, known as the deflection, which is be measured by the SPM system. The forces between the tip and the sample are usually small, in the nanonewton range.

Most SPMs today use a laser beam defection system, where a laser beam is reflected from the backside of the cantilever onto a position-sensitive photodetector. The cantilever and the tip are usually microfabricated from Si or Si_3N_4, tip radius ranging from a few to several tens of nanometers. The schematic of a SPM is shown in Fig. A2.1. The tip rasters across the surface of the sample, with a feedback loop that enables the piezoelectric scanner to maintain the tip at a constant force with the surface (constant

force mode), or at a constant distance away from the surface (constant height mode). In the constant force mode the piezo-electric transducer monitors real time height deviation. In the constant height mode the deflection force on the sample is recorded.

A2.2. Basic imaging modes

The primary operation modes for a SPM include contact mode, non-contact mode, and tapping mode.

In contact mode, the tip is in hard contact with the surface, rastering across the sample. Contact force causes the cantilever to deflect. The deflection of the cantilever is kept constant through the feedback mechanism of the SPM system. As the tip traces the contour of the sample surface, the compensation of the piezoelectric scanner to keep the deflection constant provides the topography information of the sample. In contact mode, the tip-sample distance is in the repulsive regime of the force-distance curve, which is less than a few angstroms, see Fig. A2.2.

Non-contact mode operates in the attractive regime (Fig. A2.2), with tip-sample distance on the order of nanometers to tens of nanometers. The force between the tip and the sample is very small, in pN range, which is beneficial for studying very soft or elastic samples. It is also the base for several functional imaging modes, such as surface potential imaging. The cantilevers used for non-contact mode are usually stiffer than those for contact mode, to prevent being pulled into contact with the sample surface. Non-contact mode is more difficult to measure due to its small signal. Thus, a sensitive, AC detection scheme is used for non-contact operation. Basically, the cantilever is driven at a fixed frequency close to, but greater than, than its free air resonant frequency. The resonance frequency of a cantilever is specified by

$$\omega = \sqrt{\frac{k_{eff}}{m}} \tag{A2.1}$$

where k_{eff} is the effective spring constant of the cantilever, m is the mass of the cantilever. k_{eff} is affected by the force gradient between the cample and the tip,

$$k_{eff} = k - f' \tag{A2.2}$$

where k is the spring constant of the cantilever in the free air, f' is the force gradient. Since the cantilever is forced to oscillate at a fixed frequency, the system measures the change in vibration amplitude to generate topography information.

In tapping mode, the cantilever is driven at a fixed frequency close to, but less than, its free air resonant frequency. The cantilever is oscillated closer to the sample than in noncontact mode, which can be adjusted to be in either the repulsive regime or the attractive regime. Very stiff cantilevers are used in tapping mode, to prevent them from being stuck in the water layer on the sample surface. The advantage of tapping mode is improved lateral resolution on soft samples.

A2.3. Conductive and photoconductive SPM

Conductive SPM is one of the functional modes of SPM. It is a powerful current sensing technique which simultaneously measures the local topography and current of a sample. The current measured by conductive SPM usually ranges from hundreds of femtoamps to nearly a microamp. It can be applied to thin dielectric films, ferro-electric films, nanotubes, conductive polymers, etc. A schematic of the conductive SPM is shown in Fig. A2.3. For materials systems such as thin film organic solar cells, a focused laser beam can be utilized to shine on the sample from underneath passing the transparent substrate, thus local photocurrents as well as topography information can be generated

simultaneously, which give useful information of the internal structure of the thin film solar cells, see Fig. A2.3.

A3. References

1. Williams, D.B. and Carter, C.B. (1996) *Transmission Electron Microscopy,* Plenum Press, New York
2. Chapman, S.K. (1980) *Understanding and Optimizing Electron Microscope Performance 1. Transmission Microscopy*, Science Reviews Ltd, London.
3. Chapman, S.K. (1986) *Maintaining and Monitoring the TEM,* Royal Microscopical Society Handbook, No. 8, Oxford University Press, New York.
4. Edington, J.W. (1976) *Practical Electron Microscopy in Materials Science,* Van Nostrand Reinhold, New York.
5. Eaten, P. and Paul, W. (2010) *Atomic Force Microscopy*, Oxford University Press, New York.
6. Kalinin, S., and Gruverman, A. (2007) *Scanning Probe Microscopy Electrical and Electromechanical Phenomena at the Nanoscale*, Springer, New York.

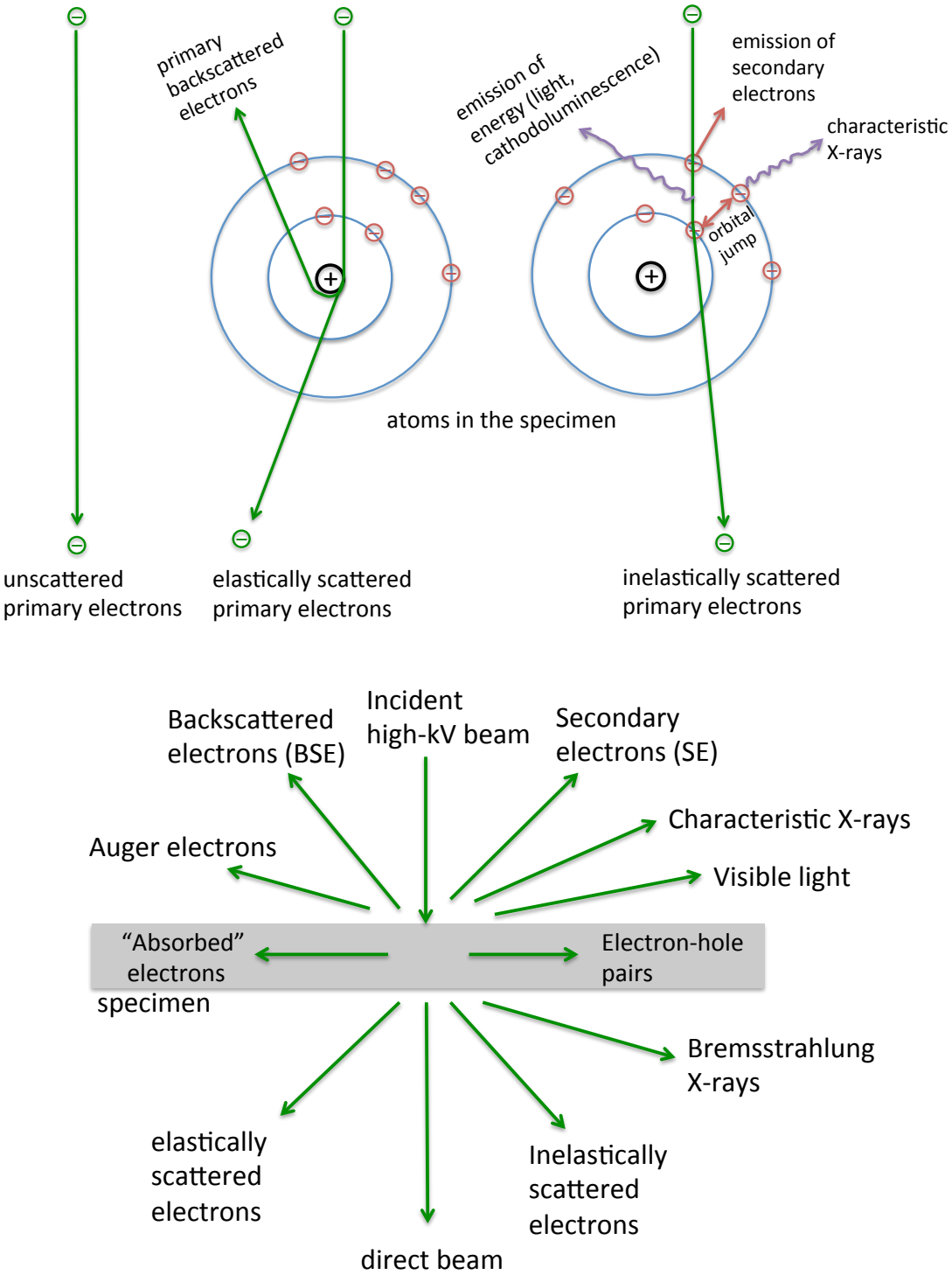

Figure A1.1 Interactions between incident electrons and the specimen are shown here.

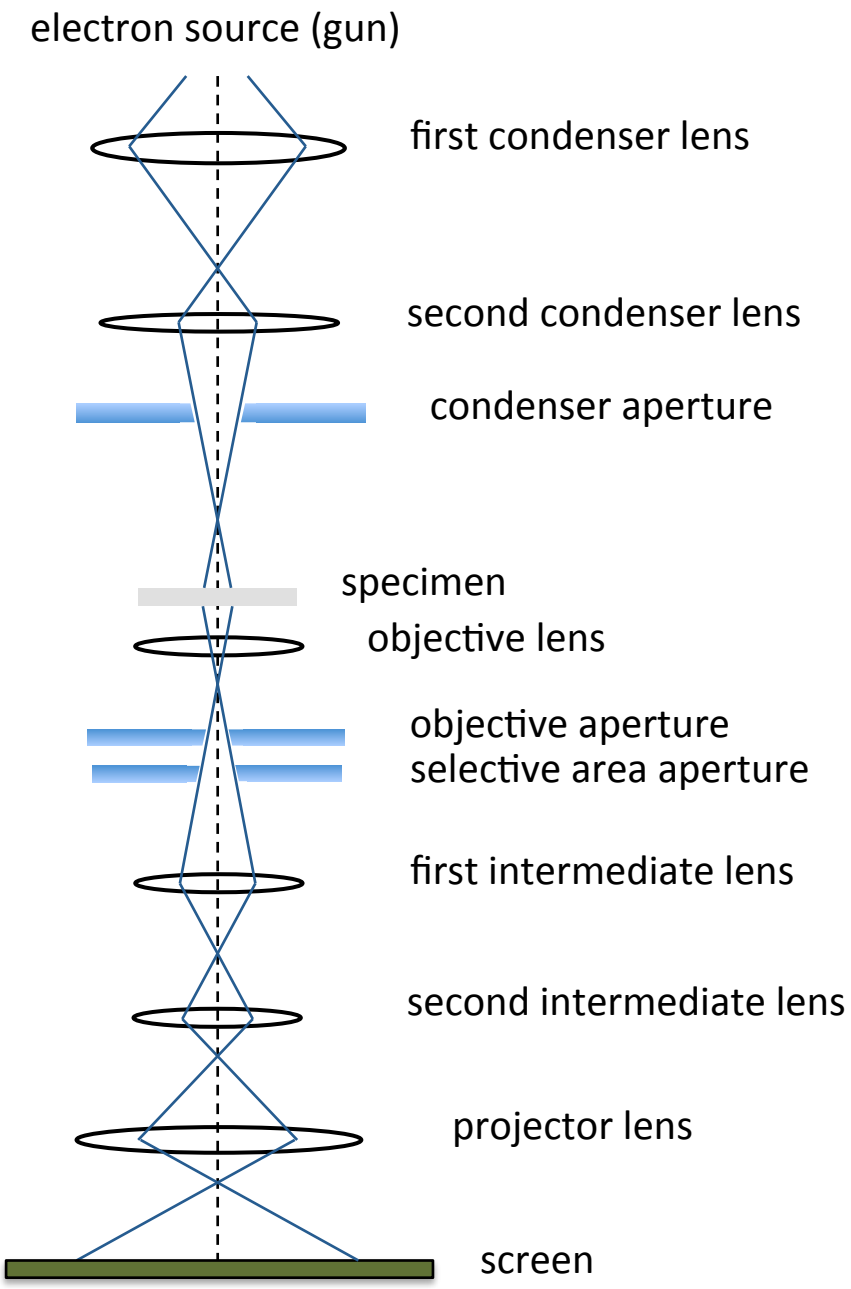

Figure A1.2 The ray diagram of a generic TEM.

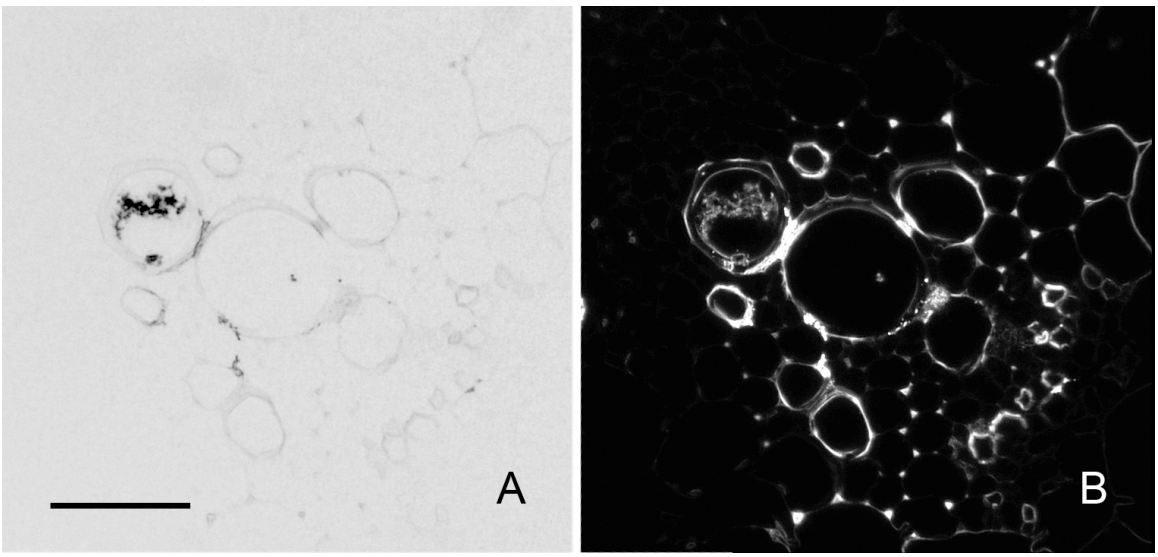

Figure A1.3 A vascular core, showing a cluster of dense material inside of a xylem vessel; A, bright-field image, B, corresponding dark-field image; scale bar = 30 µm. (Corredor et al. BMC plant biology, 2009)

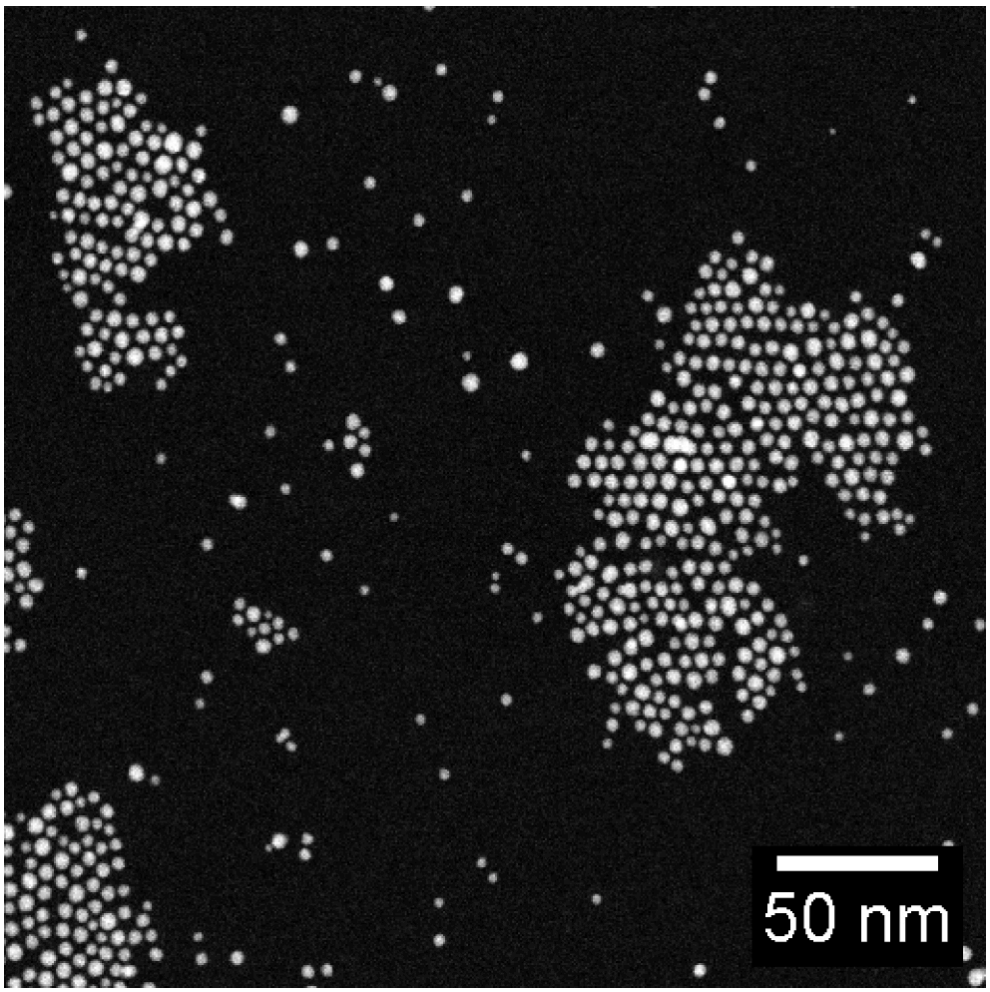

Figure A1.4 An HAADF STEM image of Au/MEH-PPV thin film nanocomposite is shown here.

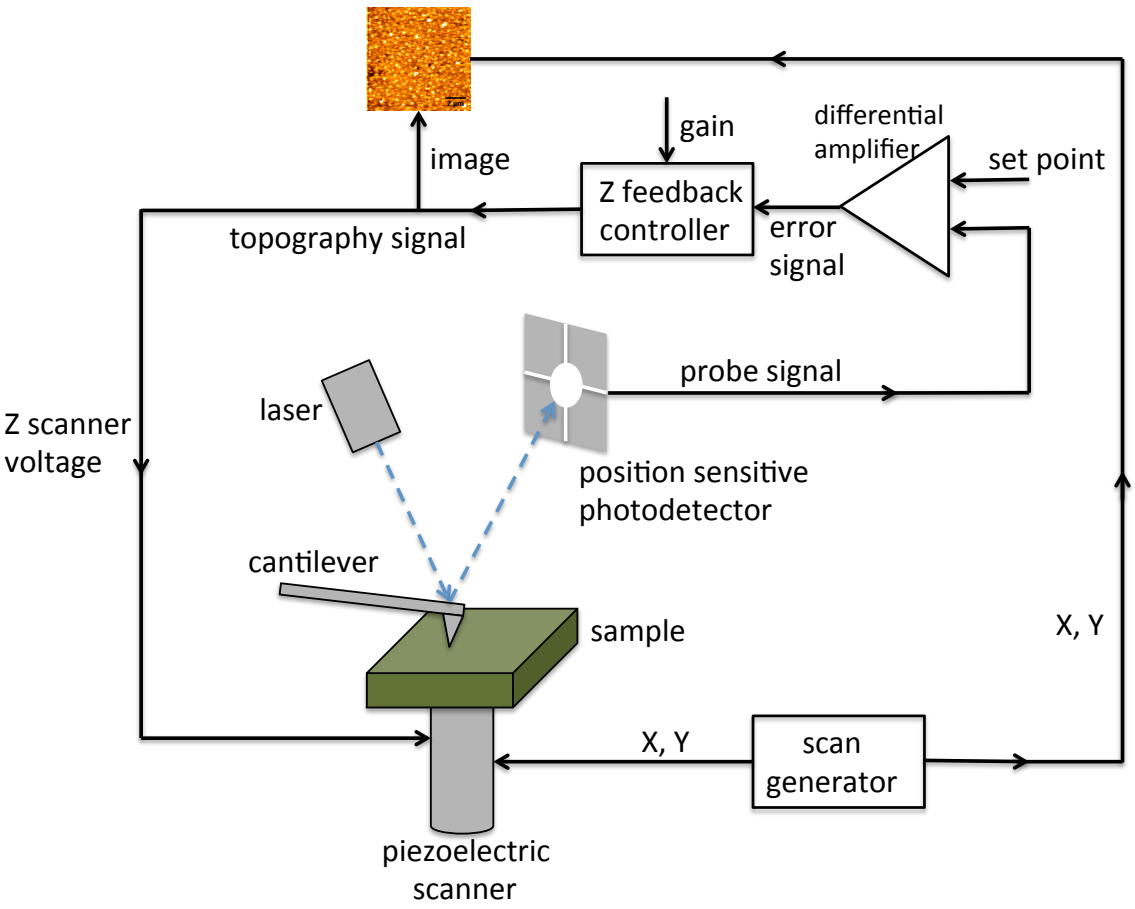

Figure A2.1 Schematic of an SPM is shown here.

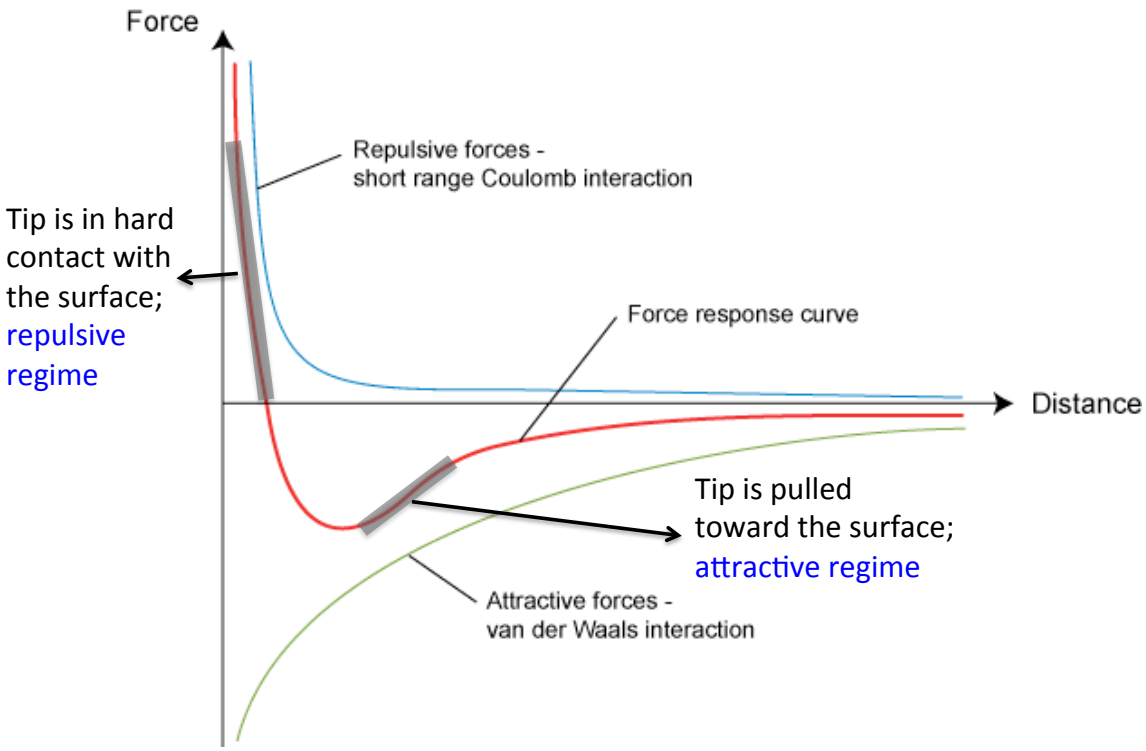

Figure A2.2 The force-distance curve showing the interactions between the tip and the sample surface is shown here.

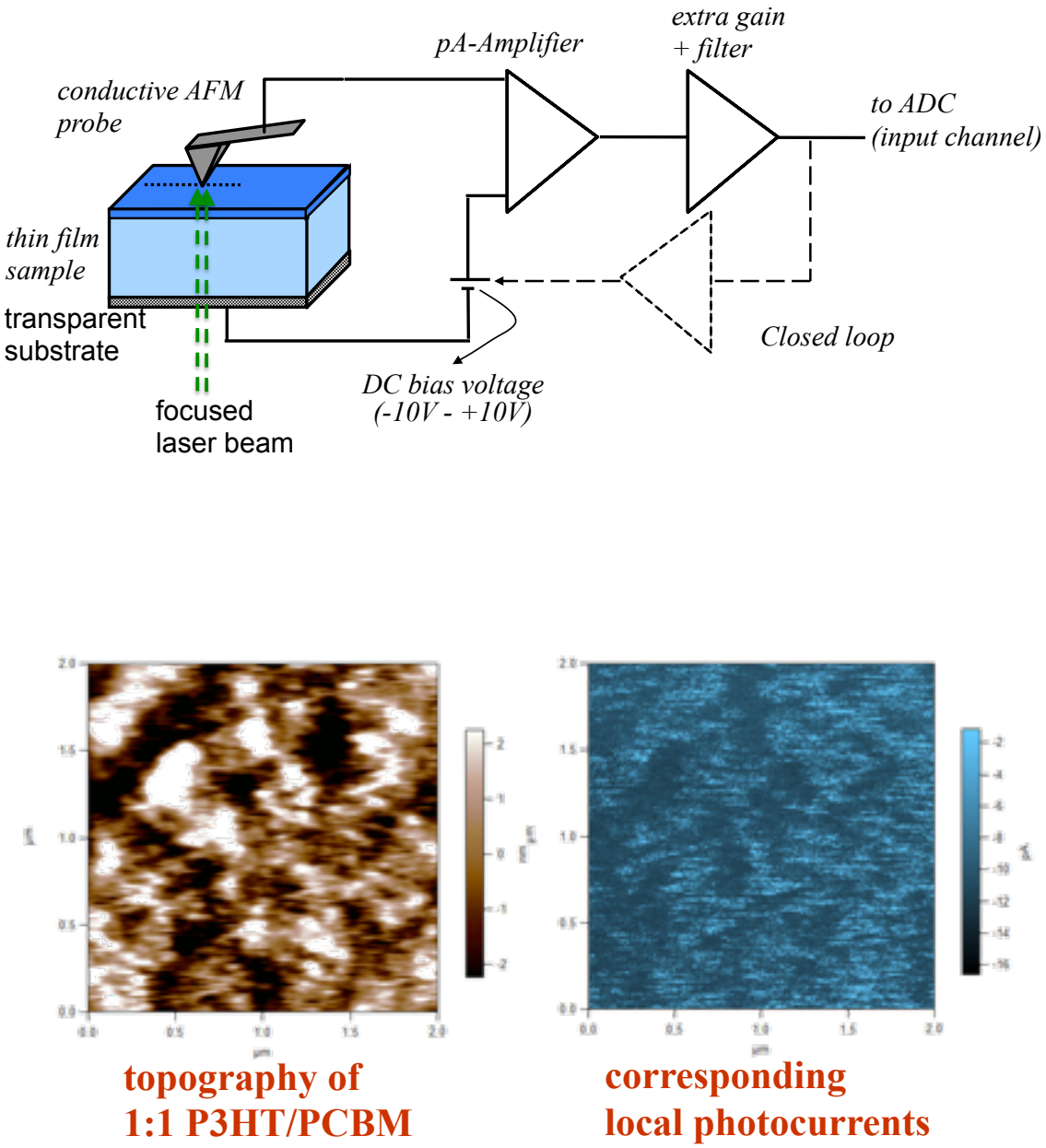

Figure A2.3 Schematic of the photoconductive SPM setup and an example of the photoconductive imaging on organic solar cells are shown here.